JMeXFRI

Indexed in: EMBASE/Excerpta Medica, SciELO, BIBLAT, MIAR, DOAJ, ASCI-Database, Latindex
Preserved in: CLOCKSS

Journal of the Mexican Federation of Radiology and Imaging

J Mex Fed Radiol Imaging

Volume 5. Number 2, April-June 2026
ISSN: 2938-1215
eISSN: 2696-8444

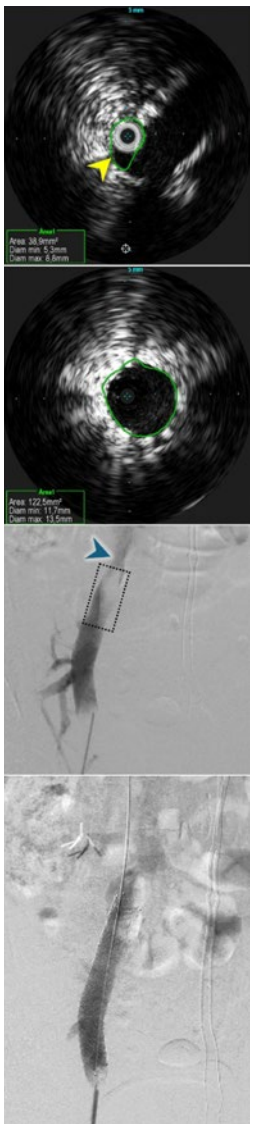

Official Journal of the

FEDERACIÓN MEXICANA DE RADIOLOGÍA E IMAGEN, A.C

PERMANYER
www.permanyer.com

WWW.JMeXFRI.COM

JMeXFRI

Journal of the Mexican Federation of Radiology and Imaging

J Mex Fed Radiol Imaging

Volume 5. Number 2, April-June 2026

ISSN: 2938-1215

eISSN: 2696-8444

The *Journal of the Mexican Federation of Radiology and Imaging* (JMeXFRI) is the official journal of the Federacion Mexicana de Radiologia e Imagen. The aim of the journal is to disseminate scientific knowledge and technological developments for innovation in diagnostic and therapeutic radiology with original articles on basic and clinical aspects of modern radiology in an international context with global impact. JMeXFRI is published in American English with 4 issues per year (print and online) and the first issue was published in the first quarter of 2022. Articles undergo a rigorous, double-blind peer-review process. Publication of articles in JMexFRI is free of charge and all published articles are open access.

The journal publishes the following types of manuscripts: *Full Research Article, Pictorial Essay, Brief Research Article, Technical Note, In-Depth Review, Case Report, Images in Radiology, and Editorial.*

EDITORIAL BOARD

WEBSITE ADMINISTRATION COMMITTEE

GRAPHICAL ABSTRACTS COMMITTEE

SOCIAL MEDIA COMMITTEE

RADIOLOGICAL AND CLINICAL CORRELATION BOARD

Follow us

https://linkedin.com/company/jmexfri

https://instagram.com/jmexfri

https://facebook.com/jmexfri

https://youtube.com/@jmexfri

https://x.com/jmexfri

Original papers should be deposited in their electronic version through the following URL:

https://publisher.jmexfri.permanyer.com

PERMANYER
www.permanyer.com

Permanyer Mexico
Temistocles, 315
Col. Polanco, Del. Miguel Hidalgo
11560 Ciudad de Mexico
mexico@permanyer.com

Permanyer
Mallorca, 310 – Barcelona (Cataluña), España
permanyer@permanyer.com

www.permanyer.com

ISSN: 2696-8444
Ref.: 11908AMEX262

JMeXFRI

Journal of the Mexican Federation of Radiology and Imaging

Check for updates

EDITORIAL

Evolution of cardiothoracic imaging: from images to improved healthcare

Suhny Abbara[1] *and Harold Goerne*[2,3]*

[1]*Department of Radiology, Division of Cardiothoracic Imaging, Mayo Clinic, Jacksonville, FL., USA;* [2]*Department of Radiology, Hospital de Pediatria, Centro Medico Nacional de Occidente, Instituto Mexicano del Seguro Social;* [3]*Centro de Imagen y Diagnostico. Guadalajara, Jalisco, Mexico*

Cardiothoracic imaging is undergoing a profound transformation. Once defined primarily by its ability to depict anatomy and exclude disease, contemporary imaging now increasingly informs prognosis, guides management decisions, and shapes long-term care pathways[1]. This evolution is not due to of a single technological breakthrough, but rather the convergence of advances in imaging hardware, computational modeling, artificial intelligence (AI), and clinical integration. Together, these developments are redefining what it means to "image" the heart and thorax in modern medicine[1-5]. At the center of this shift is a simple but significant change in expectation: cardiothoracic imaging is no longer judged solely by how accurately it detects disease, but by how meaningfully it predicts outcomes and influences patient care. Across cardiac computed tomography (CT) and magnetic resonance imaging (MRI), examinations are increasingly expected to provide functional, physiologic, and prognostic information – often from a single acquisition – while remaining efficient, reproducible, and clinically actionable[1-4]. Cardiothoracic imaging is moving from descriptive assessment toward predictive medicine.

Prognosis as a core imaging endpoint: integrating imaging into risk stratification has long been a goal in cardiovascular care. Traditional clinical risk scores, while valuable, rely primarily on demographic, laboratory, and historical variables that may not fully capture the complexity of myocardial injury, plaque biology, or physiologic reserve. Advanced imaging offers a complementary perspective by directly visualizing tissue characteristics and the functional consequences of disease. Recent studies using multiparametric cardiac MRI illustrate this shift. By combining clinical variables with quantitative MRI-derived features and applying machine-learning techniques, researchers have demonstrated improved long-term prediction of major adverse cardiovascular events after acute myocardial infarction[2]. Importantly, these approaches do not replace clinical judgment; rather, they enhance it by incorporating imaging biomarkers that reflect myocardial injury, remodeling, and functional impairment. Such studies highlight a broader trend: imaging based models can outperform traditional risk scores when they more directly capture disease biology[2]. This paradigm is not limited to MRI or acute coronary syndromes. In patients with stable angina, coronary CT angiography-derived fractional flow reserve (CT-FFR) has shown durable prognostic value over extended follow-up[3].

In the randomized SCOT-HEART trial in Scotland, coronary CT angiography-guided management of patients with stable chest pain demonstrated, at 10-year follow-up, a sustained reduction in coronary heart disease, non-fatal myocardial infarction or death. Identification of atherosclerosis by coronary CT angiography informs preventative strategies and improves long-term cardiovascular outcomes[3]. By transforming an anatomic dataset into a physiologic assessment, CT-FFR enables noninvasive identification of patients at increased risk of adverse outcomes, even years after imaging[4]. These findings reinforce the concept that the value of cardiothoracic imaging increasingly lies in its ability to quantify disease impact, not merely its presence. Collectively, these advances signal a reframing of imaging endpoints. Diagnostic accuracy and morphology remain essential, but prognosis and

***Corresponding author:**
Harold Goerne
E-mail: haroldgoerne@gmail.com

Received for publication: 18-03-2026
Accepted for publication: 10-04-2026
DOI: 10.24875/JMEXFRI.26000010

Available online: 08-07-2026
J Mex Fed Radiol Imaging. 2026;5(2):83-85
www.JMeXFRI.com

risk stratification are becoming equally central measures of success. For radiologists and other cardiac imagers, this evolution requires not only technical expertise but also deeper engagement with clinical outcomes and longitudinal care.

Technology as an enabler of clinical transformation: the expanding therapeutic guidance and prognostic role of cardiothoracic imaging has been made possible by rapid technological innovation, particularly in CT. Photon-counting CT represents a significant hardware advance. Photon-counting detectors provide improved spatial resolution, reduced noise, material decomposition, iodine quantification, virtual monoenergetic images, virtual non-contrast and calcium removed images, and other enhanced spectral capabilities compared with conventional energy-integrating detectors[5]. These features result in clearer visualization of small structures, reduced blooming from calcifications and stents, and more efficient use of radiation and contrast material. Clinically, the importance of these advances extends beyond image quality. Improved spatial resolution and spectral separation enable more accurate plaque characterization, better assessment of coronary lumen and vessel wall, and extraction of quantitative information from a single dataset. In cardiothoracic imaging, where subtle differences in plaque composition, myocardial perfusion, or extracellular volume may carry prognostic significance, such improvements are highly valuable. Other CT innovations further broaden the scope of cardiothoracic imaging. Upright and multi-position CT challenge the traditional assumption that all imaging must occur in the supine position, opening new avenues for assessing cardiopulmonary physiology under more physiologic conditions. Dual-source CT is now available with whole-heart coverage.

AI is a crucial integrative layer across technologies: AI tools extract new information from existing images, transforming how we interpret these images, guide interventionalists, and manage structural heart disease patients. These advances expand the questions CT can address, moving beyond static anatomy to dynamic physiology. Rather than serving as a standalone solution, AI enhances the value of advanced hardware by enabling automated segmentation, quantitative analysis, and pattern recognition at scales beyond human capability. In cardiothoracic imaging, AI-driven tools are already facilitating plaque quantification, ventricular function analysis, and extraction of imaging biomarkers relevant to prognosis and predicting intervention outcomes.

Bridging radiology and cardiovascular care: the expanding prognostic role of cardiothoracic imaging has significant implications for interdisciplinary collaboration. Imaging-derived metrics such as CT-FFR, myocardial strain, and quantitative scar burden increasingly influence clinical decision-making, from revascularization strategies to long-term medical therapy. As a result, cardiothoracic radiologists are becoming integral members of cardiovascular care teams, rather than consultants limited to diagnostic confirmation. This integration is evident in current cardiology perspectives, which trace the evolution of coronary CT angiography from a rule-out test to a comprehensive tool for assessing plaque burden, composition, and hemodynamic significance[6]. Functional CT techniques, combined with AI-enabled analysis, are transforming how coronary artery disease is evaluated and managed. Notably, this evolution has been accompanied by growing acceptance within cardiology, reinforcing the clinical relevance of advanced imaging. For radiologists, this shift presents both opportunity and responsibility. Imaging reports must convey prognostic and functional information in a clear, standardized, and actionable manner. Quantitative metrics must be reproducible and evidence-based, with their limitations transparently acknowledged. As imaging becomes more influential in guiding care, close collaboration with referring practitioners becomes essential.

Challenges and considerations: despite its promise, the transformation of cardiothoracic imaging presents several challenges. Advanced imaging techniques and AI-driven models must be validated across diverse populations and practice settings to ensure generalizability. Workflow integration remains a practical concern, as increasingly complex analyses must be delivered efficiently to avoid delaying care. Additionally, the implementation and interpretability of machine-learning models are ongoing topics of discussion, particularly when imaging-derived predictions influence high-stakes clinical decisions. Education and training also require attention. As cardiothoracic imaging expands into functional and prognostic domains, radiologists must acquire new competencies in quantitative analysis, data interpretation, and interdisciplinary communication. Training programs will need to adapt to ensure that future radiologists are prepared to navigate this evolving landscape.

In conclusion, the future of cardiothoracic imaging is one of integration: combining anatomy and morphology with physiology, computational analysis, and clinical management pathways. Imaging is moving beyond the diagnostic sphere to embrace procedure planning, prognostic evaluation, and clinical management. This transformation

challenges radiologists and other cardiac imagers to evolve their roles –not merely as interpreters of images, but as stewards of imaging-derived insights that guide therapeutic decisions and influence long-term outcomes. Embracing this role will require continued innovation, rigorous validation, and close collaboration with clinical partners. By doing so, cardiothoracic imaging can fulfill its expanding promise: not only to diagnose disease more clearly, but also to improve health through imaging.

Funding

The authors declare that they have not received funding.

Conflicts of interest

The authors declare no conflicts of interest.

Ethical considerations

Protection of human subjects and animals. The authors declare that no experiments on humans or animals were performed for this research.

Confidentiality, informed consent, and ethical approval. This study does not involve personal patient data, medical records, or biological samples, and does not require ethical approval. SAGER guidelines do not apply.

Declaration on the use of artificial intelligence. The authors declare that the content was human generated by the authors but MSCoPilot was used for punctuation and grammar editing.

REFERENCES

1. Abbara S, Shaw LJ. Past, present, and future of CTA. Circulation. 2024;150(2):87-90. doi:10.1161/CIRCULATIONAHA.124.068325.
2. Xie W, Shi R, Xiang J, Chen B, An DA, Zhou Y, et al. Machine learning using clinical and cardiac MRI features to predict long-term outcomes in acute STEMI. Radiology. 2026;318(2):e251490. doi:10.1148/radiol.251490.
3. Williams MC, Wereski R, Tuck C, Adamson PD, Shah ASV, van Beek EJR, et al. Coronary CT angiography-guided management of patients with stable chest pain: 10-year outcomes from the SCOT-HEART randomised controlled trial in Scotland. Lancet. 2025;405(10475):329-337. doi:10.1016/S0140-6736(24)02679-5.
4. Madsen KT, Nørgaard BL, Øvrehus KA, Scheuer ST, Jensen JM, Leipsic J, et al. Seven-year prognostic value of coronary CT angiography-derived fractional flow reserve in stable angina. Radiology. 2025;317(1): e251788. doi:10.1148/radiol.251788.
5. Douek PC, Boccalini S, Oei EHG, Cormode DP, Pourmorteza A, Boussel L, et al. Clinical applications of photon-counting CT: a review of pioneer studies and a glimpse into the future. Radiology. 2023;309(1):e222432. doi:10.1148/radiol.222432.
6. Schiebler ML, Jinzaki M, Yanagawa M, Pourmorteza A, Yamada Y, Kato Y, et al. Future applications of cardiothoracic CT. Radiology. 2025;315(3): e240085. doi:10.1148/radiol.240085.

JMeXFRI

Journal of the Mexican Federation of Radiology and Imaging

Check for updates

IN-DEPTH REVIEW

The call for mastering chest radiography – an urgent priority for training radiologists and trainees

Santiago Martinez-Jimenez

Department of Radiology, University of Missouri-Kansas City and Department of Radiology, Thoracic Imaging Division, Saint Luke's Hospital, Kansas City, Missouri, USA

ABSTRACT

Chest radiography remains the most frequently performed imaging examination and the primary diagnostic tool for thoracic evaluation worldwide. Despite its central clinical role, interpretive expertise has declined with the widespread adoption of computed tomography (CT), which offers greater contrast resolution but introduces higher radiation exposure, increased cost, and limited accessibility in many settings. This article argues that renewed emphasis on chest radiograph interpretation is an urgent educational and professional priority. Chest radiography is technically and diagnostically unique, employing high kilovoltage techniques to optimize grayscale latitude and enable detection of subtle pulmonary and mediastinal abnormalities. Accurate interpretation requires understanding both imaging physics and structured analytic approaches. Foundational concepts popularized by Benjamin Felson and others – including gestalt-based pattern recognition and classic signs such as the silhouette, hilum overlay, or cervicothoracic signs remain essential but risk being underemphasized in contemporary training. Strengthening education in these principles can improve diagnostic consistency, reduce unnecessary downstream imaging, and enhance patient outcomes. While systemic workflow challenges influence radiology practice, responsibility for interpretive excellence rests with educators and clinicians. Reinvesting in mastery of chest radiography is therefore both a practical necessity and an ethical obligation, ensuring that this fundamental modality continues to support accurate, efficient, and accessible patient care in modern medicine.

Keywords: *Chest radiography. Aunt Minnie. Felson. Chest imaging. Gestalt.*

INTRODUCTION

While chest radiography remains the most common imaging examination in all radiology departments, its proficiency and interpretive interest seem to have gradually diminished. This decline has become particularly evident since the widespread adoption of computed tomography (CT) after the 1980s. The reasons for this decline are multifaceted, with several apparent factors. CT provides significantly superior contrast resolution compared to radiography, resulting in more conspicuous abnormalities. Consequently, radiologists who interpret both chest radiographs and CT scans often observe findings on CT that may be subtle or even occult on radiography. This raises the question of whether chest CT scans should always be preferred over chest radiography. However, this hypothetical question lacks practicality for several reasons. First, the availability of CT scanners and the time required for both performing and interpreting CT scans may never be sufficient to replace the use of chest radiography. Second, the high radiation

Corresponding author:
Santiago Martinez-Jimenez
E-mail: smartinez-jimenez@saintlukeskc.org

Received for publication: 10-03-2026
Accepted for publication: 22-03-2026
DOI: 10.24875/JMEXFRI.26000009

Available online: 08-07-2026
J Mex Fed Radiol Imaging. 2026;5(2):86-97
www.JMeXFRI.com

dose associated with chest CT makes widespread use impractical, given that chest radiography currently serves as the primary imaging modality for this purpose. Furthermore, the current level of radiation exposure from CT scanning poses a public health concern. For example, a study published in 2025 by Smith-Bindman revealed that 5% of all new cancer cases are attributed to current CT use and radiation dose[1]. Additionally, CT may not always be feasible or practical in certain settings, such as intensive care units or hospitals with limited technological resources. Therefore, for the foreseeable future, chest radiography remains the initial imaging tool for patient assessment. It is imperative that we review, replan, and refine our skills in interpreting chest radiographs to ensure their continued relevance and accuracy.

The substantial volume of chest radiographs can sometimes be overwhelming prompting radiology departments to adopt various strategies to manage their immense workload. Some departments choose not to interpret chest radiographs, allowing clinicians to review them independently. Others assign all chest radiographs to general radiologists, reserving subspecialty readers for more complex studies such as CT and magnetic resonance imaging (MRI) at a higher level of interpretation. Multiple strategies are feasible, each with its own rationale. However, a common theme emerges there is a low level of interest and sophistication in interpreting chest radiographs. This presents a challenge, as chest radiography is the most frequently performed study in any radiology department and may contain critical information for clinical decision-making. It is contradictory that the most common imaging examination, with significant potential impact on clinical decisions, is perceived as a radiologic nuisance. While it may seem reasonable to consider strategic and policy-level responses to address the substantial workload in radiology departments – particularly the high volume of chest radiographs – such responsibilities largely fall outside the scope of academic practitioners and reside primarily with institutional leadership and radiology administrators. Practicing radiologists, although directly affected by these systemic pressures, have limited influence over resource allocation, workflow design, or policy implementation. Nevertheless, this reality does not diminish our professional obligation. Our foremost responsibility remains patient care through the accurate and timely interpretation of chest radiographs. Given these challenges, it is plausible that current levels of proficiency may not consistently meet optimal standards.

EDUCATIONAL FRAMEWORK FOR CHEST RADIOGRAPHY INTERPRETATION

Rather than viewing this limitation solely as a systemic constraint, it should be recognized as a meaningful opportunity for educational renewal. The current circumstances encourage educators and senior clinicians to re-emphasize foundational interpretive principles, reinforce structured approaches to image analysis, and build confidence among trainees. By deliberately strengthening the educational framework for chest radiograph interpretation, radiology training programs can promote greater diagnostic consistency and reduce interpretive variability.

Improving trainees' comfort and competence in reading chest radiographs has implications that extend beyond academic performance. Enhanced interpretive accuracy can reduce downstream diagnostic uncertainty, minimize unnecessary imaging or interventions, and support more efficient clinical decision-making. Ultimately, such improvements may mitigate not only financial costs to healthcare systems but, more importantly, the human cost borne by patients through delayed diagnoses, avoidable complications, or suboptimal care. In this context, reinforcing fundamental radiographic interpretation is not merely an educational objective but a practical and ethical imperative.

WHY IS CHEST RADIOGRAPHY SUCH A UNIQUE IMAGING STUDY?

Within the spectrum of diagnostic imaging, chest radiography occupies a distinctive and uniquely demanding role. It differs from other radiographic examinations not only in technical execution but also in diagnostic purpose, image characteristics, and interpretive complexity. Unlike many region-specific radiographs that focus primarily on the structural detail of dense tissues, chest radiography is designed to evaluate a wide range of structures with markedly different radiographic properties, including air-filled lungs, the soft tissue mediastinum, vascular structures, and osseous components. This diversity of tissue composition requires imaging parameters that differ fundamentally from those used in abdominal or musculoskeletal radiography.

One of the most defining technical features of chest radiography is the routine use of a substantially higher kilovoltage potential (kVp). This discussion refers to the frontal chest radiograph performed on a fixed unit, not a portable chest radiograph, which does not use the

high kVp technique. While musculoskeletal radiographs are commonly acquired at approximately 60-70 kVp and abdominal studies at intermediate levels, chest radiography is typically performed at approximately 120-140 kVp. This distinction is deliberate and reflects the specific optimization required for thoracic imaging.

From a geometric perspective, chest radiography often uses a relatively long source-to-image distance to reduce magnification and distortion of thoracic structures, particularly the cardiac silhouette and mediastinum. Increasing this distance reduces beam divergence at the detector, thereby improving dimensional accuracy. However, a greater distance also leads to attenuation of photon intensity before reaching the detector. To compensate for this loss and maintain adequate penetration through the thorax, higher beam energy is required.

DIAGNOSTIC RATIONALE OF CHEST RADIOGRAPHY RELATED TO IMAGE INTERPRETABILITY

Beyond geometric factors, the diagnostic rationale for using higher kVp is closely related to image interpretability. High-kVp imaging produces a broader spectrum of gray tones, commonly referred to as increased radiographic latitude. This wide latitude is especially important for evaluating the lung parenchyma, where clinically significant findings often appear as subtle variations in attenuation rather than distinct high-contrast abnormalities. The lungs contain a complex mix of air, interstitial tissue, vascular structures, and potential pathological processes, all of which produce only modest differences in x-ray attenuation. A wide grayscale range allows these subtle density variations to be appreciated simultaneously without sacrificing visibility of mediastinal or vascular structures. In contrast, lower kVp techniques produce images with higher contrast resolution but a narrower grayscale range. This higher contrast enhances visualization of cortical bone and fine osseous detail.

Another important effect of higher kVp is the relative reduction in the visual prominence of osseous structures. As photon energy increases, the differential attenuation between bone and soft tissue decreases, effectively softening the appearance of ribs, clavicles, and the thoracic spine. This reduction in bone contrast is diagnostically advantageous because the primary focus of chest radiography is typically the lung parenchyma and mediastinal structures rather than skeletal anatomy. By reducing the conspicuity of overlying bones, high-kVp imaging allows better visualization of pulmonary markings and parenchymal abnormalities that might otherwise be obscured.

This principle is especially evident when comparing standard chest radiography with rib series imaging. Rib radiographs, commonly acquired at lower kVp values, are designed to maximize osseous contrast and delineate cortical margins. In these images, the lung parenchyma appears more attenuated, diminishing the visibility of intrinsic pulmonary abnormalities. In contrast, a standard chest radiograph acquired with higher kVp shows the lung parenchyma with a wider range of grays, facilitating the detection of focal or diffuse opacities. For example, identifying a pneumothorax relies on recognizing subtle differences in lung edge definition and pleural air, a task that is considerably more challenging on lower-kVp musculoskeletal-focused imaging.

In addition to improving visualization of pulmonary structures, high-kVp chest radiography provides more uniform penetration across the thorax. The thoracic cavity contains regions with markedly different thicknesses and densities, ranging from the air-filled lung apices to the denser mediastinum and diaphragm. A higher-energy beam reduces the risk of underpenetration in thicker regions while preserving sufficient detail in thinner areas, resulting in a more diagnostically balanced image.

THORACIC ANATOMY, IMAGING GEOMETRY, AND DIAGNOSTIC OBJECTIVES OF CHEST RADIOGRAPHY

The technical and physical principles explain why chest radiography cannot be considered simply another form of general radiography. Its acquisition parameters are specifically tailored to balance penetration, contrast, and diagnostic latitude to support the detection of subtle and clinically significant pathology. Understanding these distinctions is essential not only for technologists performing the examination but also for radiologists interpreting the images. Mastery of chest radiograph interpretation therefore requires knowledge of both the physical principles governing image formation and the clinical implications of technique selection.

In summary, the routine use of higher kilovoltage in chest radiography is not merely a technical preference but a fundamental requirement dictated by thoracic anatomy, imaging geometry, and diagnostic objectives. By expanding grayscale latitude, reducing osseous dominance, and enabling uniform penetration of heterogeneous thoracic structures, high-kVp imaging provides the optimal foundation for accurate evaluation of pulmonary and mediastinal pathology.

FUNDAMENTAL CONCEPTS OF DIAGNOSTIC SIGNS IN CHEST RADIOGRAPHY

The characteristics that distinguish chest radiography from other radiographic modalities reinforce its unique role in diagnostic imaging. This distinctiveness has led several scholars to propose strategies that address the specific features of chest radiography. A notable historical example is the collection of principles elucidated and disseminated by Dr. Benjamin Felson[2]. In his seminal work, "Chest Roentgenology," a classic in the field of radiology, Felson compiled a series of findings that may not be immediately apparent but rather require a holistic understanding, akin to a gestalt[2,3]. Throughout his distinguished academic career, he meticulously identified these specific findings as diagnostic signs (e.g., silhouette, hilum overlay, hilum convergence, cervicothoracic, thoracoabdominal, etc.). Notably, he also popularized the concept of Aunt Minnie's (originally described by Ed Duncan Neuhauser)[4]. This refers to an evident and characteristic finding, similar to identifying "Aunt Minnie" in a crowd through gestalt perception[3-7]. However, if an individual has not previously met Aunt Minnie, it is impossible to recognize her. Similarly, in the field of radiology, an Aunt Minnie requires the radiologist to be familiar with Aunt Minnie's facial features to identify her among many findings.

This concept introduces a novel approach to learning that challenges the traditional method of recognizing individual findings and patterns. Instead of describing each feature separately (such as the mouth, nose, eyes, eyebrows, or hair), this approach emphasizes recognizing the overall set of findings. It is similar to recognizing a face without distinguishing its individual characteristics, as proposed by the psychological theory of gestalt[3,6]. Felson introduced and emphasized the importance of a gestalt approach in chest radiography interpretation, noting that it is not intuitive and requires deliberate learning to understand or appreciate effectively. If radiology educators do not address and teach these concepts comprehensively, they may eventually become obsolete. This phenomenon may help explain the increasing challenges radiologists face in interpreting chest radiographs.

Fortunately, the fundamental concepts that Felson introduced, along with additional ones described after his seminal works, can still be learned. In an era where intuitive development and logical deduction are the prevailing norms, the gestalt approach is not mainstream. Although technological advancements continue at a rapid pace, radiologists are constantly challenged to expand their knowledge bases. Nevertheless, there is a pressing need to revisit the fundamental principles that have been somewhat overlooked or disregarded over the past three to four decades. The following examples, taken from Felson's original textbook "Chest Roentgenology," are presented in this review to highlight the importance of this distinct type of learning in facilitating the proper interpretation of chest radiographs.

SILHOUETTE SIGN

The iconic sign popularized by Felson is arguably the "silhouette" sign. In his original book, it is described as follows[2]: *"an intrathoracic lesion touching a border of the heart, aorta, or diaphragm will obliterate that border on the roentgenogram. An intrathoracic lesion not anatomically contiguous with a border of one of these structures will not obliterate that border".* Notably, the sign refers to the absent or obliterated silhouette; it signifies the absence of a silhouette, which can sometimes confuse trainees.

This sign is widely recognized by radiologists and most clinicians. It is such a fundamental concept that no further explanation is typically necessary. Essentially, any portion of the lung replaced by air and adjacent to the silhouetted organ will cause obliteration of the adjacent margin of that organ, such as portions of the cardiac contour or other soft tissue structures like the diaphragm or the neck, as the organ's density increases from air to soft tissue, provided both have similar densities[8-13]. For example, a consolidated right middle lobe can obscure the right cardiac contour. Similarly, consolidation of the lingula can obscure the left cardiac contour (Figure 1), and consolidation of the apicoposterior aspect of the left upper lobe can obscure the aortic arch contour.

However, the same principle underlying the concept of the "silhouette" sign applies to various other imaging instances. In the presence of pleural effusion, the "meniscus sign" can be observed. This sign occurs because pleural fluid, which is closer in density to soft tissue than to air, causes "silhouetting" of the adjacent diaphragm. Similarly, when there is consolidation of the basilar portion of the lung, the consolidation leads to obscuration of the adjacent diaphragm. Certain signs, such as the "cervicothoracic" and "thoracoabdominal" signs, are simply corollaries of this concept. For example, if a mass is located in both the chest and the neck (i.e., cervicothoracic sign), the mass has a distinct inferior border but loses its superior border as it extends

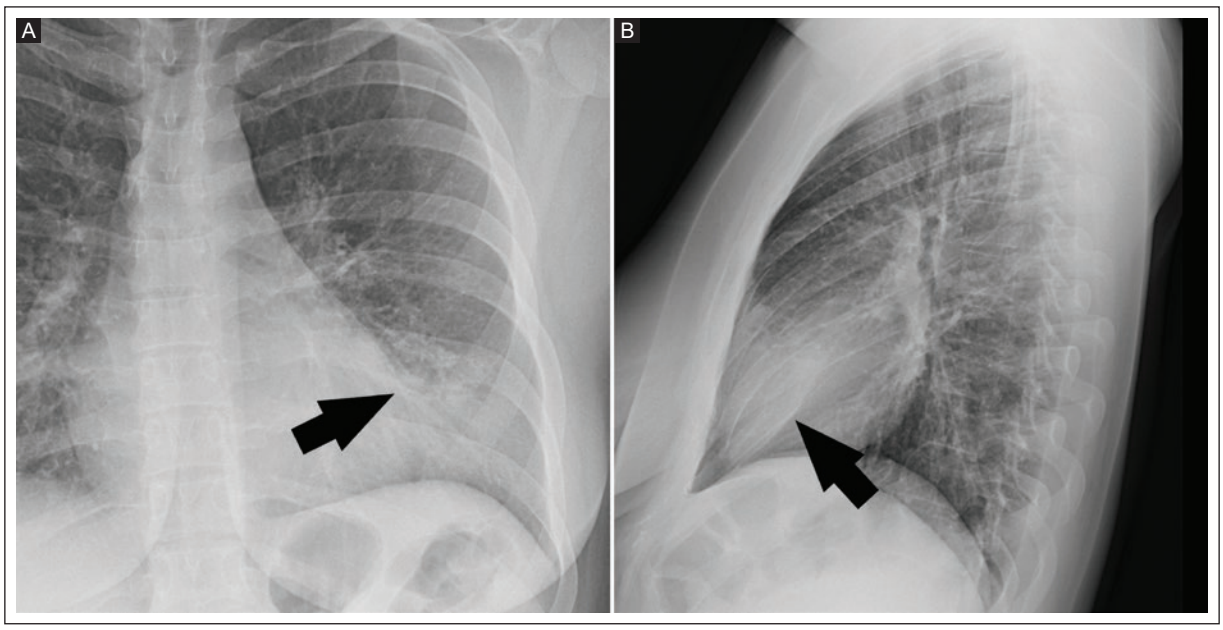

Figure 1. Patient with lingular pneumonia and the silhouette sign. **A:** frontal chest radiograph shows opacity along the left lower hemithorax with obscuration (arrow) along the left heart border. **B:** lateral chest radiograph shows paracardiac opacities corresponding to the anatomic location of the lingula.

into the neck, where it is no longer defined by lung air. Consequently, the mass is "silhouetted" by the soft tissues of the neck. This classic description by Felson is discussed in greater detail later. Nevertheless, other signs not typically considered corollaries of the "silhouette" sign may also be explained by the same principles, as discussed below.

HILUM OVERLAY AND HILUM CONVERGENCE SIGNS

The hilum overlay sign and hilum convergence sign are critical for understanding hilar contour abnormalities[2,14,15]. Typically, a convexity should not be observed in the hilar regions. However, a convexity in this region is considered abnormal and warrants further investigation. Felson defined the hilum overlay sign as a hilar convexity that still allows visualization of the pulmonary vessels, which now lie over the abnormal contour. His description is as follows[2]: *"visibility, on the PA film, of either the right or left pulmonary artery more than a centimeter within the lateral edge of what appears to be the cardiac silhouette".*

This phenomenon typically occurs with prevascular masses, such as thymoma, germ cell tumor, lymphoma, and others (Figure 2). However, it can also be seen in masses located posterior to the hilum, such as a thoracic aortic aneurysm. In this context, Felson describes that the hilar vessels can be observed within 1 cm of the edge of the contour abnormality but not beyond that[2]. The absence of "silhouetting" of the pulmonary hilar vessels is another consequence of this overlay sign.

Conversely, if the pulmonary vessels reach the edge of the abnormal convexity but do not significantly extend beyond it, this phenomenon is more accurately described as the hilum convergence sign. The original description states[2]: *"If the pulmonary artery branches converge toward the mass rather than toward the heart, you are dealing with an enlarged pulmonary artery".* This finding suggests that the contour abnormality is due to an enlarged pulmonary trunk, which may be associated with pulmonary hypertension (Figure 3) or pulmonic valve stenosis (Figure 4).

THIRD MOGUL AND OTHERS

Another concept, less frequently mentioned but also popularized by Felson[2] in his textbook and originally described by Daves[16,17] is the "third mogul". In skiing, a mogul refers to a bump on a snow slope created by skiers through turns and snow packing or intentionally constructed for competition. As described by Daves, several "moguls" can be found along the cardiac silhouette. Within the cardiac silhouette, the term "mogul" includes both normal and abnormal convexities.

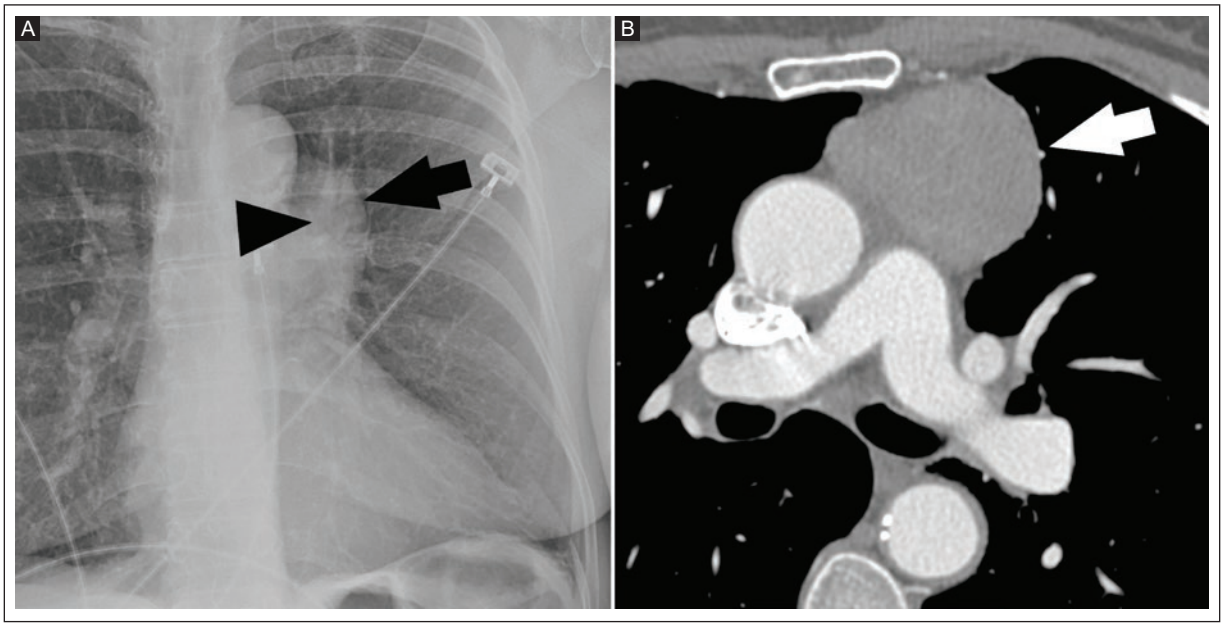

Figure 2. Patient with thymoma demonstrating the hilum overlay sign. **A:** frontal chest radiograph shows abnormal left hilar convexity (arrow) with well-defined hilar vessels (arrowhead) visible through the hilar abnormality, known as the hilum, overlay sign. **B:** contrast-enhanced chest CT shows a prevascular soft-tissue mass (arrow) corresponding to the abnormality seen on chest radiography.
CT: computed tomography.

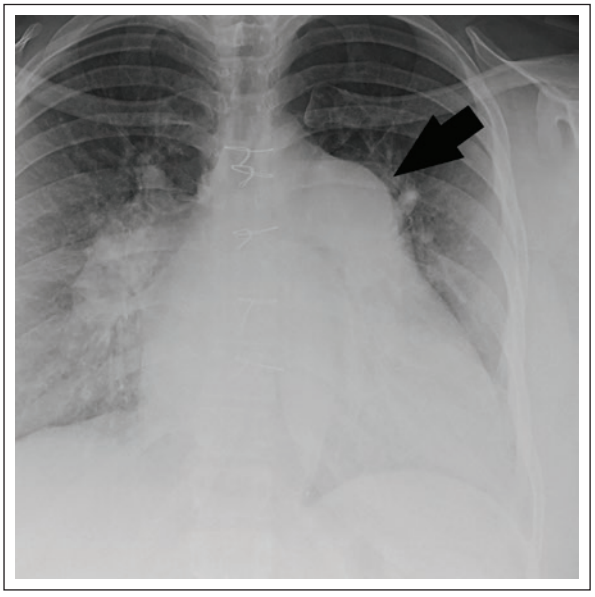

Figure 3. Patient with pulmonary hypertension showing the hilum convergence sign. Chest radiograph shows abnormal left hilar convexity (arrow). Note that the hilar vessels reach the edge but are not seen through the hilar convexity.

The right atrium, the first normal mogul, is the only normal convexity on the right side. The left side has two normal moguls: the aortic arch (first mogul) and the left ventricle (fourth mogul). Under abnormal circumstances, second and third moguls may also be present, representing a large pulmonary trunk and a large atrial appendage (Figure 5), respectively. When encountering a hilar abnormal contour, it is important to distinguish it from true hilar abnormality, such as the hilum convergence and hilum overlay signs, as well as the third mogul. An imaginary line along the left main stem bronchus shadow serves as a useful landmark for distinguishing true hilar abnormality above that line from an enlarged atrial appendage (i.e., third mogul) below the line. While most cases involving the third mogul are associated with enlarged atrial appendages, other potential causes include a mediastinal mass, infundibular hump in tetralogy of Fallot, pericardial cyst, and pulmonary arteriovenous malformation[18].

CERVICOTHORACIC AND THORACOABDOMINAL SIGN

As previously stated, when a mediastinal mass or contour abnormality – especially one above the subjective vicinity of the aortic arch (i.e., in the superior mediastinum) – has a distinct inferior border that becomes obscured as it extends superiorly, this is known as the cervicothoracic sign. Felson described it as follows[2]: *"based on the tenet that if a thoracic lesion is in anatomic contact with the soft tissues of the neck, its contiguous border will be lost. The cephalic border*

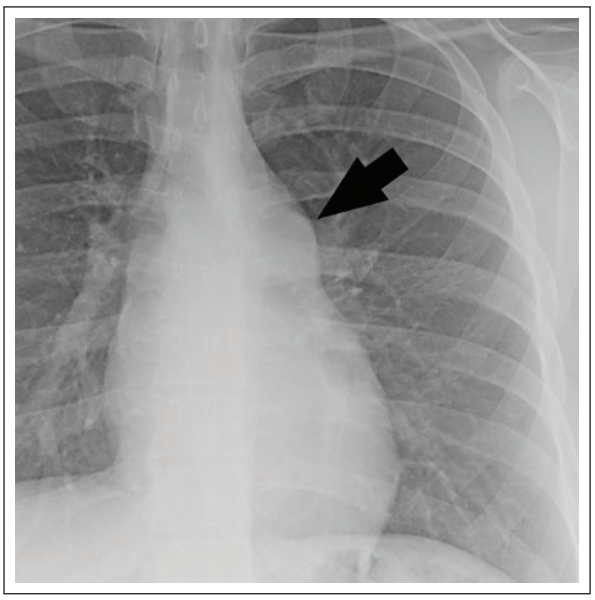

Figure 4. Patient with pulmonic valve stenosis showing the hilum convergence sign. Frontal chest radiograph shows abnormal left hilar convexity (arrow). Note that the hilar vessels reach the edge but are not seen through the hilar convexity. Also note that the pulmonary arteries are normal, which would not be expected in pulmonary hypertension.

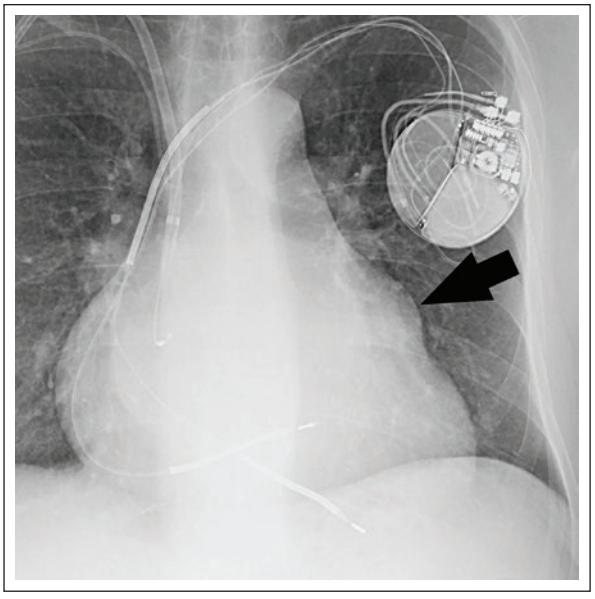

Figure 5. Patient with dilated left atrium showing the third mogul. Frontal chest radiograph shows abnormal left hilar convexity (arrow). Note that this convexity is slightly more inferior, notably below the left mainstem bronchus compared to figures 3 and 4.

of the anterior mediastinum ends at the level of the clavicles, whereas that of the posterior mediastinum extends much higher. Hence, a lesion clearly above the clavicles on the frontal view must lie posteriorly and entirely within the thorax". Felson introduced the clavicle as a key anatomical landmark, using it to demarcate the transition between the inferior, well-defined, and superior ill-defined borders. Classic masses exhibiting the cervicothoracic sign include thyroid masses with intrathoracic extension (Figures 6 and 7), a tortuous but otherwise normal brachiocephalic trunk, and rarer entities such as cervicothoracic lymphangioma[10,19,20].

Many radiology textbooks have introduced a misconception about this sign, deviating from Felson's original description. They have presented it as a sign almost pathognomonic of paravertebral neurogenic tumors. However, thoracic neurogenic tumors rarely extend into the neck or vice versa, leading to confusion. Contrary to some textbooks claims, a neurogenic tumor typically does not exhibit a cervicothoracic sign.

The thoracoabdominal sign is a corollary of the cervicothoracic sign and is useful when masses are located within the chest but also extend into the abdomen and, consequently, the thoracoabdominal region. In contrast to the clavicle, Felson refers to the hemidiaphragm as the defining anatomical landmark. He described it as follows[2]: *"A silhouette sign on its lowermost margin indicates that the mass ends at the diaphragm or extends below it. Convergence of the lower lateral margin toward the spine indicates that the bottom lesion is nearby and, therefore, that the lesion is probably entirely intrathoracic".* This situation is frequently encountered, as in hiatus hernia. Conversely, thoracic masses in this region that typically do not extend into the abdomen, such as extramedullary hemopoiesis, should not manifest the thoracoabdominal sign.

LUFTSICHEL SIGN

One particularly challenging sign with an Aunt Minnie character is the Luftsichel sign[20-25]. The term originates from Germany, combining "Luft" (air) and "Sichel" (sickle)[23]. Although historical references indicate that this sign was described by the Germans in the 1940s, which explains its German name[25], Felson described in his book[2]: *"LUL collapse has caused so much forward displacement of the upper section of the major fissure that the superior segment of the air-filled LLL now lies in opposition to the aortic knob,"* which is exactly what is known as the Luftsichel sign. It refers to an opacity of the superior hemithorax with a sickle – or crescent-shaped hyperlucency typically overlying the aortic arch. The sign is counterintuitive because

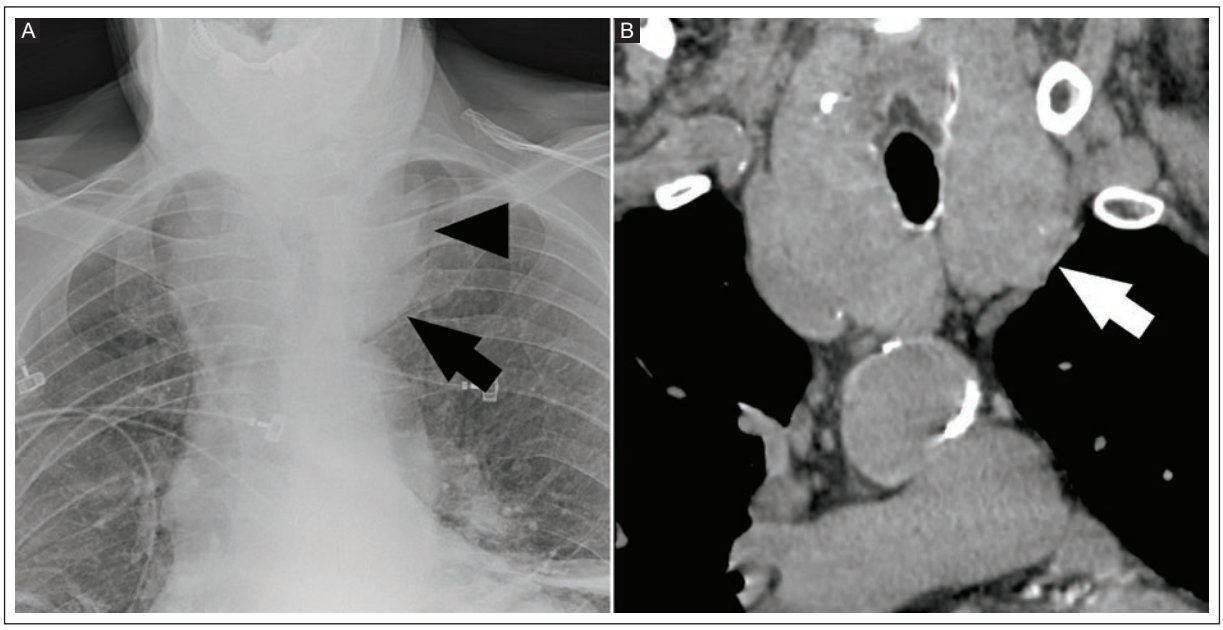

Figure 6. Patient with thyroid goiter and cervicothoracic sign. **A:** frontal chest radiograph shows abnormal convexity along the left superior mediastinum with a well-defined inferior border (arrow) which progressively fades (arrowhead) as it reaches the level of the ipsilateral clavicle, the so-called cervicothoracic sign, which indicates this mass in partially within the chest and partially within the neck. **B:** nonenhanced chest CT shows enlarged thyroid with intrathoracic extension. Note that the inferior border of the mass (arrow) is outlined by lung, which correlates with the radiographic manifestation of a well-defined inferior border.

CT: computed tomography.

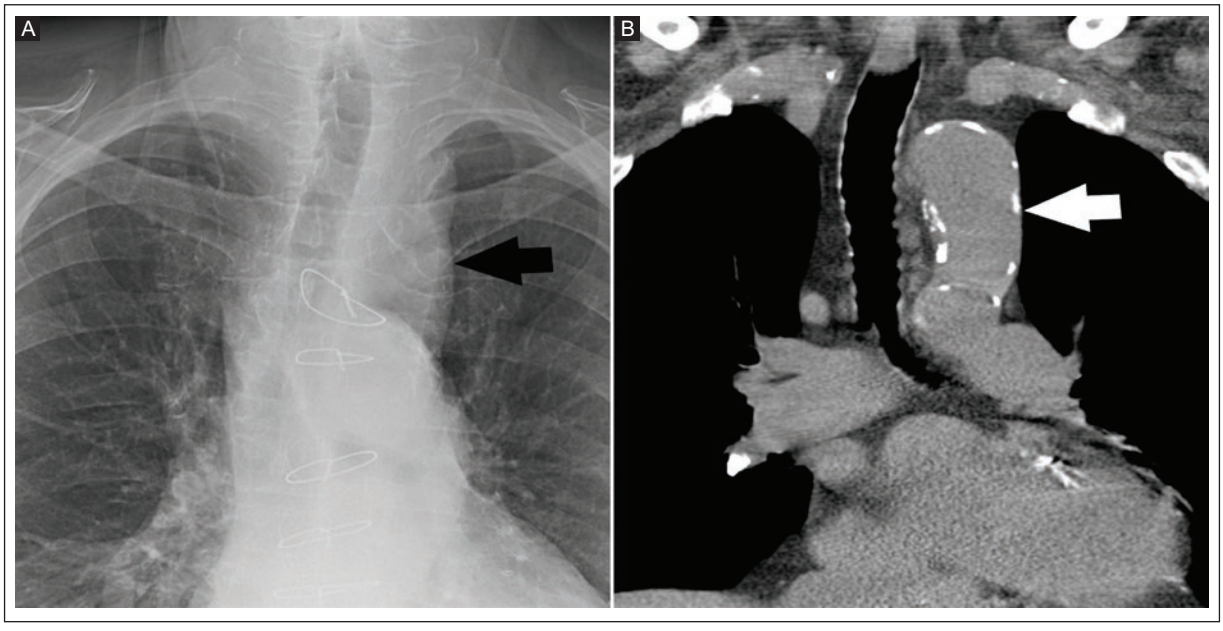

Figure 7. Patient with cervical aortic arch without the cervicothoracic sign. **A:** frontal chest radiograph shows abnormal convexity along the left superior mediastinum with well-defined inferior and superior borders (arrow), indicating that this mass is entirely within the chest and does not extend into the neck. **B:** nonenhanced chest CT shows cervical aortic arch (arrow). This example is provided to contrast and clarify the cervicothoracic sign.

CT: computed tomography.

the superior segment of the left lower lobe anatomically migrates superiorly into the upper hemithorax (which is not its normal location) and, although denser, appears aerated, making it difficult to appreciate the significant atelectasis involving the left upper lobe. This sign occurs in chronic atelectasis of the left upper lobe, most often in lung cancer, but can also be seen in chronic bronchial stenosis and, nowadays, after placement of left upper lobe endobronchial valves (Figure 8). The Luftsichel sign does not typically occur in acute atelectasis of the left upper lobe, such as that due to mucus plugging.

A special mention should be made of the less commonly recognized right Luftsichel sign,[23,25] which consists of combined atelectasis involving the right upper and middle lobes, also related to non-acute obstructive processes such as malignancy. Like the typical Luftsichel sign, the superior segment of the right lower lobe is markedly displaced superiorly, creating a confusing imaging appearance in which there is still lucency in the upper portion of the corresponding hemithorax[23,26]. On chest radiography, there is a medial

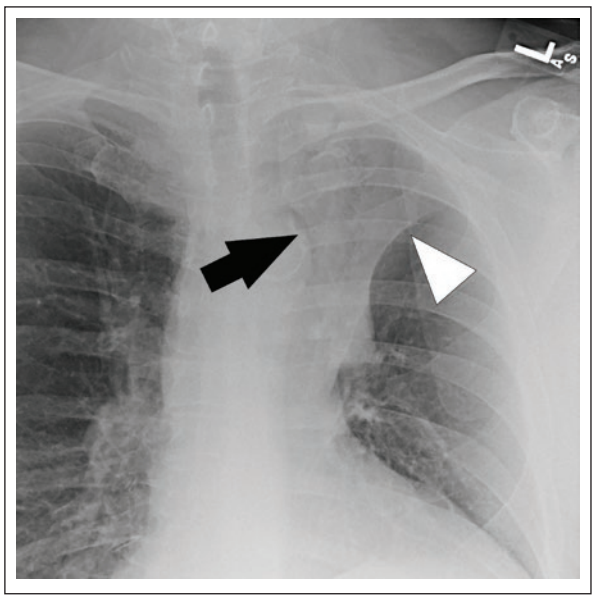

Figure 8. Patient with chronic left upper lobe atelectasis exhibiting the Luftsichel sign secondary to endobronchial valve placement. Frontal chest radiograph shows left upper lobe opacity. In this case, there is marked superior shift of the oblique fissure (arrowhead). Note crescentic lucency overlying the aortic arch (arrow), which constitutes the Luftsichel sign.

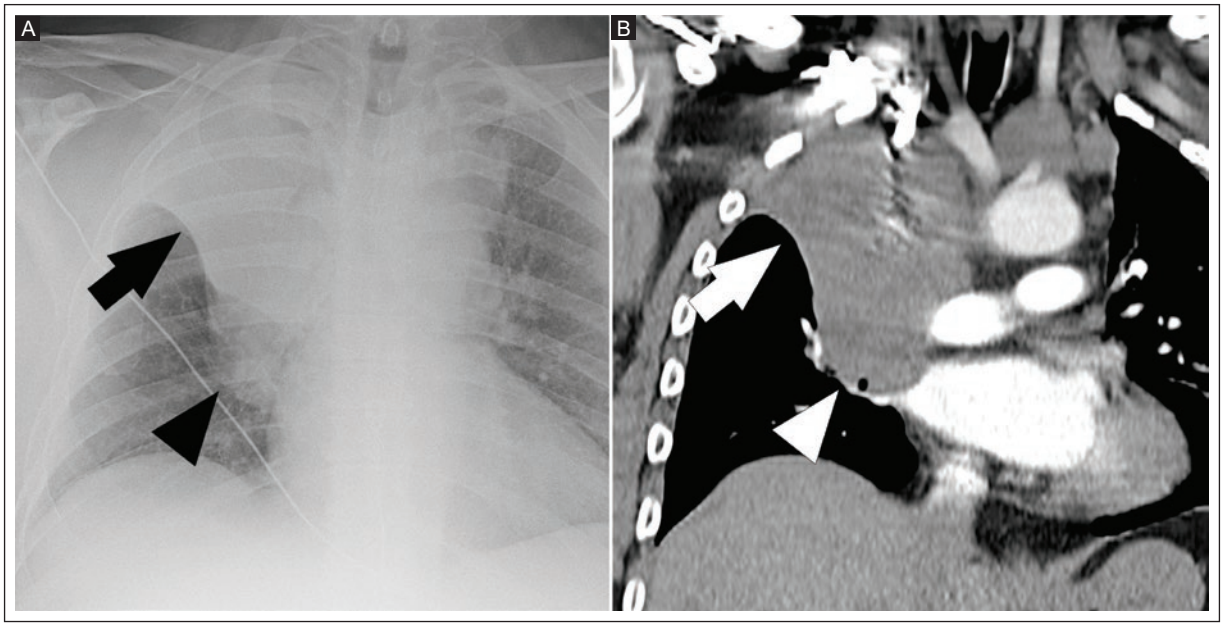

Figure 9. Patient with squamous cell lung cancer and the S of Golden sign. **A:** frontal chest radiograph shows opacity in the right upper hemithorax with a distinct superiorly directed convexity (arrow) and abnormal hilar convexity (arrowhead), the so-called S of Golden sign. **B:** coronal reformation of contrast-enhanced chest CT shows atelectatic right upper lobe (arrow) and right hilar mass (arrowhead). The principle of the S of Golden sign can be replicated on CT of any postobstructive atelectasis due to a central mass.

CT: computed tomography.

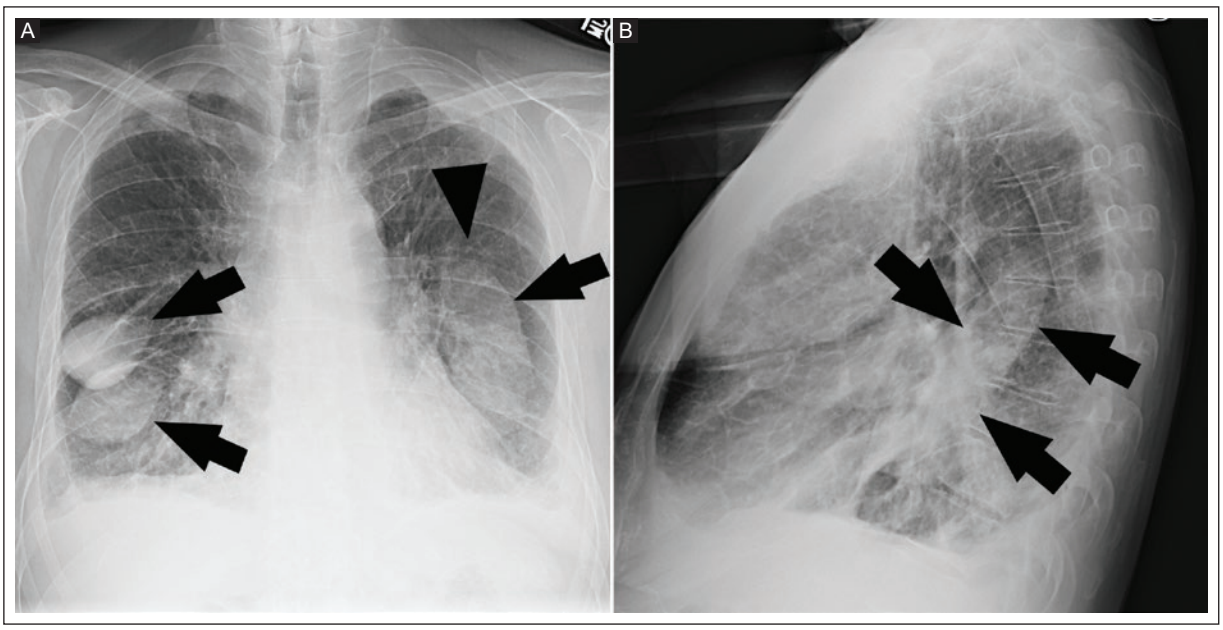

Figure 10. Patient with phantom tumors in the context of heart failure. **A:** frontal chest radiograph shows multiple mass-like opacities (arrows), distinctly overlying the fissural anatomy, with some, such as the left, exhibiting an incomplete border (arrowhead) sign indicating extrapulmonary location. **B:** lateral chest radiograph shows fusiform distribution of the opacity (arrows) along the expected course of the oblique fissure.

opacity that obscures the right mediastinal contour and fades laterally. However, similar to the left Luftsichel sign, if the superior segment of the right lower lobe is significantly displaced superiorly, there may be significant lucency in the right upper hemithorax which is what makes the left Luftsichel sign somewhat counterintuitive and difficult to diagnose.

S OF GOLDEN SIGN

This distinctive sign, predominantly seen in chronic right upper lobe atelectasis, is almost exclusively secondary to hilar malignancy. Although slightly more intuitive than the Luftsichel sign, the S of Golden sign is also gestaltic and often requires visual observation before a definitive diagnosis can be made. The S sign is a morphological description provided by Golden[27], sometimes referred to as the "reverse S of Golden," in which the lateral superior convexity is formed by superior displacement of the horizontal fissure, while the central inferior concavity represents the hilar mass[2,10,24,28-30]. Like the Luftsichel sign, the S of Golden sign is typically associated with longstanding obstruction and is not commonly seen in acute right upper lobe atelectasis (Figure 9). The concept of the S of Golden is significant, as the same principle can be applied to CT, yielding similar implications[31], not only for obstructive collapse of the right upper lobe. Thus, any central obstructive mass will create a convexity, and its downstream atelectasis will exhibit a concavity, often delineated by the displaced adjacent fissure.

VANISHING OR PHANTOM TUMOR AND THE INCOMPLETE BORDER SIGN

A widely recognized phenomenon popularized by Felson is the vanishing tumor, also known as the phantom or pseudotumor, which refers to localized effusion along one of the fissures. This condition is common in heart failure and typically resolves rapidly as the patient's condition improves. Felson described this phenomenon as follows[2]: *"Interlobar effusion is encountered most commonly in heart failure… may cast a sharply marginated elliptical or circular shadow which, on frontal roentgenogram, may closely resemble a solid tumor. As the cardiac status improves, rapid regression can occur*". This finding can be mistaken for collapse, consolidation, or tumor. The diagnosis is primarily suspected because the mass overlies the expected course of the oblique or horizontal fissures (Figure 10). Most cases are right-sided. Cases may be challenging on frontal radiography, but the lateral projection is often helpful by locating the abnormality along the normal course of the fissures and because

the collections tend to be elongated or exhibit tapering ends (i.e. acute angles)[32-35].

A more pertinent corollary of the above is the so-called incomplete border sign, which can be instrumental in distinguishing extrapulmonary masses from those originating in the lungs[36-40]. Masses of pulmonary origin tend to be circular or rounded and fully surrounded by air (except those abutting the pleural surface); thus, their margins tend to be well defined along the entire perimeter in both radiographic projections (e.g., pulmonary cancer or abscess). In contrast, extraparenchymal masses (i.e., arising from the pleura or chest wall) tend to have one well-defined border and another poorly defined, referred to as the incomplete border sign. This is typically due to air (from the lungs or externally) outlining a portion of the mass, while the other border is silhouetted by soft tissues. The principle applies to extrapleural lesions such as those of the pleura and chest wall, with the caveat that some pulmonary parenchymal lesions abutting the pleura may falsely exhibit this sign.

CONCLUSION

Chest radiography remains the most widely performed imaging examination and continues to serve as the foundation of thoracic diagnostic evaluation. Despite technological advances in cross-sectional imaging, its accessibility, efficiency, and clinical impact ensure its enduring relevance. The apparent decline in interpretive emphasis does not indicate diminished importance but rather a shift in educational and professional priorities that now requires deliberate correction. Chest radiography is a technically unique modality that demands a specific interpretive framework grounded in both physical principles and pattern recognition. The diagnostic concepts articulated by pioneers such as Benjamin Felson – including gestalt-based recognition and classic radiographic signs – remain essential tools for accurate interpretation. These principles cannot be acquired passively; they require structured teaching, repeated exposure, and intentional practice.

Reinvesting in the mastery of chest radiograph interpretation is not merely an educational preference but a professional responsibility. Strengthening training in this area will enhance diagnostic accuracy, support efficient clinical decision-making, and ultimately improve patient outcomes. In an era of expanding technological capability, disciplined interpretation of the most fundamental imaging examination remains an indispensable skill that radiology must actively preserve and advance.

Funding

The authors declare that they have not received funding.

Conflicts of interest

The authors declare no conflicts of interest.

Ethical considerations

Protection of human subjects and animals. The authors declare that no experiments on humans or animals were performed for this research.

Confidentiality, informed consent, and ethical approval. This study does not involve personal patient data, medical records, or biological samples, and does not require ethical approval. SAGER guidelines do not apply.

Declaration on the use of artificial intelligence. The author declares that an AI tool (Apple) was used for orthographic and stylistic corrections of the manuscript.

REFERENCES

1. Smith-Bindman R, Chu PW, Azman-Firdaus HA, Stewart C, Malekhedayat M, Alber S, et al. Projected lifetime cancer risks from current computed tomography imaging. JAMA Intern Med. 2025;185(6):710-719. doi:10.1001/jamainternmed.2025.0505. Erratum in: JAMA Intern Med. 2025;185(6):747. doi: 10.1001/jamainternmed.2025.2355.
2. Felson B. Chest roentgenology. Philadelphia: W.B. Saunders Company; 1973.
3. Koontz NA, Gunderman RB. Gestalt theory: implications for radiology education. Am J Roentgenol. 2008;190(5):1156-1160. doi:10.2214/ajr.07.3268. Erratum in: AJR Am J Roentgenol. 2008;190(6):1430.
4. Applegate KE, Neuhauser DVB. Whose aunt minnie? Radiology. 1999;211(1):292. doi:10.1148/radiology.211.1.r99ap22292.
5. Greenberg LW. Aunt minnie: will inexperienced trainees recognize her? Arch Pediatr Adolesc Med. 1999;153(8):893-894. doi:10.1001/archpedi.153.8.893-c.
6. Cunningham AS, Blatt SD, Fuller PG, Weinberger HL. The art of precepting: Socrates or aunt minnie? Arch Pediatr Adolesc Med. 1999;153(2):114-116. doi:10.1001/archpedi.153.2.114.
7. George PP, Irodi A, Nidugala Keshava S, Lamont AC. 'Felson Signs' revisited. J Med Imaging Radiat Oncol. 2014;58(1):64-74. doi: 10.1111/1754-9485.12031.
8. Longuet R, Phelan J, Tanous H, Bushong S. Criteria of the Silhouette Sign. Radiology. 1977;122(3):581-585. doi:10.1148/122.3.581.
9. Felson B, Felson H. Localization of intrathoracic lesions by means of the postero-anterior roentgenogram: the silhouette sign. Radiology. 1950;55(3):363-374. doi:10.1148/55.3.363.
10. Algin O, Gokalp G, Topal U. Signs in chest imaging: a pictorial review. Diagn Interv Radiol. 2009;17(1):18-29. doi:10.4261/1305-3825.dir.2901-09.1.
11. Madhyastha SP, Reddy CT, Acharya RV, Seshadri S. Silhouette sign revisited. BMJ Case Rep. 2020;13(9):e239033. doi:10.1136/bcr-2020-239033.
12. Bertwistle AP. The silhouette radiogram in the interpretation of clinical signs. Postgrad Med J. 1926;2(13):13-14. doi:10.1136/pgmj.2.13.13.
13. Louw VJ, Schmidt A, Bolliger CT. The silhouette sign revisited. Respiration. 2000;67(1):89. doi:10.1159/000029469.
14. Ludeña T, Lozano-Samaniego A, Maldonado S, Salas F. The hilum of the lung: two classical radiological signs to decipher it. Radiologia (Engl Ed). 2022;64(1):60-68. doi:10.1016/j.rxeng.2020.09.005.

15. Sarkar S, Jash D, Maji A, Patra A. Approach to unequal hilum on chest X-ray. J Assoc Chest Physicians. 2013;1(2):32-37. doi:10.4103/2320-8775.123204.
16. Daves ML. Skiagraphing the mediastinal moguls. New Physician. 1970; 19:49-54.
17. Daves ML. Cardiovascular anachronisms: phrases and concepts that should disappear but haven't. JAMA. 1973;224(6):879-883. doi: 10.1001/jama.224.6.879.
18. Kandachar PS, Varughese NA, Kaur C, Farqani AMA, Al Lawati AA. Mogul in a Baby. Sultan Qaboos Univ Med J. 2023;23(5):71-73. doi: 10.18295/squmj.12.2023.071.
19. Kamiya S, Nishizawa T, Arioka H. Cervicothoracic sign of mediastinal goitre. BMJ Case Rep. 2023;16(12):e258963. doi:10.1136/bcr-2023-258963.
20. Mu SYM, Fok JS. Luftsichel sign. J R Coll Physicians Edinb. 2023; 53(3):179-180. doi:10.1177/14782715231188986.
21. Sriram PS, Biswas A. Luftsichel sign and juxtaphrenic peak sign. BMJ Case Rep. 2015;2015:bcr2015210302. doi:10.1136/bcr-2015-210302.
22. Boira-Enrique I, Esteban-Ronda V, Chiner-Vives E. The Luftsichel sign is still in effect. Open Respir Arch. 2024;6(1):100305. doi: 10.1016/j.opresp. 2024.100305.
23. Blankenbaker DG. The Luftsichel sign. Radiology. 1998;208(2):319-320. doi:10.1148/radiology.208.2.9680553.
24. Proto AV, Tocino I. Radiographic manifestations of lobar collapse. Semin Roentgenol. 1980;15(2):117-173. doi:10.1016/0037-198x(80)90004-8.
25. Webber M, Davies P. The Luftsichel: an old sign in upper lobe collapse. Clin Radiol. 1981;32(3):271-275. doi:10.1016/s0009-9260(81)80036-0.
26. Lee KS, Logan PM, Primack SL, Müller NL. Combined lobar atelectasis of the right lung: imaging findings. AJR Am J Roentgenol. 1994;163(1): 43-47. doi:10.2214/ajr.163.1.8010243.
27. Golden R. The effect of bronchostenosis upon the roetgen-ray shadows in carcinoma of the bronchus. AJR Am J Roentgenol. 1925;13:21-30.
28. Gupta P. The Golden S sign. Radiology. 2004;233(3):790-791. doi: 10.1148/radiol.2333021407.
29. Bunkar ML, Takhar R, Arya S, Biswas R. Golden 'S' sign. BMJ Case Rep. 2014;2014:bcr2014207844. doi:10.1136/bcr-2014-207844.
30. Lemyze M, Grunderbeeck NV, Gasan G, Thevenin D. Golden S sign. Am J Respir Crit Care Med. 2011;183(1):131. doi:10.1164/rccm.201009-1505IM.
31. Reinig JW, Ross P. Computed tomography appearance of Golden's "S" sign. J Comput Tomogr. 1984;8(3):219-223. doi:10.1016/0149-936x(84)90065-1.
32. David R, Edwin G, Alphonce B, Kusima H. A Vanishing lung tumor in congestive heart failure. Clin Case Rep. 2025;13(10):e71136. doi:10.1002/ccr3.71136.
33. Lozo M, Lozo Vukovac EL, Ivancevic Z, Pletikosic I. Phantom tumor of the lung: localized interlobar effusion in congestive heart failure. Case Rep Cardiol. 2014;2014(1):207294. doi:10.1155/2014/207294.
34. Kabnick EM, Sobo S, Cooper C, Alexander LL. Vanishing lung tumor. J Natl Med Assoc. 1985;77(3):229-230.
35. Antonio FA, Edavalath M, Pappachan JM. Vanishing tumor of the lung. Oman Med J. 2015;30(3):223. doi:10.5001/omj.2015.47.
36. Mendelson E. Abdominal wall masses: the usefulness of the incomplete Border sign. Radiol Clin North Am.1964;2:161-166.
37. Huang KY, Shen TC, Tu CY. Incomplete border sign. QJM Int J Med. 2013;106(9):871-872. doi:10.1093/qjmed/hct110.
38. Catalano O. The incomplete Border sign. Radiology. 2002;225(1): 129-130. doi:10.1148/radiol.2251010926.
39. Ellis R. Incomplete Border sign of extrapleural masses. JAMA. 1977; 237(25):2748. doi:10.1001/jama.1977.03270520058027.
40. Hsu CCT, Henry TS, Chung JH, Little BP. The incomplete Border sign. J Thorac Imaging. 2014;29(4):W48. doi:10.1097/rti.0000000000000088.

JMeXFRI

Journal of the Mexican Federation of Radiology and Imaging

Check for updates

FULL RESEARCH ARTICLE

Mdprostate AI and radiologist performance and interobserver agreement using bpMRI to predict the likelihood of prostate cancer based on PI-RADS

Eduardo Valencia-Segura, Beatriz Elias-Perez, Arturo Hernandez-Medina and Francisco J. Omaña-Villagran*

Department of Magnetic Resonance Imaging, Hospital Angeles Lomas, Huixquilucan, State of Mexico, Mexico

ABSTRACT

Introduction: *Artificial intelligence (AI) has improved the diagnostic performance of prostate magnetic resonance imaging (MRI) and reduced interobserver variability in Prostate Imaging Reporting and Data System (PI-RADS) scores. This study compared the diagnostic performance of a radiologist and mdprostate AI, using biparametric (bp) MRI, for predicting the likelihood of clinically significant prostate cancer (csPCa) based on PI-RADS scores and assessed interobserver agreement.* **Materials and methods:** *This retrospective cross-sectional study included patients who underwent bpMRI for suspected prostate cancer. bpMRI scans were analyzed using PI-RADS v2.1 by an experienced radiologist and mdprostate. Prostate lesions were classified as low (PI-RADS 1 to 3) or high/very high (PI-RADS 4 to 5) likelihood of csPCa. Sensitivity, specificity, positive and negative predictive values, likelihood ratios, and accuracy were calculated. Cohen's kappa coefficient was used to assess interobserver agreement, and Bowker's test of symmetry was used to analyze systematic differences in ordinal PI-RADS scoring.* **Results:** *Eighty-two men with a mean age of 64 ± 9.9 years (range 43-85) were included. The mean PSA was 9.9 ± 10.3 ng/mL. Mdprostate showed a sensitivity of 96.3%, specificity of 89.1%, and overall accuracy of 91.5% in predicting high and very high likelihood of csPCa, with the radiologist as the gold standard. Interobserver agreement between the radiologist and mdprostate was almost perfect (k = 0.81; 95% CI, 0.67-0.96). Bowker's test showed significant differences in PI-RADS categories (p = 0.017), indicating that mdprostate tended to assign higher PI-RADS scores than the radiologist, particularly for PI-RADS 5 lesions.* **Conclusion:** *Mdprostate demonstrated high diagnostic performance compared to the radiologist and near-perfect agreement between both, using bpMRI to predict a high or very high likelihood of csPCa based on PI-RADS assessment.*

Keywords: *Prostate cancer. Artificial intelligence. Biparametric magnetic resonance imaging. Mdprostate. Prostate Imaging Reporting and Data System.*

INTRODUCTION

Prostate cancer is one of the most common male malignancies worldwide, and an important cause of morbidity and mortality, ranking fourth globally with 1.4 million cases[1]. Prostate biparametric magnetic resonance imaging (bpMRI), based on T2-weighted (T2W), diffusion-weighted imaging (DWI), and apparent diffusion coefficient (ADC) sequences, is faster and more cost-effective than multiparametric (mp) MRI, with comparable diagnostic performance for detecting prostate cancer[2,3]. Prostate MRI may exhibit high interobserver variability, even among experienced radiologists[4]. In this context, artificial intelligence (AI) is a valuable tool for detecting

***Corresponding author:**
Beatriz Elias-Perez
E-mail: betyelias@hotmail.com

Received for publication: 12-12-2025
Accepted for publication: 23-03-2026
DOI: 10.24875/JMEXFRI.M26000132

Available online: 08-07-2026
J Mex Fed Radiol Imaging. 2026;5(2):98-106
www.JMeXFRI.com

and characterizing prostate lesions, offering diagnostic performance comparable to that of expert radiologists with adequate reproducibility[5,6].

Commercial platforms designed for clinical integration, such as Quantib Prostate (2020), ProstatID (2022), mdprostate (2023), and QP-Prostate (2024), incorporate automated prostate segmentation, suspicious lesion detection, Prostate Imaging Reporting and Data System (PI-RADS) scoring, and structured reporting. These tools improve diagnostic sensitivity, optimize reading times, and especially assist radiologists with less experience in interpreting prostatic mpMRI[7-10]. Mdprostate (mediaire GmbH, Berlin, Germany) is an AI-based software designed to assist in interpreting prostate MRI using biparametric sequences, especially T2W, DWI, and ADC[8,11]. Mdprostate uses deep neural networks for automatic prostate segmentation, calculates quantitative parameters such as prostate volume, lesion dimensions, ADC values, and prostate-specific antigen (PSA) density, detects suspicious prostate lesions, classifies PI-RADS v2.1, and generates structured reports with sectorial maps integrated in the PACS.

Despite AI's high performance in bpMRI, its external validity and formal adoption need to be standardized, with potential biases arising from the training datasets used for the algorithms[9,10]. Several reviews on AI in MRI emphasize the need for multicenter, prospective validations before widespread clinical adoption[5,12]. This study compared the diagnostic performance of a radiologist and mdprostate AI using bpMRI to predict the likelihood of csPCa based on PI-RADS score and assessed interobserver agreement between the two.

MATERIALS AND METHODS

This cross-sectional study was conducted from January to October 2025 in the Department of Magnetic Resonance Imaging at Hospital Angeles Lomas, Huixquilucan, State of Mexico, Mexico. Adult men with PSA > 3 ng/mL who underwent prostate bpMRI were included. Patients with claustrophobia, incomplete bpMRI scans, studies with motion artifacts, or without a PI-RADS score generated by mdprostate were excluded. All participants provided written informed consent. The study was approved by the Institutional Research Ethics Committee and Research Committee.

Development and study variables

We recorded the patients´ age and PSA (ng/mL). The radiologist and mdprostate assigned a PI-RADS v2.1 score[13] on bpMRI using a five-point scale to indicate the likelihood of csPCa, with a score of 1 indicating a very low likelihood and a score of 5 indicating a very high likelihood. Individual scores were assigned to each sequence, with an overall score that summarized the likelihood of csPCa. In this study, the PI-RADS score was dichotomized as follows: PI-RADS of 1 to 3 indicated a low likelihood of csPCa; PI-RADS ≥ 4 indicated a high or very high likelihood of csPCa. The PI-RADS score agreement between the radiologist (EVS) with 5 years of MRI experience and mdprostate was assessed.

Imaging acquisition and data analysis protocol

bpMRI was performed on 1.5T MAGNETOM Aera or 3.0T MAGNETOM Skyra Fit equipment (Siemens Healthineers, Erlangen, Germany) with an 18-channel radiofrequency surface coil. A conventional T2W sequence was acquired in the axial plane and DWI ($b \geq 1500$ s/mm^2) with ADC map generation. Standard clinical acquisition parameters are shown in table 1.

After acquisition, the images were automatically transferred to the mdprostate software (Mediaire GmbH, Berlin, Germany) for analysis. Mdprostate generated a PI-RADS score, and the radiologist's evaluation was recorded.

Statistical analysis

Quantitative variables were analyzed with descriptive statistics. The Shapiro-Wilk test was used to assess the distribution of quantitative variables. Results were expressed as mean and standard deviation (SD). Diagnostic performance using the radiologist or mdprostate as the gold standard was assessed with sensitivity, specificity, positive predictive value (PPV), negative predictive value (NPV), positive and negative likelihood ratios, and accuracy. Inter-reader agreement between the radiologist and mdprostate was analyzed using Cohen's kappa, and Bowker's test of symmetry was used to evaluate systematic differences in paired ordinal PI-RADS scores. A p value < 0.05 was considered statistically significant. The analysis was performed with RKWard v0.8.0[14].

RESULTS

Eighty-two patients with a mean age of 64 ± 9.9 years (range 43-85) were included. The mean PSA value was 9.9 ± 10.3 ng/mL, with a median of 6.1 ng/mL (range 3.1-71.9 ng/mL).

Table 1. Prostate bpMRI protocol used by mdprostate AI

Field strength	Sequence	FOV (mm)	Matrix	TR (ms)	TE (ms)	b values [number of samples] (s/mm^2)	Slices/Slice thickness (mm)[a]
1.5T	Axial T2W TSE	220*220	266*320	5730	87	N/A	30/3.0
	Axial EPI DWI	220*220	110*110	6700	74	50 [2], 400 [5], 1600 [10], 2000[b]	30/3.0
3.0T	Axial T2W TSE	200*200	352*352	6000	105	N/A	25/3.0
	Axial EPI DWI	200*200	104*104	4600	75	50 [2], 800 [5], 1500 [14], 2000[b]	25/3.0

[a]No gap between slices; [b]Synthetic high b value was calculated by the scanner. DWI: diffusion-weighted imaging; EPI: echo planar imaging; FOV: field-of-view; MRI: magnetic resonance imaging; N/A: not applicable; T: tesla; TE: echo time; TI: inversion-recovery time; TR: repetition time; TSE: turbo spin echo; T2W: T2-weighted.

Comparison of PI-RADS scores assigned by the radiologist and mdprostate

Cases classified as PI-RADS 2 (n = 51, 62.2%) and PI-RADS 3 (n = 6, 7.3%) by the radiologist were comparable to those classified by mdprostate (n = 43, 52.4% and n = 5, 6.1%, respectively) (Table 2). The radiologist classified 14 (17.1%) and 11 (13.4%) cases as PI-RADS 4 and 5, respectively, while mdprostate classified 9 (11.0%) and 21 (25.6%) cases. The radiologist and mdprostate PI-RADS scores were compared using Bowker's test of symmetry with a significant difference (p = 0.017), indicating systematic differences in score assignment. Specifically, mdprostate classified more cases as higher (PI-RADS 5) than the radiologist. This difference is likely due to mdprostate's tendency to overestimate lesion segmentation. However, this overestimation was observed from categories 4 to 5 and does not directly impact the likelihood of csPCa.

Diagnostic performance of mdprostate using bpMRI, with the radiologist as the gold standard in predicting the likelihood of csPCa

Compared with the radiologist, mdprostate showed a sensitivity of 96.3% (95% CI: 92.1-100) and a specificity of 89.1% (95% CI: 82.3-95.8) for predicting high likelihood (PI-RADS 4) and very high likelihood (PI-RADS 5) of csPCa (Table 3). The PPV was 81.2%, and the NPV was 98.0%, reflecting a high probability that both positive and negative classifications were accurate. The diagnostic accuracy was 91.4% (95% CI: 85.4-97.5).

The positive likelihood ratio was 8.8 (4.1-18.9), indicating that a positive result strongly predicts csPCa. The negative likelihood ratio was 0.04 (0.01-0.29), indicating that negative results greatly reduce the probability of disease. Mdprostate tended to classify more cases as very high likelihood of csPCa (PI-RADS 5).

Table 2. Comparison of PI-RADS scores assigned by the radiologist and mdprostate in patients with suspicious prostate lesions

Score	Radiologist (n = 82)	Mdprostate (n = 82)
PI-RADS 1, n (%)	0	4 (4.9)
PI-RADS 2, n (%)	51 (62.2)	43 (52.4)
PI-RADS 3, n (%)	6 (7.3)	5 (6.1)
PI-RADS 4, n (%)	14 (17.1)	9 (11.0)
PI-RADS 5, n (%)	11 (13.4)	21 (25.6)

PI-RADS: Prostate Imaging Reporting and Data System.

Diagnostic performance of the radiologist using bpMRI, with mdprostate as the gold standard in predicting the likelihood of csPCa

The radiologist demonstrated high diagnostic performance compared to mdprostate (Table 4). Sensitivity was 81.2% (95% CI: 63.6-92.8), and specificity was 98.0% (95% CI: 89.3-99.9), indicating an excellent ability of the radiologist to identify true-negative cases. The PPV and NPV were 95.1% and 91.7%, respectively, reflecting a high probability that both positive and negative results were accurate. The accuracy was 92.6% (95% CI 84.7-97.2). The mean positive likelihood ratio was 40.6 (5.8-284.8), suggesting a strong ability to confirm disease, while the mean negative likelihood ratio was 0.19 (0.09-0.39), indicating a good ability to establish a negative diagnosis, though less strong than the positive ratio.

Interobserver agreement in PI-RADS scoring between the radiologist and mdprostate

There was strong concordance between the radiologist and mdprostate, with almost perfect agreement (k = 0.81, 95% CI 0.67-0.96) in assigning PI-RADS scores. The kappa values support the reliability of mdprostate in a

Table 3. Diagnostic performance of mdprostate using bpMRI, with the radiologist as the gold standard in predicting the likelihood of csPCa based on PI-RADS scores

Description	Parameter
Sensitivity, % (95% CI)	96.3 (92.1-100)
Specificity, % (95% CI)	89.1 (82.3-95.8)
PPV, % (95% CI)	81.2 (72.7-89.7)
NPV, % (95% CI)	98.0 (94.9-100)
LR+, mean (min-max)	8.8 (4.1-18.9)
LR–, mean (min-max)	0.04 (0.01-0.29)
Accuracy, % (95% CI)	91.4 (85.4-97.5)

AI: artificial intelligence; bpMRI: biparametric magnetic resonance imaging; csPCa: clinically significant prostate cancer; CI: confidence interval; LR+: positive likelihood ratio; LR–: negative likelihood ratio; NPV: negative predictive value; PI-RADS: Prostate Imaging Reporting and Data System; PPV: positive predictive value.

Table 4. Diagnostic performance of the radiologist using bpMRI, with mdprostate as the gold standard in predicting the likelihood of csPCa based on PI-RADS scores

Description	Parameter
Sensitivity, % (95% CI)	81.2 (63.6-92.8)
Specificity, % (95% CI)	98.0 (89.3-99.9)
PPV, % (95% CI)	95.1 (73.1-99.2)
NPV, % (95% CI)	91.7 (84.4-95.8)
LR+, mean (min-max)	40.6 (5.8-284.8)
LR–, mean (min-max)	0.19 (0.09-0.39)
Accuracy, % (95% CI)	92.6 (84.7-97.2)

AI: artificial intelligence; bpMRI: biparametric magnetic resonance imaging; csPCa: clinically significant prostate cancer; CI: confidence interval; LR+: positive likelihood ratio; LR–: negative likelihood ratio; NPV: negative predictive value; PI-RADS: Prostate Imaging Reporting and Data System; PPV: positive predictive value.

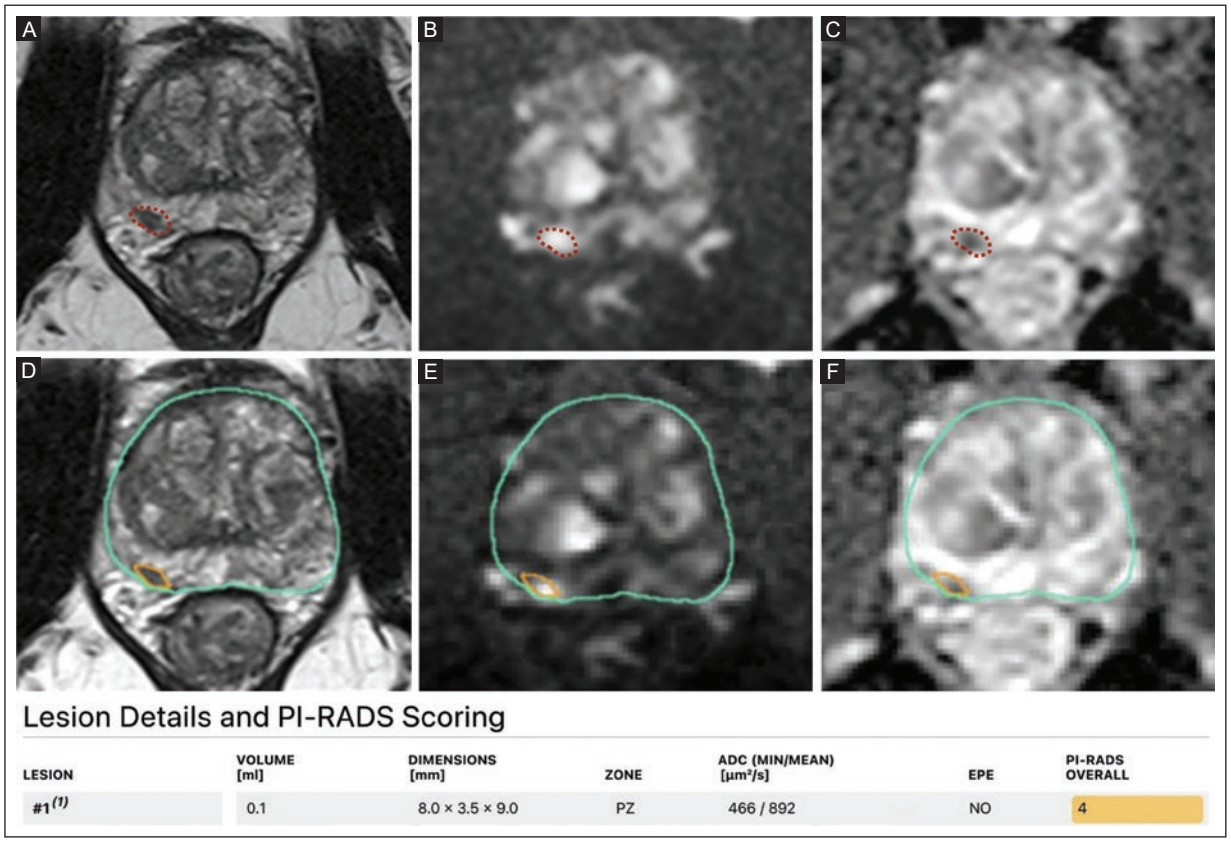

Figure 1. bpMRI of a 69-year-old man with an elevated PSA of 10 ng/mL. The upper panel shows the images assessed by the radiologist: **A:** T2W axial sequence shows a hypointense nodule (dashed line) with well-defined margins, measuring 8.2 mm × 3.6 mm × 6.4 mm along the transverse, anteroposterior, and longitudinal axes, respectively, with an estimated volume of 0.09 mL. The nodule is located in the right posterolateral PZ. **B:** an axial DWI sequence showing marked nodule hyperintensity (dashed line). **C:** ADC map shows marked hypointensity (dashed line) with a mean of 654 μm²/s (min 466, max 894), indicating diffusion restriction. The radiologist classified this nodule as PI-RADS 4. The lower panel shows images assessed by mdprostate: **D:** axial T2W sequence, **E:** axial DWI sequence, and **F:** ADC map. Mdprostate analysis shows segmentation of the prostate (green circle) and the nodule (orange circle). The data at the bottom show the prostate nodule volume, dimensions, zone, and ADC, with a PI-RADS score of 4. The histopathologic biopsy diagnosis of the nodule was prostate adenocarcinoma, Gleason 3 + 4. This case showed agreement between the radiologist and mdprostate on PI-RADS scoring.

ADC: apparent diffusion coefficient; bpMRI: biparametric prostate magnetic resonance imaging; DWI: diffusion-weighted imaging; PSA: prostate-specific antigen; PI-RADS: Prostate Imaging Reporting and Data System; PZ: peripheral zone; T2W: T2-weighted.

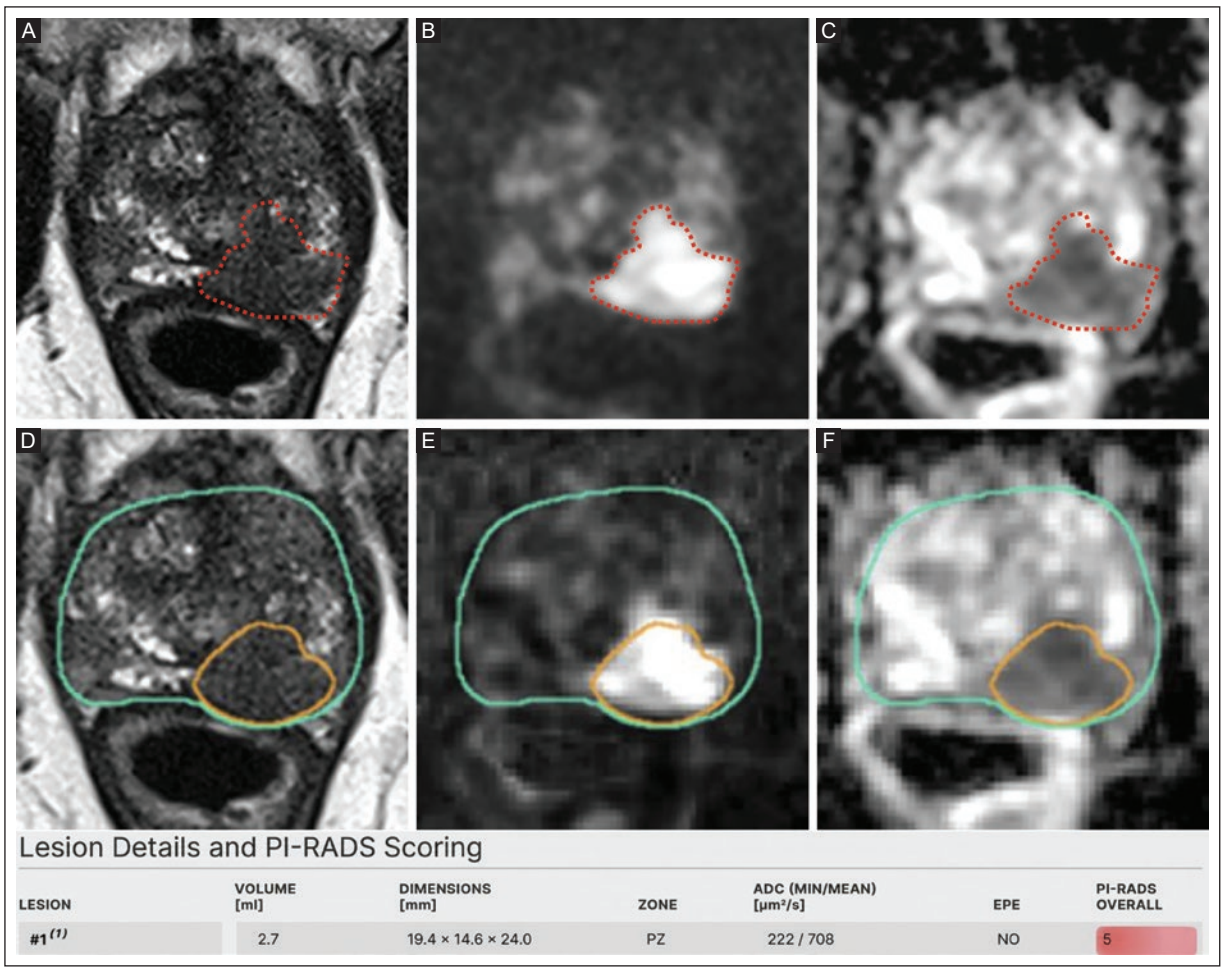

Figure 2. bpMRI of an 85-year-old man with an elevated PSA of 9.5 ng/mL. The upper panel shows the images assessed by the radiologist: **A:** T2W axial sequence shows a nodule with poorly defined margins (dashed line) that partially bulges the prostate capsule, measuring 21.1 mm × 7.2 mm × 16.3 mm along the transverse, anteroposterior, and longitudinal axes, respectively, with an estimated volume of 1.2 mL. The nodule is located in the left posterolateral and posteromedial PZ and extends into the left posterior TZ. **B:** axial DWI sequence shows marked hyperintensity within the nodule (dashed line). **C:** the ADC map shows marked hypointensity (dashed line) due to diffusion restriction, with a mean ADC of 544 μm^2/s (range 385-750). The radiologist classified the nodule as PI-RADS 5. The lower panel shows the images assessed by mdprostate: **D:** axial T2W sequence, **E:** axial DWI sequence, and **F:** ADC map. Analysis by mdprostate shows segmentation of the prostate (green circle) and nodule (orange circle). The data at the bottom show the volume, dimensions, prostate zone, and ADC of the prostate nodule, with a PI-RADS score of 5. This case showed agreement in PI-RADS scoring between the radiologist and mdprostate.

ADC: apparent diffusion coefficient; bpMRI: biparametric prostate magnetic resonance imaging; DWI: diffusion-weighted imaging; PSA: prostate-specific antigen; PI-RADS: Prostate Imaging Reporting and Data System; PZ: peripheral zone; T2W: T2-weighted; TZ: transition zone.

clinical setting, reinforcing that the likelihood of csPCa was accurately classified in both positive and negative cases when mdprostate was compared with the radiologist.

Figure 1 shows a bpMRI of a 69-year-old man with an elevated PSA of 10 ng/mL. A prostate nodule with marked hyperintensity on the DWI sequence is located in the right posterolateral peripheral zone (PZ). The ADC map shows marked hypointensity, with a mean of 654 μm^2/s, indicating diffusion restriction. The radiologist and mdprostate agreed and classified this nodule as PI-RADS 4. Histopathologic analysis of the nodule biopsy showed prostate adenocarcinoma, Gleason 3 + 4.

Figure 2 shows a bpMRI of an 85-year-old man with an elevated PSA of 9.5 ng/mL. A prostate nodule with marked hyperintensity on the DWI sequence is located in the left posterolateral and posteromedial PZ, extending into the left posterior transition zone (TZ). The ADC map shows marked hypointensity due to diffusion restriction, with a mean ADC of 544 μm^2/s. The radiologist and mdprostate agreed and classified the nodule as PI-RADS 5.

Figure 3 shows a bpMRI of a 62-year-old man with an elevated PSA of 40 ng/mL, fever, and dysuria. The T2W axial sequence shows homogeneous diffuse hypointensity in the TZ and PZ of both prostatic lobes,

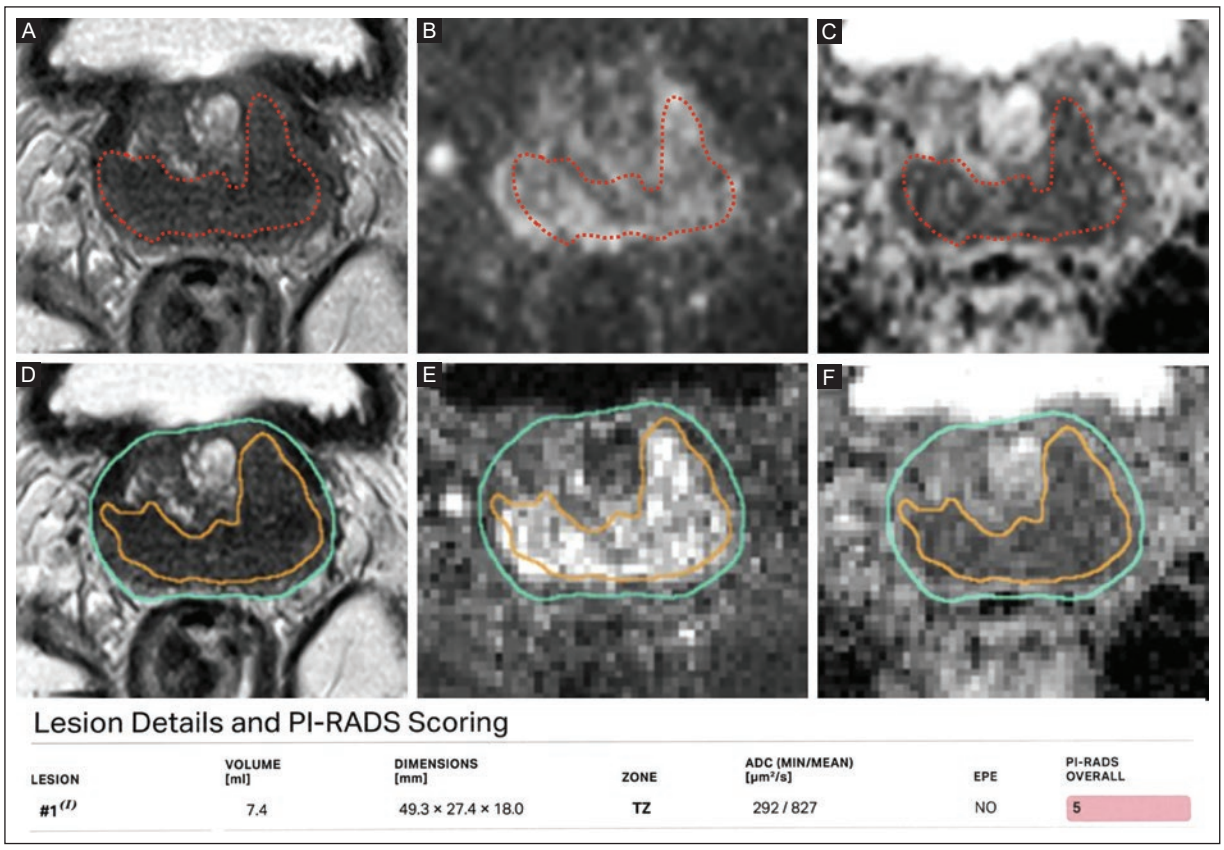

Figure 3. bpMRI of a 62-year-old man with fever, dysuria, and an elevated PSA of 40 ng/mL. The upper panel shows the images assessed by the radiologist: **A:** T2W axial sequence shows homogeneous diffuse hypointensity (dashed line) in the TZ and PZ of both prostate lobes, predominantly on the left, measuring 40 mm × 20.9 mm × 25.5 mm along the transverse, anteroposterior, and longitudinal axes, respectively, with an estimated volume of 11 mL. **B:** axial DWI sequence shows mild TZ and PZ hyperintensity of both prostate lobes, predominantly on the left (dashed line). **C:** ADC map shows marked TZ and PZ hypointensity of both prostatic lobes (dashed line), predominantly on the left, with restricted diffusion and a mean ADC of 762 $\mu m^2/s$ (range 520-984). The radiologist assigned a PI-RADS score of 2. The lower panel shows the images assessed by mdprostate: **D:** axial T2W sequence, **E:** axial DWI sequence, and **F**: ADC map. Analysis by mdprostate includes segmentation of the prostate (green line) and identification of a diffuse hypointense area on T2W (orange line). The data at the bottom show the volume, dimensions, prostate zone, and ADC of the prostate nodule, with a PI-RADS score of 5. A prostate abscess was ruled out. There was no agreement between the radiologist (PI-RADS score 2) and mdprostate (PI-RADS score 5). Based on clinical data, antibiotic treatment was administered, and symptoms resolved. Due to persistently elevated PSA, the patient underwent prostate biopsy, which showed acute prostatitis due to *Klebsiella pneumoniae* without evidence of malignancy.

ADC: apparent diffusion coefficient; bpMRI: biparametric prostate magnetic resonance imaging; DWI: diffusion-weighted imaging; PSA: prostate-specific-antigen; PI-RADS: Prostate Imaging Reporting and Data System; PZ: peripheral zone; T2W: T2-weighted. TZ: transition zone

predominantly on the left. The DWI sequence shows mild hyperintensity. The ADC map shows marked hypointensity in the TZ and PZ of both prostatic lobes, predominantly on the left, with restricted diffusion and a mean ADC value of 762 $\mu m^2/s$. There was no agreement between the radiologist (PI-RADS score 2) and mdprostate (PI-RADS score 5). The patient underwent prostate biopsy, which showed acute prostatitis due to *Klebsiella pneumoniae* without evidence of malignancy.

Figure 4 shows a bpMRI of a 63-year-old man with a PSA of 7.14 ng/mL and a small nodule with a poorly defined border in the right posteromedial PZ. The DWI axial sequence shows marked focal hyperintensity. The ADC map shows marked focal hypointensity (asterisk), indicating restricted diffusion with a mean ADC value of 638 $\mu m^2/s$. The radiologist assigned this nodule a PI-RADS score of 4. Mdprostate assigned the small nodule a PI-RADS 3 and segmented the nodule as larger than calculated by the radiologist. In the DWI sequence, this nodule showed marked restriction, and because it was in the peripheral zone, the radiologist assigned a PI-RADS score of 4. A targeted prostate biopsy was performed, and the histopathologic diagnosis was prostate adenocarcinoma.

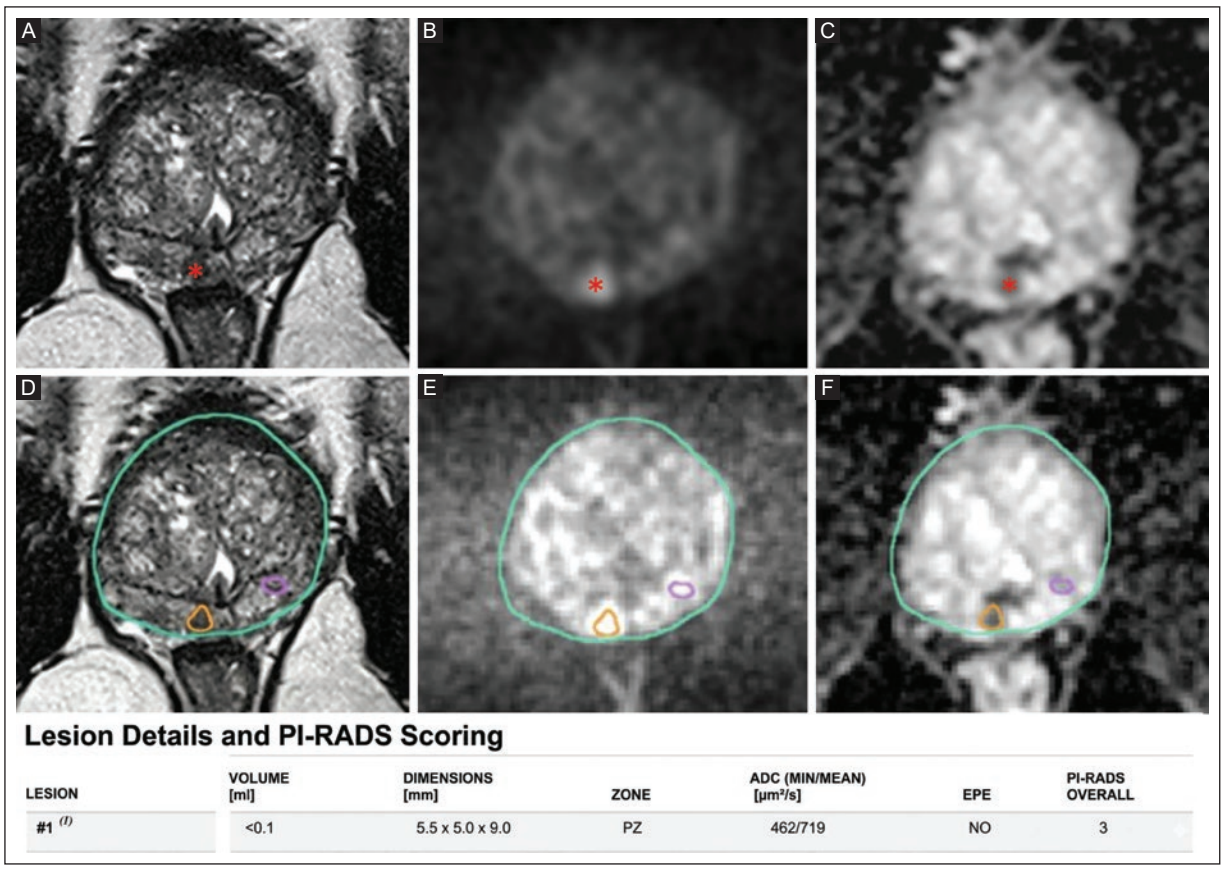

Figure 4. bpMRI of a 63-year-old man with a PSA of 7.14 ng/mL. The upper panel shows the images assessed by the radiologist: **A:** T2W axial sequence shows a nodule with poorly defined margins (asterisk) measuring 5.2 mm × 4.5 mm × 6.1 mm along the transverse, anteroposterior, and longitudinal axes, respectively, with an estimated volume of 0.07 mL. The nodule is located in the right posteromedial PZ. **B:** DWI axial sequence shows marked focal hyperintensity (asterisk). **C:** ADC map shows marked focal hypointensity (asterisk), indicating restricted diffusion, with a mean ADC of 638 $\mu m^2/s$ (range 509-917). The radiologist assigned this nodule a PI-RADS score of 4. The lower panel shows the images assessed by mdprostate: **D:** axial T2W sequence, **E**: axial DWI sequence, and **F**: ADC map. Analysis by mdprostate includes segmentation of the prostate (green line) and the nodule (orange line). The data at the bottom show the volume, dimensions, prostate zone, and ADC of the prostate nodule, with a PI-RADS score of 3. Additionally, a small nodule (purple line) was scored PI-RADS 2 by both the radiologist and mdprostate. A targeted prostate biopsy was performed, and histopathologic diagnosis was prostate adenocarcinoma, Gleason 3 + 3 (ISUP 1). The patient received HIFU treatment. Mdprostate assigned the nodule a PI-RADS 3 and segmented it as larger than the radiologist calculated. In the DWI sequence, this nodule showed marked restriction, and because it was in the peripheral zone, the radiologist assigned a PI-RADS score of 4.

ADC: apparent diffusion coefficient; bpMRI: biparametric prostate magnetic resonance imaging; DWI: diffusion-weighted imaging; HIFU: high-intensity focused ultrasound; ISUP: International Society of Urological Pathology; PSA: prostate-specific antigen; PI-RADS: Prostate Imaging Reporting and Data System; PZ: peripheral zone; T2W: T2-weighted.

DISCUSSION

Our study showed that mdprostate had high diagnostic performance compared to the radiologist using bpMRI in predicting a high or very high likelihood of csPCa based on the PI-RADS score. Interobserver agreement between the radiologist and mdprostate was almost perfect. Mdprostate can be used as a second reader for bpMRI to predict the likelihood of csPCa based on the PI-RADS score.

AI-based tools for prostate MRI demonstrate good diagnostic performance in detecting and classifying csPCa using the PI-RADS score. Multicenter studies demonstrate that AI systems achieve diagnostic performance comparable to or better than that of experienced radiologists[15,16]. Bayerl et al.,[8] using mdprostate and PI-RADS v2.1 in a retrospective study of 123 German men with suspected PCa, found that 53 (43.1%) did not have PCa, 15 (12.2%) had prostate cancer (Gleason score 6) and 55 (44.7%) had csPCa. PI-RADS ≥ 4 had a sensitivity of 85.5% and a specificity of 63.2%. PI-RADS 5 had a sensitivity of 88.7%. Results were comparable to those of an expert radiologist. Chen et al.[11] in a meta-analysis compared the performance

of various AI systems, including mdprostate versus radiologists in detecting csPCa in a multinational study with 20,423 patients from Asia, Europe, and the United States. Both 1.5T and 3.0T mpMRI scanners from various brands (Siemens, General Electric, and Philips) were used. AI systems showed diagnostic performance with a sensitivity of 87% and specificity of 61%, comparable to radiologists with a sensitivity of 85% and a specificity of 63% for detecting csPCa. In our study, mdprostate showed higher sensitivity (96.3%) than the radiologist (81.2%) in predicting the likelihood of csPCa based on PI-RADS using bpMRI, even higher than that reported by Bayerl et al.[8] and Chen et al.[11]. The high sensitivity observed in our study supports the clinical utility of mdprostate as a diagnostic tool in prostate bpMRI interpretation to accurately predict the likelihood of csPCa based on PI-RADS for suspicious prostate lesions.

AI software tends to overdiagnose, especially for PI-RADS 3 lesions, prostatitis, and benign prostatic hyperplasia, resulting in unnecessary biopsies[17]. In their meta-analysis, Chen et al.[11] reported that specificity is generally higher among radiologists, suggesting that increased lesion detection may lead to overclassification. The international Prostate Imaging-Cancer Artificial Intelligence (PI-CAI) project by Saha et al.[15] showed that certain AI algorithms can reduce false positives in detecting prostate cancer compared with specialized radiologists. AI software achieved performance that was not inferior to, and was even superior to, that of expert radiologists using PI-RADS v2.1 for csPCa in a multicenter, retrospective study of 10,207 prostate MRI scans from 9,129 patients in the Netherlands and Norway. Patients had suspected prostate lesions due to elevated PSA, abnormal digital rectal examination, or both. In total, 2,440 cases had csPCa confirmed by biopsy. Both 1.5T and 3.0T MRI equipment were used (Siemens Healthineers and Philips Medical Systems, respectively). The AI system was trained primarily with bpMRI, while radiologists evaluated mpMRI with PI-RADS v2.1. The AI was trained to prioritize detecting csPCa. AI software, including mdprostate, showed fewer false positives than radiologists (56 versus 113, respectively). The authors emphasize the ability of AI software to improve clinical specificity by achieving high detection of csPCa, reducing false positives, and lowering the risk of overdiagnosis. In our study, mdprostate demonstrated a tendency toward higher PI-RADS categorization, particularly for PI-RADS 5 lesions. The radiologist classified 11 (13.4%) cases, while mdprostate classified 21 (25.6%) cases. Therefore, specificity was lower for mdprostate (89.1%) compared to the radiologist (98.0%). This finding is consistent with the significant differences identified by Bowker's test and may reflect a diagnostic strategy of mdprostate to overestimate the PI-RADS score.

Previous reports have shown mild to high interobserver variability in PI-RADS classification, depending on the radiologist´s experience and MRI image quality[18,19]. Therefore, AI tools are proposed to improve the standardization and reproducibility of prostate cancer diagnosis. The multicenter study by Forookhi et al.[20] demonstrated that Quantib® Prostate software v2.0.1 (Quantib BV, Rotterdam, The Netherlands) improved agreement among less experienced radiologists. Cohen's Kappa showed excellent interobserver agreement between mdprostate and radiologists, using two categories: nonsuspicious (PI-RADS 1-3) and suspicious prostate cancer (4 and 5), and found improvement in PI-RADS assessment by less experienced radiologists. The multicenter PI-CAI study[15] reported that AI algorithms match or exceed the average performance of radiologists in detecting csPCa. Software such as mdprostate has demonstrated high concordance ($k > 0.80$), considered almost perfect. These results are consistent with reports that AI can be effectively integrated into clinical practice as a diagnostic support system, especially for less experienced radiologists, with reductions in false positives and less interobserver variability[8,15]. Our results showed comparable findings with almost perfect interobserver agreement ($k = 0.81$, 95% CI 0.67-0.96) between the radiologist and mdprostate in assigning PI-RADS scores. These findings support the evidence that AI-assisted prostate MRI interpretation with software such as mdprostate may serve as a reliable complementary tool to improve lesion detection, reduce diagnostic variability, and potentially facilitate more standardized reporting in clinical practice.

The main strength of our study is that it evaluated diagnostic performance and interobserver agreement of mdprostate, allowing a comprehensive assessment in a clinical setting, which is infrequent in the literature. However, the study has several limitations. First, this was a retrospective single-center study with a limited sample size, which may restrict the generalizability of the findings. Second, histopathological confirmation of prostate cancer was not available for all patients, limiting the use of the standard reference for the radiologist to evaluate the diagnostic performance of mdprostate. Third, a single radiologist performed the PI-RADS evaluation, so interobserver variability between radiologists was not assessed. Finally, two MRI scanners were used, which may have caused variability in image features.

CONCLUSION

Mdprostate demonstrated high diagnostic performance compared to the radiologist using bpMRI for the prediction of high and very high likelihood of csPCa based on the PI-RADS score. Additionally, agreement between the radiologist and mdprostate was almost perfect for PI-RADS scoring of prostate lesions. Implementing mdprostate as a second-reading tool may improve diagnostic standardization by prioritizing sensitivity over specificity[8]. Its progressive integration into clinical practice will likely play an increasingly important role in detecting and characterizing csPCa.

Acknowledgments

The authors thank Professor Ana M. Contreras-Navarro for her guidance in preparing and writing this scientific paper. This original research in the Radiology Specialty field was an awarded thesis at the Cuarta Convocatoria Nacional 2025-2026 “Las Mejores Tesis de Radiologia para Publicar en el JMeXFRI”.

Funding

The authors declare that they have not received funding.

Conflicts of interest

The authors declare no conflicts of interest.

Ethical considerations

Protection of human subjects and animals. The authors declare that the procedures followed were in accordance with the ethical standards of the responsible committee on human experimentation and with the World Medical Association and the Declaration of Helsinki (1964) and subsequent amendments.

Confidentiality, informed consent, and ethical approval. The authors have followed their institution’s confidentiality protocols. All participants provided written informed consent.

Declaration on the use of artificial intelligence. The authors declare that no generative artificial intelligence was used in the writing or creation of the content of this manuscript.

REFERENCES

1. Sung H, Ferlay J, Siegel RL, Laversanne M, Soerjomataram I, Jemal A, et al. Global Cancer Statistics 2020: GLOBOCAN Estimates of incidence and mortality worldwide for 36 cancers in 185 countries. CA Cancer J Clin. 2021;71(3):209-249. doi: 10.3322/caac.21660.
2. Kuhl CK, Schrading S, Enno-Edzard B, Heidenreich A, Katz-Brull R, Pickhardt PJ, et al. Abbreviated biparametric prostate MR imaging in men with elevated prostate-specific antigen. Radiology. 2017;285(2):493-505. doi: 10.1148/radiol.2017170129.
3. van der Leest M, Cornel E, Israël B, Hendriks R, Padhani AR, Hoogenboom M, et al. Head-to-head comparison of transrectal ultrasound-guided prostate biopsy versus multiparametric prostate resonance imaging with subsequent magnetic resonance-guided biopsy in biopsy-naïve men with elevated prostate-specific antigen: a large prospective multicenter clinical study. Eur Urol. 2019;75(4):570-578. doi: 10.1016/j.eururo.2018.11.023.
4. Rosenkrantz AB, Ginocchio LA, Cornfeld D, Froemming AT, Gupta RT, Turkbey B, et al. Interobserver reproducibility of the PI-RADS version 2 Lexicon: a multicenter study of six experienced prostate radiologists. Radiology. 2016;280(3):793-804. doi: 10.1148/radiol.2016152542.
5. Liu X, Faes L, Kale AU, Wagner SK, Fu DJ, Bruynseels A, et al. A comparison of deep learning performance against health-care professionals in detecting diseases from medical imaging: a systematic review and meta-analysis. Lancet Digit Health. 2019;1(6):e271-e297. doi: 10.1016/S2589-7500(19)30123-2.
6. Bhattacharya I, Khandwala YS, Vesal S, Shao W, Yang Q, Soerensen SJC, et al. A review of artificial intelligence in prostate cancer detection on imaging. Ther Adv Urol. 2022;14:17562872221128791. doi: 10.1177/17562872221128791.
7. Russo T, Quarta L, Pellegrino F, Cosenza M, Camisassa E, Lavalle S, et al. The added value of artificial intelligence using Quantib Prostate for the detection of prostate cancer at multiparametric magnetic resonance imaging. Radiol Med. 2025;130(7):1105-1114. doi: 10.1007/s11547-025-02017-8.
8. Bayerl N, Adams LC, Cavallaro A, Bäuerle T, Schlicht M, Wullich B, et al. Assessment of a fully-automated diagnostic AI software in prostate MRI: clinical evaluation and histopathological correlation. Eur J Radiol. 2024;181:111790. doi: 10.1016/j.ejrad.2024.111790.
9. Baydoun A, Jia AY, Zaorsky NG, Kashani R, Rao S, Shoag JE, et al. Artificial intelligence applications in prostate cancer. Prostate Cancer Prostatic Dis. 2024;27(1):37-45. doi:10.1038/s41391-023-00684-0.
10. Kim H, Kang SW, Kim JH, Nagar H, Sabuncu M, Margolis DJA, et al. The role of AI in prostate MRI quality and interpretation: opportunities and challenges. Eur J Radiol. 2023;165:110887. doi:10.1016/j.ejrad.2023.110887. Erratum in: Eur J Radiol. 2024;177:111585. doi: 10.1016/j.ejrad.2024.111585.
11. Chen H, Li E, Christos PJ, Zhu YS. Comparison of artificial intelligence and radiologists in MRI-based prostate cancer diagnosis: a meta-analysis of accuracy and effectiveness. Biomedicines. 2025;14(1):20. doi: 10.3390/biomedicines14010020.
12. Giganti F, Rosenkrantz AB, Villeirs G, Panebianco V, Stabile A, Emberton M, et al. The evolution of MRI of the prostate: The past, the present and the future. AJR Am J Roentgenol. 2019;213 (2):384-396. doi: 10.2214/AJR.18.20796.
13. Turkbey B, Rosenkrantz AB, Haider MA, Padhani AR, Villeirs G, Macura KJ, et al. Prostate imaging reporting and data system version 2.1: 2019 update of adherence to prostate imaging reporting and data system version 2. Eur Urol. 2019;76(3):340-351. doi: 10.1016/j.eururo.2019.02.033.
14. Friedrichsmeier T, and the RKWard Team (2024). RKWard: graphical interface to the statistical language R. Version 0.8.0. Available from: https://rkward.kde.org
15. Saha A, Bosma JS, Twilt JJ, van Ginneken B, Bjartell A, Padhani AR, et al. Artificial intelligence and radiologists in prostate cancer detection on MRI (PI-CAI): an international, paired, non-inferiority, confirmatory study. Lancet Oncol. 2024;25(7):879-887. doi: 10.1016/S1470-2045(24)00220-1.
16. Giganti F, Moreira da Silva N, Yeung M, Davies L, Frary A, Ferrer Rodriguez M, et al. AI-powered prostate cancer detection: a multi-centre, multi-scanner validation study. Eur Radiol. 2025;35(8):4915-4924. doi: 10.1007/s00330-024-11323-0.
17. Jensen LJ, Kim D, Elgeti T, Steffen IG, Schaafs LA, Haas M, et al. Detecting clinically significant prostate cancer in PI-RADS 3 lesions using T2w-derived radiomics feature maps in 3T prostate MRI. Curr Oncol. 2024;31(11):6814-6828. doi: 10.3390/curroncol31110503.
18. Wallström J, Thimansson E, Andersson J, Karlsson M, Zackrisson S, Bratt O, et al. An online national quality assessment survey of prostate MRI reading: interreader variability in prostate volume measurement and PI-RADS classification. Eur J Radiol Open. 2024;14:100625. doi: 10.1016/j.ejro.2024.100625.
19. Bhayana R, O’Shea A, Anderson MA, Bradley WR, Gottumukkala RV, Mojtahed A, et al. PI-RADS versions 2 and 2.1: interobserver agreement and diagnostic performance in peripheral and transition zone lesions among six radiologists. AJR Am J Roentgenol. 2021;217(1):141-151. doi: 10.2214/ajr.20.24199.
20. Forookhi A, Laschena L, Pecoraro M, Borrelli A, Massaro M, Dehghanpour A, et al. Bridging the experience gap in prostate multiparametric magnetic resonance imaging using artificial intelligence: a prospective multireader comparison study on inter-reader agreement in PI-RADS v2.1, image quality and reporting time between novice and expert readers. Eur J Radiol. 2023;161:110749. doi: 10.1016/j.ejrad.2023.110749.

JMeXFRI

Journal of the Mexican Federation of Radiology and Imaging

Check for updates

FULL RESEARCH ARTICLE

T2 relaxometry and cross-sectional area of the median nerve as quantitative MRI biomarkers in carpal tunnel syndrome

Beatriz Elias-Perez, Arturo Hernandez-Medina and Juan J. Mariño-Arevalo*

Department of Magnetic Resonance Imaging, Hospital Angeles Lomas, Huixquilucan, State of Mexico, Mexico

ABSTRACT

Introduction: *T2 relaxometry and cross-sectional area (CSA) values of the median nerve, assessed by magnetic resonance imaging (MRI) at various levels of the carpal tunnel have not been sufficiently evaluated in patients with carpal tunnel syndrome (CTS). This study aimed to assess the CSA and T2 relaxometry values of the median nerve at the proximal and distal levels of the carpal tunnel using MRI in Mexican patients with CTS.* **Material and methods:** *This case series included patients clinically diagnosed with CTS. Wrist 3.0T MRI scans were performed, and CSA and T2 relaxometry maps of the median nerve were obtained at the proximal (pisiform bone) and distal (hook of hamate bone) levels of the carpal tunnel. Age, weight, height, body mass index (BMI), and clinical severity and functional scores of CTS were recorded.* **Results:** *Twelve wrists from 10 patients with CTS were included. The mean CSA of the median nerve at the proximal level (12.7 ± 2.1 mm^2) was significantly higher than at the distal level (9.7 ± 1.9 mm^2; $p < 0.001$), with a large effect size (Cohen's $d = 1.43$). The mean T2 relaxation time was higher at the proximal level (64.7 ± 7.4 ms) than at the distal level (59.6 ± 7.8 ms; $p = 0.034$), with a moderate effect size (Cohen's $d = 0.70$). No significant correlations were observed between anthropometric measures and CSA, T2 relaxometry, or CTS clinical and functional scores.* **Conclusion:** *T2 relaxometry and CSA values of the median nerve on MRI showed regional variation, with significantly higher values at the proximal carpal tunnel level in patients with CTS. T2 relaxometry values at the proximal level were abnormally elevated compared with reference values from healthy Mexican subjects. T2 relaxometry and CSA are complementary biomarkers for assessing median nerve damage in CTS.*

Keywords: *Magnetic resonance imaging. Relaxometry. Median nerve. Carpal tunnel syndrome.*

INTRODUCTION

Carpal tunnel syndrome (CTS) is a common entrapment neuropathy caused by compression of the median nerve within the carpal tunnel, resulting in pain, paresthesia, or altered sensation. A small carpal tunnel area is considered a risk factor for CTS[1]. Morphological evaluation of the median nerve is performed with conventional magnetic resonance imaging (MRI) using standardized anatomical references for the carpal tunnel. Patients with CTS typically show an increased cross-sectional area (CSA), hyperintensity on T2-weighted images, and loss of fascicular architecture[2,3]. Advances in MRI technology, including high-field and multi-channel coils, provide robust signal-to-noise ratios, enabling quantitative imaging of peripheral nerves using techniques such as T2 relaxometry and diffusion imaging[4]. T2 relaxometry has been proposed as a sensitive biomarker for detecting microstructural alterations, allowing differentiation between affected and unaffected nerve segments[4-7].

***Corresponding author:**
Beatriz Elias-Perez
E-mail: beatriz.elias@saludangeles.mx

Received for publication: 11-12-2025
Accepted for publication: 13-02-2026
DOI: 10.24875/JMEXFRI.M26000131

Available online: 08-07-2026
J Mex Fed Radiol Imaging. 2026;5(2):107-115
www.JMeXFRI.com

Integrating morphometric parameters, such as CSA, with quantitative T2 relaxometry improves diagnostic accuracy and characterization of nerve damage in patients with CTS[8]. T2 relaxometry may vary with magnetic field strength (1.5T versus 3.0T), the sequence used, the anatomical level, and individual factors such as age, sex, and body mass index (BMI)[9]. Disorders such as a bifid median nerve can alter measurements if not properly recognized.

There are no established diagnostic cut-off points for CSA and T2 relaxometry that differentiate healthy subjects from patients with CTS. A T2 relaxometry value of 58.8 ms at the proximal carpal tunnel level of the median nerve was reported in a previous study of healthy Mexican subjects[10]. Higher CSA and T2 relaxometry values have been reported in patients with CTS compared with healthy individuals[5]. The aim of this study was to assess CSA and T2 relaxometry values of the median nerve at the proximal and distal levels of the carpal tunnel using MRI in Mexican patients with CTS.

MATERIAL AND METHODS

This case series was conducted from June to November 2025 in the Magnetic Resonance Department of Hospital Angeles Lomas in Huixquilucan, State of Mexico, Mexico. Adult patients with a clinical diagnosis of CTS referred by neurology or neurosurgery specialists were included. Patients with metal implants, movement disorders, claustrophobia, incomplete or low-quality MRI, or prior wrist surgery were excluded. Written informed consent was obtained from all participants. The study was approved by the institutional Ethics and Research Committee.

Study development and variables

Data on sex, age, weight, height, BMI, occupational activity, and median nerve laterality were recorded. CSA and T2 relaxation time color maps at the proximal and distal carpal tunnel levels were obtained. CSA reference values were based on data reported by Middleton et al.[11]. At the proximal carpal tunnel level, the CSA reference value was ≤ 7 mm². At the distal level, it was ≤ 8 mm². The T2 relaxation time at the proximal carpal tunnel level was based on Castro-Teran et al.[10] with a mean of 58.8 ms in healthy Mexican subjects. No reference value was defined for T2 relaxation time at the distal carpal tunnel level.

Symptoms and functional status were assessed using the Boston Carpal Tunnel Questionnaire (BCTQ)[12], a disease-specific measure that includes a self-reported symptom severity scale (SSS) with 11 questions rated on a five-point scale and a functional status scale (FSS) with 8 items rated for degree of difficulty on a five-point scale.

Imaging acquisition and analysis protocol

Wrist MRI scans were performed on a 3.0T MAGNETOM Skyra Fit (Siemens Healthineers, Erlangen, Germany). Images were acquired at the wrist using a 16-channel radiofrequency hand/wrist coil. The protocol included two sequences for the median nerve: T2 turbo spin-echo (TSE) and isotropic coronal T2-weighted multiple-echo data image combination (MEDIC), and an axial T2 map spin-echo multi-echo image for relaxometry time quantification. The relaxometry images were automatically processed by the system, yielding two image series: a grayscale T2 map and a color map.

T2 MEDIC images were analyzed to determine nerve position, and the proximal and distal nerve levels were localized on both grayscale and T2 color map images. The color map was merged with the grayscale image using syngo.via software (Siemens Healthineers, Erlangen, Germany). The median nerve was assessed at the pisiform bone for the proximal level and at the hook of the hamate bone for the distal level. A region of interest (ROI) of 2.5 to 3.0 mm^2 was manually outlined, and the mean relaxation time across all pixels within each ROI was calculated.

Statistical analysis

All measures of central tendency were obtained at both carpal tunnel levels. The Shapiro-Wilk normality test was performed, and the p value was < 0.05, indicating normal distributions for CSA and T2 relaxation time of the median nerve at the proximal and distal carpal tunnel levels. Inferential analysis of the ROI and comparison with published reference values for CSA[11] and T2 relaxometry[10] were performed using Student's *t*-test. Cohen's d values were calculated for each test to quantify effect size and provide a standardized difference between means[13]. Pearson correlation coefficients were calculated between the proximal and distal carpal tunnel levels and between age, height, weight, BMI, SSS, and FSS. A p value < 0.05 was considered significant for all tests. RKWard v0.8.0 software was used for the analysis[14].

Table 1. Characteristics of patients with CTS and quantitative values of median nerve CSA and T2 relaxometry using wrist MRI

Case	Sex	Age (years)	Weight (kg)	Height (meters)	BMI (kg/m^2)	BMI category	Occupational activity	Laterality	Median nerve					
									BCTQ		CSA		T2 relaxometry	
									SSS	FSS	Proximal (mm^2)	Distal (mm^2)	Proximal (ms)	Distal (ms)
1[a]	w	52	70	1.65	25.7	Overweight	Housework	Left	2.0	1.6	10.8	6.3	70.78 ± 2.64	59.25 ± 5.38
2	w	52	70	1.65	25.7	Overweight	Housework	Right	2.7	2.1	11.1	7.2	76.64 ± 3.03	68.67 ± 3.18
3	w	61	47	1.56	19.3	Normal	Housework	Right	2.1	1.0	15.7	9.5	71.30 ± 5.60	71.60 ± 5.78
4	m	49	77	1.63	29.0	Overweight	Radiologist	Right	2.0	1.1	14.2	11.6	55.25 ± 0.96	65.86 ± 5.52
5	m	42	72	1.64	26.8	Overweight	Technician	Right	1.6	1.3	8.8	8.3	60.50 ± 2.55	60.86 ± 3.78
6[b]	w	50	60	1.56	24.7	Normal	Accountant	Right	2.5	1.5	14.2	11.8	61.21 ± 5.07	60.86 ± 3.78
7	w	50	60	1.56	24.7	Normal	Accountant	Left	2.5	1.6	13.7	10.1	61.57 ± 3.92	54.38 ± 4.37
8	w	70	62	1.63	23.3	Normal	Nurse	Left	3.4	4.1	11.6	8.7	66.30 ± 6.55	48.17 ± 3.59
9	w	38	50	1.57	20.3	Normal	Housework	Right	2.0	1.6	11.1	11.2	55.87 ± 6.46	48.60 ± 3.85
10	w	48	70	1.56	28.8	Overweight	Secretary	Right	2.3	1.9	15.5	9.3	75.79 ± 3.33	66.14 ± 4.07
11	m	37	120	1.83	35.8	Obesity[c]	Physician	Right	1.2	1.0	12.0	9.3	57.50 ± 5.24	50.64 ± 1.91
12	w	35	51	1.53	21.8	Normal	Nurse	Right	2.2	1.9	13.1	12.8	63.57 ± 7.09	60.29 ± 4.84

[a]Cases 1 and 2 are the same patient with bilateral CTS. [b]Cases 6 and 7 are the same patient with bilateral CTS. [c]Grade 2 obesity. BCTQ: Boston Carpal Tunnel Questionnaire; BMI: body mass index; CTS: carpal tunnel syndrome; CSA: cross-sectional area; FSS: functional status scale; m: man; MRI: magnetic resonance imaging; SSS: symptom severity scale; w: woman.

RESULTS

Twelve wrist MRIs from 10 patients with CTS were included, comprising 7 women and 3 men. Data for each patient are shown in table 1. The mean age was 48.2 ± 11.1 years. The mean weight was 67.9 ± 21.0 kg, the mean height was 1.61 ± 0.08 meters, and the mean BMI was 25.5 ± 4.9 kg/m^2. The mean SSS was 2.2 ± 0.5, indicating moderate symptom severity, and the mean FSS was 1.7 ± 0.8, suggesting mild functional impairment.

Comparison of median nerve CSA and T2 relaxometry at the proximal and distal carpal tunnel levels using MRI in patients with CTS

The mean CSA at the proximal carpal tunnel level was higher (12.7 ± 2.1 mm^2) than at the distal level (9.7 ± 1.9 mm^2, $p < 0.001$) (Table 2). The median nerve CSA showed a mean difference of 3.0 mm^2 between the proximal and distal levels ($p < 0.001$), with a large effect size (Cohen's d = 1.43). The coefficients of variation were comparable between the two levels (0.17 and 0.15, respectively), indicating similar proportional variability across the two segments evaluated.

The proximal level had a higher mean T2 relaxometry value than the distal level (64.7 ± 7.4 ms versus 59.6 ± 7.8 ms, respectively; $p = 0.034$), with a mean difference of 5.1 ms and a moderate effect size (Cohen's d = 0.70). The mean difference in T2 relaxometry between the proximal and distal median nerve was significant. The coefficients of variation for T2 relaxometry values at both levels were comparable (0.11 and 0.12, respectively), indicating similar proportional variability between the two segments evaluated. The difference between the means of the median nerve T2 relaxometry varied according to the level measured, with different values between proximal and distal levels. Figure 1 shows a

Table 2. Comparison of median nerve CSA and T2 relaxometry at the proximal and distal carpal tunnel levels using wrist MRI in patients with CTS

Description	n	Mean	SD	Min	Max	Coefficient of variation	Mean difference	p	Cohen's d
Median nerve CSA									
Proximal level, mm^2	12	12.7	2.1	8.8	15.7	0.17	3.0	< 0.001	1.43
Distal level, mm^2	12	9.7	1.9	6.3	12.8	0.15			
Median nerve T2 relaxometry									
Proximal level, ms	12	64.7	7.4	55.2	76.6	0.11	5.1	0.034	0.70
Distal level, ms	12	59.6	7.8	48.1	71.6	0.12			

CTS: carpal tunnel syndrome; CSA: cross-sectional area; MRI: magnetic resonance imaging; SD: standard deviation.

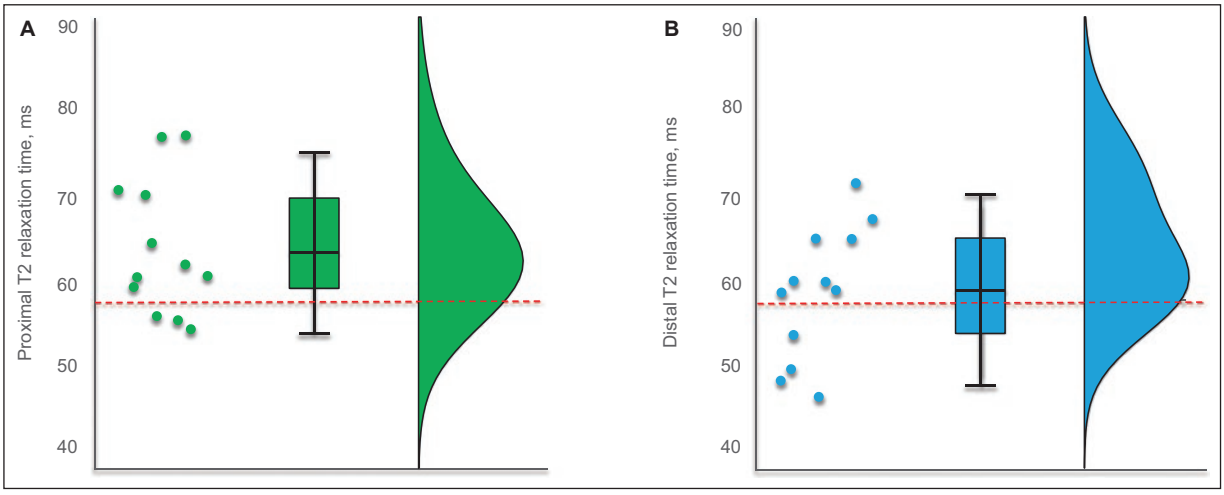

Figure 1. T2 relaxometry raincloud plot of the median nerve in patients with CTS. **A:** T2 relaxometry at the proximal carpal tunnel level. **B:** T2 relaxometry at the distal carpal tunnel level showing the scatter plot, box plot, and distribution curve. Values represent the variability of each individual measurement. The difference in means and the asymmetry of the distribution curve between levels are shown. The dotted line indicates the value reported in healthy Mexican patients[a] (58.8 ms). In CTS, both proximal and distal levels show increased T2 relaxometry values, with higher values at the proximal level of the carpal tunnel.

[a]Castro-Teran et al.[10] CTS: carpal tunnel syndrome; SD: standard deviation.

raincloud plot displaying the dispersion of T2 relaxometry values for each affected wrist, along with their representation in a box plot and distribution curve. The mean proximal T2 relaxometry value was 64.7 ± 7.4 ms (min 55.2, max 76.6). The mean T2 relaxometry at the distal level was 59.6 ± 7.8 ms (min 48.1, max 71.6).

Figure 2 shows wrist MRI and T2 relaxometry color map of a 52-year-old woman with pain, weakness, and nocturnal paresthesias of the left hand, with a clinical diagnosis of CTS. An increased CSA (10.8 mm^2, reference value 7 mm^2) was found at the proximal level compared with the distal level (6.3 mm^2, reference value 8 mm^2). T2 relaxometry time of the median nerve was higher at the proximal level (70.8 ms, reference value 58.8 ms) than at the distal level (59.2 ms). The imaging diagnosis was CTS. Figure 3 shows the right wrist MRI of the same patient as in figure 2, with a clinical diagnosis of bilateral CTS. Increased CSA (11.1 mm^2, reference value 7 mm^2) was found at the proximal level compared with the distal level (7.2 mm^2, reference value 8 mm^2). T2 relaxometry time of the median nerve was higher at the proximal level (76.64 ms, reference value 58.8 ms) than at the distal level (68.67 ms). The imaging diagnosis was CTS.

Figure 4 shows the wrist MRI of a 70-year-old woman with pain and nocturnal paresthesias. The proximal carpal tunnel showed increased CSA (11.6 mm^2, reference value 7 mm^2). Increased T2 relaxometry time (66.3 ms, reference value 58.8 ms) indicated intraneural edema. The imaging diagnosis was CTS. Quantitative findings showed variability, with increased CSA and T2 relaxometry values at the proximal level.

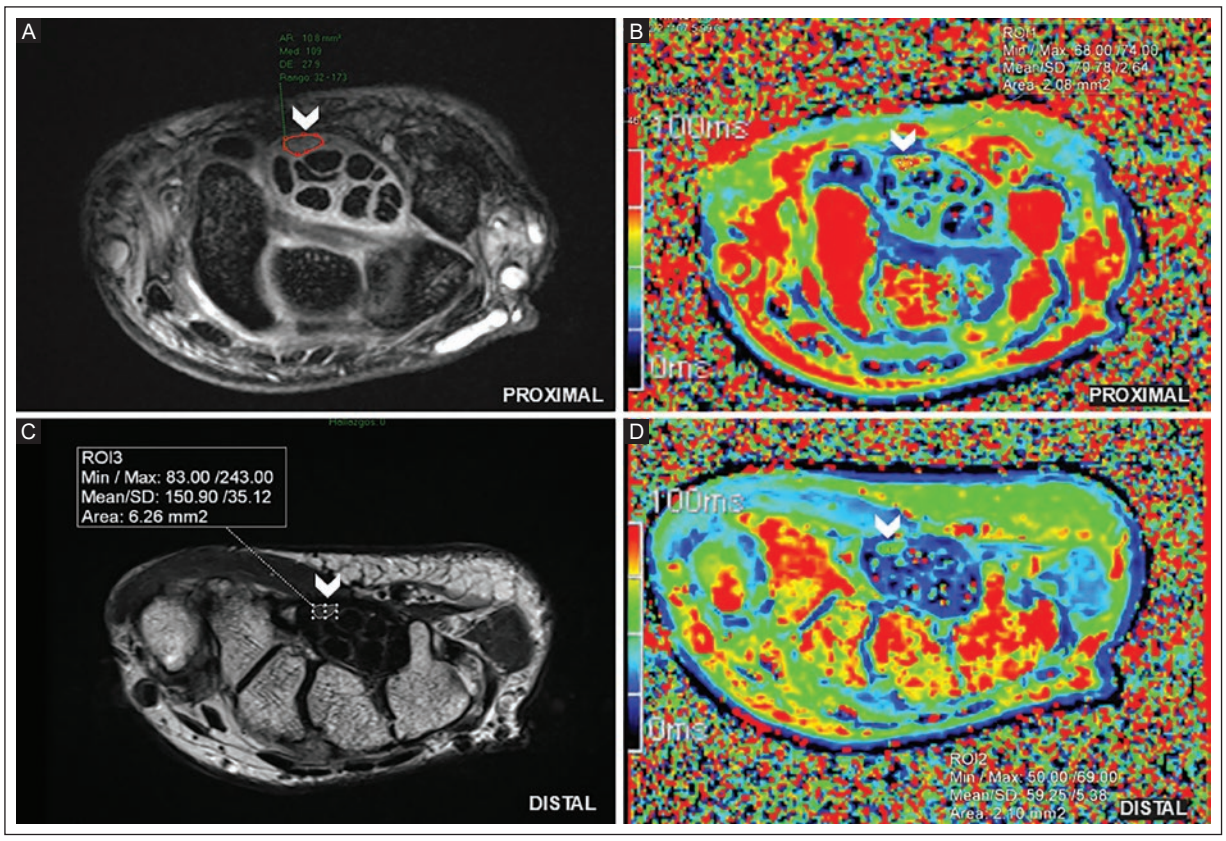

Figure 2. Wrist MRI of a 52-year-old woman with pain, weakness, and nocturnal paresthesia involving the left median nerve. The clinical diagnosis was CTS. **A:** T2 TSE axial view of the proximal carpal tunnel shows median nerve thickening with a CSA of 10.8 mm² (arrowhead) (reference value 7 mm²)[a]. **B:** T2 relaxometry of 70.8 ms (arrowhead) (reference value 58.8 ms)[b], consistent with intraneural edema. The imaging diagnosis was CTS. **C**: T2 TSE axial view at the distal carpal tunnel shows the median nerve with ovoid morphology. CSA measures 6.3 mm² (arrowhead) (reference value 8 mm²)[a]. **D**: T2 relaxometry map at the distal carpal tunnel shows a relaxation time of 59.2 ms (arrowhead), with no evidence of intraneural edema. [a]Middleton et al.[11], [b]Castro-Teran et al.[10]. CSA: cross-sectional area; CTS: carpal tunnel syndrome; MRI: magnetic resonance imaging; TSE: turbo spin echo.

Pearson correlation coefficients between median nerve CSA and T2 relaxometry and age, weight, height, and BMI in patients with CTS

No correlation was found between CSA and T2 relaxometry at the proximal and distal levels of the carpal tunnel of the median nerve, and age, weight, height, or BMI in patients with CTS (Table 3). Proximal and distal CSA measurements showed a moderate positive correlation (r = 0.47, p = 0.125), but this association was not significant. T2 relaxometry values at the proximal and distal levels showed a positive relationship: as the value at one level increased, the other also increased.

Correlation between BCTQ scales and median nerve CSA and T2 relaxometry in patients with CTS

There was no significant correlation between CSA and the BCTQ for symptom severity and functional status, with r = 0.16 and 0.19, respectively, at the proximal level and r = –0.04 and –0.19, respectively, at the distal level (p > 0.05) (Table 4). There was no significant correlation between T2 relaxometry values and the BCTQ for symptom severity and functional status, with r = 0.41 and 0.29, respectively, at the proximal level and r = –0.04 and –0.38, respectively, at the distal level (p > 0.05).

DISCUSSION

In our study of Mexican patients with CTS, MRI showed that the median nerve at the proximal carpal tunnel level had a larger CSA and a longer T2 relaxometry time than at the distal carpal tunnel level. The CSA and T2 relaxometry time at the proximal level were abnormally high compared with reference values for healthy individuals. Combining a morphological parameter, such as CSA, with a quantitative measurement, such as T2 relaxometry, may improve characterization of median nerve involvement in CTS. Our results show

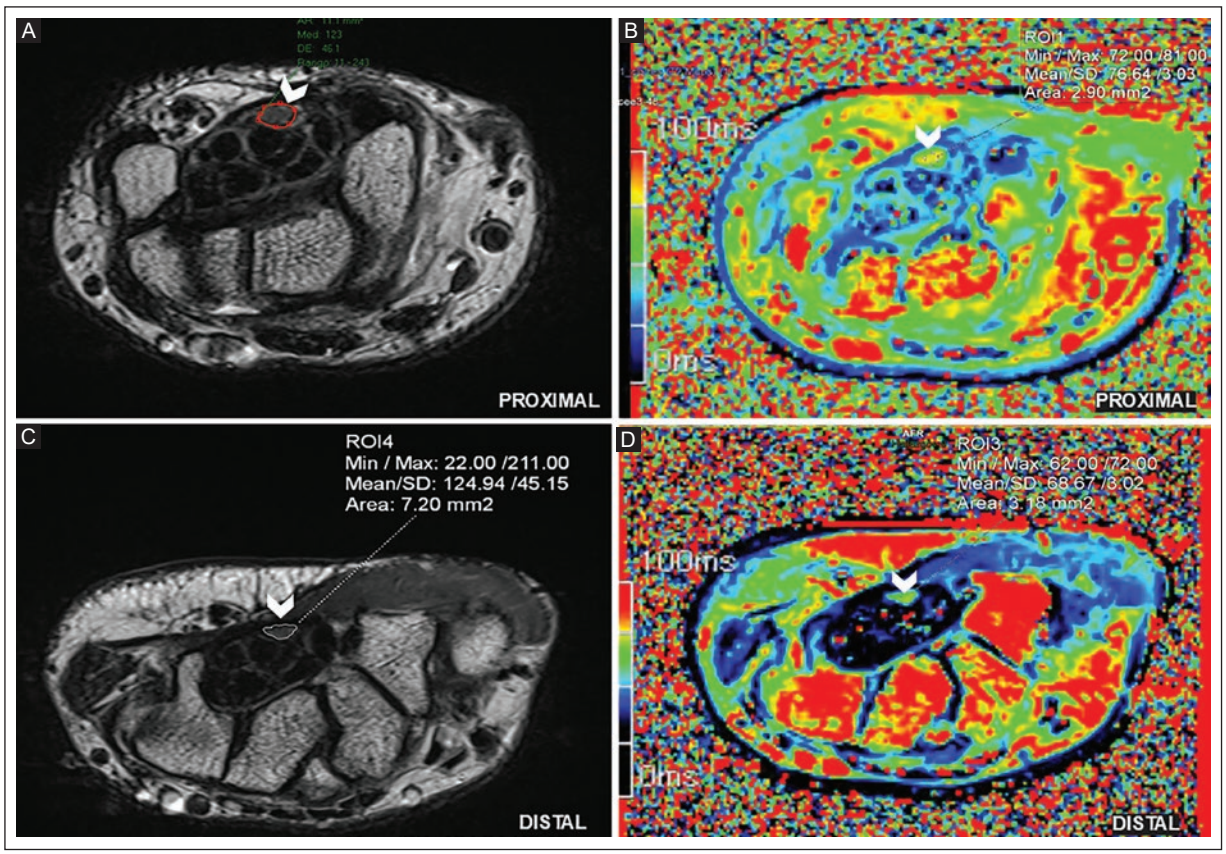

Figure 3. Right wrist MRI of the same patient as in Figure 2, with a clinical diagnosis of bilateral CTS. **A:** T2 TSE axial view at the proximal carpal tunnel level shows median nerve thickening with a CSA of 11.1 mm² (arrowhead) (reference value 7 mm²)[a]. **B:** T2 relaxometry map at the proximal carpal tunnel level shows the median nerve with an increased relaxation time of 76.6 ms (arrowhead) (reference value 58.8 ms)[b], suggestive of intraneural edema. **C:** T2 TSE axial view at the distal carpal tunnel level shows the median nerve with ovoid morphology. CSA measures 7.2 mm² (arrowhead) (reference value ≤ 8 mm²)[a]. **D:** T2 relaxometry map at the distal carpal tunnel level shows the median nerve with an increased relaxation time of 68.7 ms (arrowhead), consistent with intraneural edema. The imaging diagnosis was CTS.

[a]Middleton et al.[11], [b]Castro-Teran et al.[10]. CSA: cross-sectional area; CTS: carpal tunnel syndrome; MRI: magnetic resonance imaging; TSE: turbo spin echo.

Table 3. Pearson correlation coefficients between median nerve CSA and T2 relaxometry and age, weight, height, and BMI in patients with CTS

Description	Age	Weight	Height	BMI	Carpal tunnel		
					CSA		T2 relaxometry proximal level
					Proximal level	Distal level	
Median nerve CSA							
Proximal level	0.33	–0.23	–0.41	–0.12	-		
Distal level	0.07	–0.36	–0.38	–0.34	0.47	-	
Median nerve T2 relaxometry							
Proximal level	0.41	–0.21	–0.19	–0.16	0.10	–0.42	-
Distal level	0.21	–0.21	–0.29	–0.11	0.26	–0.36	0.57

BMI: body mass index; CTS: carpal tunnel syndrome; CSA: cross-sectional area.

that CSA and T2 relaxometry are sensitive biomarkers for local changes in the median nerve, especially at the proximal carpal tunnel level.

Both CSA and T2 relaxometry are typically increased in CTS compared with healthy subjects[4,5,15]. Cha et al.,[4] in a prospective study, compared CSA and T2 relaxometry at three anatomical carpal tunnel levels in 12 Korean CTS patients and 12 healthy controls using a 3.0T Signa HDxt MRI (GE Medical Systems, Milwaukee, WI, USA). CSA was 18.6 mm^2 in CTS versus 10.2 mm^2 in healthy controls ($p = 0.003$) at the proximal level. CSA was 12.0 mm^2 in CTS versus 9.6 mm^2 in healthy

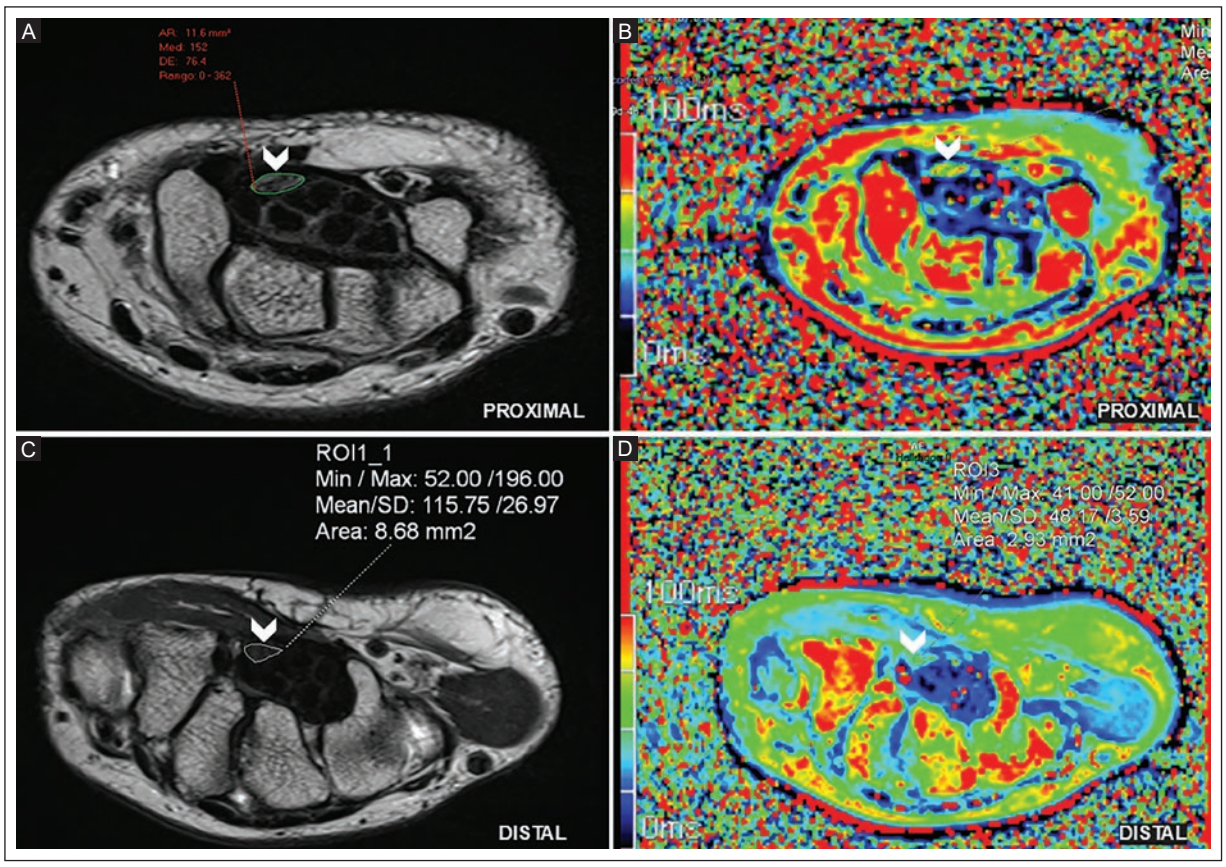

Figure 4. Wrist MRI of a 70-year-old woman with pain and nocturnal paresthesia. The clinical diagnosis was CTS. **A:** T2 TSE axial view at the proximal carpal tunnel level shows median nerve thickening with a CSA of 11.6 mm² (arrowhead) (reference value 7 mm²)[a]. **B:** T2 relaxometry map at the proximal carpal tunnel level shows an increased relaxation time of 66.3 ms (arrowhead) (reference value 58.8 ms)[b], suggestive of intraneural edema. The imaging diagnosis was CTS. **C:** T2 TSE axial view at the distal carpal tunnel level shows flattening and bulging of the median nerve under the flexor retinaculum (arrowhead). CSA is 8.7 mm² (reference value 8 mm²)[a]. **D:** T2 relaxometry map at the distal carpal tunnel level shows a relaxation time of 48.1 ms (arrowhead).

[a]Middleton et al.[11], [b]Castro-Teran et al.[10]. CSA: cross-sectional area; CTS: carpal tunnel syndrome; MRI: magnetic resonance imaging; TSE: turbo spin echo.

Table 4. Correlation between BCTQ scales[a] and median nerve CSA and T2 relaxometry in patients with CTS

Description	Parameter	Carpal tunnel			
		Proximal level		Distal level	
		CSA	T2 relaxometry	CSA	T2 relaxometry
Symptom Severity Scale	r	0.16	0.41	–0.04	–0.04
Functional Status Scale	r	0.19	0.29	–0.19	–0.38

[a]BCTQ: Boston Carpal Tunnel Questionnaire[12]. CTS: carpal tunnel syndrome; CSA: cross-sectional area.

controls (p = 0.10) at the distal tunnel. CSA was 14.9 mm² in CTS versus 10.5 mm² in healthy controls (p = 0.002) at the distal radioulnar joint. Median nerve T2 relaxometry at the proximal level was 52.1 ms in CTS versus 44.3 ms in healthy controls (p = 0.03), and 51.0 ms in CTS versus 41.8 ms in healthy controls (p = 0.03) at the distal level. At the distal radioulnar joint, it was 44.4 ms in CTS versus 44.0 ms in healthy controls (p = 0.84). The increased CSA and T2 relaxometry were mainly at nerve compression sites (proximal and distal) in the carpal tunnel. Maeda et al.[5] found a significant increase in median nerve T2 relaxometry in the proximal carpal tunnel (56.7 ± 16.4 ms) compared to the control group (51.2 ± 10.8 ms) (p = 0.02) in 71 Japanese patients with CTS and 26 healthy controls using a 3.0T Trillium Oval scanner (Hitachi Ltd, Tokyo, Japan). There was no significant difference at the distal level (p = 0.64), with values of 51.0 ± 17.3 ms in CTS patients and 49.4 ± 8.5 ms in healthy controls. The authors concluded that T2 relaxometry values in CTS patients were higher in the proximal carpal tunnel than in healthy controls, with no significant difference at the

distal level. Castro-Teran et al.,[10] in a cross-sectional study of 30 healthy Mexican individuals using a 3.0T Magnetom Skyra Fit (Siemens Healthineers, Erlangen, Germany), reported a mean T2 relaxometry time of 58.8 ± 9.0 ms at the proximal carpal tunnel level. In our study of Mexican patients with CTS, we found significantly increased T2 relaxometry times (64.7 ms) in the proximal carpal tunnel compared with those previously reported in healthy Mexican subjects (58.8 ms). The differences observed between our results and those of Cha et al.[4] and Maeda et al.[5] may, in part, be due to the use of different scanners and population characteristics[15]. There are currently no reference standard values for CSA and T2 relaxometry in CTS. This may reflect several technical and biological factors across populations. In CTS, the median nerve shows region-dependent alterations within the carpal tunnel, characterized by increased T2 MRI signal and nerve enlargement, predominantly at the proximal level. This pattern is attributed to the pathophysiology of compressive neuropathy, in which mechanical compression at the distal tunnel leads to impaired venous return, intraneural edema, and retrograde fluid accumulation, which cause pronounced changes proximally[5,8,15-17].

CSA may be affected by factors such as weight, height, and BMI[6]. In contrast, T2 relaxometry appears to be a more specific biomarker of neural microstructural damage, as it reflects intrinsic tissue alterations, such as intraneural edema and changes in water content. It is also less influenced by anthropometric variability[18]. Bowers et al.[19] evaluated the relationship between the median nerve CSA and BMI in a prospective study of 24 American patients with CTS and 283 patients without CTS using 1.5T or 3.0T MRI. They found that higher BMI was associated with higher CSA, with significant differences at both proximal and distal levels ($p = 0.01$). Patients with CTS had significantly higher CSA, and high BMI was associated with increased median nerve size, even without CTS. The correlation between T2 relaxation time and age has not been clearly defined. Kronlage et al.,[8] in a study of 60 healthy German subjects evaluated with 3.0T MRI, assessed T2 relaxation of the median, ulnar, and sciatic nerves and found correlations with height ($r = 0.28$), weight ($r = 0.40$), and BMI ($r = 0.35$), but not with age ($r = 0.23$). Castro-Teran et al.,[10] in healthy Mexican individuals, found a weak positive correlation indicating that median nerve T2 relaxation increased with age. However, insufficient data exist to establish a definitive correlation between age and T2 relaxation time. We did not find a correlation between anthropometric variables (age, weight, height, and BMI) and CSA or T2 relaxometry values in patients with CTS. These findings suggest that in our sample of Mexican patients with CTS, both CSA and T2 relaxometry are independent of patient anthropometric characteristics, reinforcing the concept that the primary effect is due to local nerve alterations rather than systemic influences.

The relationship between morphological parameters, such as CSA, and quantitative measurements, such as T2 relaxometry, and symptoms and functional status in patients with CTS has been rarely evaluated. Samanci et al.[20] reported a study of 23 Turkish patients with CTS and abnormal nerve conduction studies. The control group consisted of 24 healthy individuals matched for age, sex, and BMI. Symptoms and functional scores were assessed using the BCTQ. The preoperative BCTQ values were 3.6 ± 0.8 for the SSS and 3.3 ± 0.94 for the FSS, based on the average of all responses weighed to 5, whereas the postoperative values were 1.9 ± 0.6 for both SSS and FSS. In our study, the mean SSS value was 2.2 ± 0.5, indicating moderate symptom severity. The mean FSS value was 1.7 ± 0.8, suggesting mild functional impairment. No correlation was found between CSA or T2 relaxometry and the clinical scales (SSS and FSS). The lack of correlation between quantitative MRI findings and clinical scales in CTS may be due to several factors, such as the timing of diagnosis relative to imaging assessment.

The strengths of this study include the use of quantitative 3.0T MRI parameters and a standardized acquisition and analysis protocol, enabling reproducible assessment of the median nerve at two carpal tunnel levels in patients with CTS. However, there are several limitations, particularly the case-series design without a healthy control group, which limits the generalizability of the findings. Additionally, electromyographic diagnosis of CTS was not available.

CONCLUSION

In patients with CTS, the median nerve shows significantly higher CSA and T2 relaxometry at the proximal carpal tunnel level than at the distal level. CSA and T2 relaxometry are complementary MRI biomarkers that assess median nerve damage. These measurements provide objective information on microstructural changes in the nerve, regardless of clinical severity or function. Further studies should include larger sample sizes, a healthy control group, and correlations with electrodiagnostic studies to validate this diagnostic approach in clinical practice.

Acknowledgments

The authors thank Professor Ana M. Contreras-Navarro for her guidance in preparing and writing this scientific paper. This original research in the Radiology Specialty field was an awarded thesis at the *Cuarta Convocatoria Nacional 2025-2026 "Las Mejores Tesis para Publicar en el JMeXFRI"*.

Funding

The authors declare that they have not received funding.

Conflicts of interest

The authors declare no conflicts of interest.

Ethical considerations

Protection of human subjects and animals. The authors declare that the procedures followed were in accordance with the ethical standards of the responsible committee on human experimentation and with the World Medical Association and the Declaration of Helsinki (1964) and subsequent amendments.

Confidentiality, informed consent, and ethical approval. The authors have followed their institution's confidentiality protocols, obtained informed consent from all patients, and secured approval from the Ethics Committee.SAGER guidelines have been followed as applicable to the nature of the study.

Declaration on the use of artificial intelligence. The authors declare that no generative artificial intelligence was used in the writing or creation of the content of this manuscript.

REFERENCES

1. Huang YT, Chen CJ, Wang YW, Horng YS. Comparing the carpal tunnel area and carpal boundaries in patients with carpal tunnel syndrome and healthy volunteers: a magnetic resonance imaging study. Diagnostics (Basel). 2025;15(10):1205. doi: 10.3390/diagnostics15101205.
2. Park JS, Won HC, Oh JY, Kim DH, Hwang SC, Yoo JI. Value of cross-sectional area of median nerve by MRI in carpal tunnel syndrome. Asian J Surg. 2020;43(6):654-659. doi: 10.1016/j.asjsur.2019.08.001.
3. Kumari A, Singh S, Garg A, Prakash A, Sural S. Tingling hand: magnetic resonance imaging of median nerve pathologies within the carpal tunnel. Pol J Radiol. 2019;84:e484-e490. doi:10.5114/pjr.2019.90354.
4. Cha JG, Han JK, Im SB, Kang SJ. Median nerve T2 assessment in the wrist joints: preliminary study in patients with carpal tunnel syndrome and healthy volunteers. J Magn Reson Imaging. 2014;40(4):789-795. doi:10.1002/jmri.24448.
5. Maeda A, Suzuki T, Hayakawa K, Funahashi T, Kuroiwa T, Fujita N. T2 mapping of the median nerve in patients with carpal tunnel syndrome and healthy volunteers. Muscle Nerve. 2021;63(5):774-777. doi:10.1002/mus.27205.
6. Warburton C, Cabrera C, Pérez O, Capelle J, Dodds SD, Jose J. Identifying anatomic landmarks and median nerve characteristics for the analysis of persistent carpal tunnel syndrome using magnetic resonance imaging (MRI). Skeletal Radiol. 2024;53(2):299-305. doi: 10.1007/s00256-023-04397-2.
7. Naik S, Mahanty S, Bhoi SK, Lahre Y, Bag ND, Mohakud S. MRI of wrist and diffusion tensor imaging of the median nerve in patients with carpal tunnel syndrome. J Neurosci Rural Pract. 2023;14(2):302-307. doi: 10.25259/jnrp_57_2022.
8. Kronlage M, Schwehr V, Schwarz D, Godel T, Heiland S, Bendszus M, et al. Magnetic resonance neurography: normal values and demographic determinants of nerve caliber and T2 relaxometry in 60 healthy individuals. Clin Neuroradiol. 2019;29(1):19-26. doi: 10.1007/s00062-017-0633-5.
9. Hayakawa K, Suzuki T, Hayakawa K, Kawano Y, Iwamoto T, Fujita N. Three-dimensional magnetic resonance imaging of median nerve volume for assessing carpal tunnel syndrome severity. Muscle Nerve. 2025;72(5):1117-1121. doi:10.1002/mus.70010.
10. Castro-Teran C, Elias-Perez B, Hernandez-Medina A. Normal T2 relaxometry values of peripheral nerves on 3.0T MRI in healthy Mexican subjects: an exploratory study. J Mex Fed Radiol Imaging. 2025;4(2):125-130. doi:10.24875/jmri.M25000105.
11. Middleton WD, Kneeland JB, Kellman GM, Cates JD, Sanger JR, Jesmanowicz A, et al. MR imaging of the carpal tunnel: normal anatomy and preliminary findings in the carpal tunnel syndrome. AJR Am J Roentgenol. 1987;148(2):307-316. doi: 10.2214/ajr.148.2.307.
12. Leite JC, Jerosch-Herold C, Song F. A systematic review of the psychometric properties of the Boston Carpal Tunnel Questionnaire. BMC Musculoskelet Disord. 2006;7:78. doi: 10.1186/1471-2474-7-78.
13. Sawilowsky SS. New effect size rules of thumb. J Mod Appl Stat Methods. 2009;8(2):597-599. doi:10.22237/jmasm/1257035100.
14. Friedrichsmeier T. the RKWard Team (2024). RKWard: Graphical interface to the statistical language R. Version 0.8.0. https://rkward.kde.org.
15. Kollmer J, Bendszus M. Magnetic resonance neurography: improved diagnosis of peripheral neuropathies. Neurotherapeutics. 2021;18(4):2368-2383. doi:10.1007/s13311-021-01166-8.
16. Kondo H, Suzuki T, Hayakawa K, Maeda A, Funahashi T, Kuroiwa T, et al. T2 magnetic resonance imaging mapping and morphology of the median nerve before and after surgery in carpal tunnel syndrome. Muscle Nerve. 2024;70(3):346-351. doi:10.1002/mus.28191.
17. Sunderland S. The nerve lesion in the carpal tunnel syndrome. J Neurol Neurosurg Psychiatry. 1976;39(7):615-626. doi:10.1136/jnnp.39.7.615.
18. Gambarota G. T2 relaxometry of human median nerve. Semin Musculoskelet Radiol. 2009;13(1):24-28. doi: 10.1055/s-0029-1202242.
19. Bowers EMR, Como CJ, Dooley SW, Morales-Restrepo A, Fowler JR. Magnetic resonance imaging-measured cross-sectional area of the median nerve. J Hand Surg Glob Online. 2022;4(2):93-96. doi:10.1016/j.jhsg.2021.11.003.
20. Samanci Y, Karagöz Y, Yaman M, Atçı İB, Emre U, Kılıçkesmez NÖ, et al. Evaluation of median nerve T2 signal changes in patients with surgically treated carpal tunnel syndrome. Clin Neurol Neurosurg. 2016;150:152-158. doi:10.1016/j.clineuro.2016.09.011.

JMeXFRI

Journal of the Mexican Federation of Radiology and Imaging

Check for updates

FULL RESEARCH ARTICLE

CTA plaque characteristics of non-stenotic carotid arteries in Mexican patients with ipsilateral embolic stroke of undetermined source and in patients with other neurological diagnoses

Christian E. Sanchez-Sanchez[1,2], Vanessa Cano-Nigenda[3], Roger A. Carrillo-Mezo[1], Kevin Enriquez-Peregrino[4], Rebeca de J. Ramos-Sanchez[1], Ana L. Calderon-Garcidueñas[5] and Antonio Arauz-Gongora[2]*

[1]Department of Neuroimaging, Instituto Nacional de Neurologia y Neurocirugia "Manuel Velasco Suarez", Secretaria de Salud, Mexico City; [2]Cadem Artista, Chopo Laboratories, Proa Medical Diagnostic Group, San Luis Potosi, S.L.P.; [3]Stroke Clinic; [4]Department of Emergency; [5]Department of Neuropathology. Instituto Nacional de Neurologia y Neurocirugia "Manuel Velasco Suarez", Secretaria de Salud, Mexico City. Mexico

ABSTRACT

Introduction: *Non-stenotic carotid plaque is associated with embolic stroke of undetermined source (ESUS). This study characterizes the morphology of non-stenotic carotid plaque using head and neck CTA in Mexican patients with ipsilateral ESUS and in patients without ESUS but with other neurological diagnoses.* **Material and methods:** *This cross-sectional study was conducted in patients with non-stenotic carotid plaque (< 50%). Only unilateral evaluation of the carotid artery was reported using head and neck CTA. Patients with non-stenotic carotid plaque were classified into two groups: those with ipsilateral ESUS and those without ESUS but with other neurological diagnoses. The characteristics of non-stenotic carotid plaque considered high-risk for ischemic stroke, and those not considered high-risk, a history of ipsilateral ischemic stroke, and a transient ischemic attack (TIA) were recorded.* **Results:** *We included 410 patients with non-stenotic carotid plaque assessed by head and neck CTA: 175 (42.7%) with ipsilateral ESUS and 235 (57.3%) without ESUS but with other neurological diagnoses, including aneurysm, intracranial hemorrhage, demyelinating disease, or epilepsy. In the ipsilateral ESUS group, the most frequent high-risk characteristics of non-stenotic carotid plaque were irregular surface (n = 168, 96.0%) and ulceration (n = 102, 58.3%), whereas punctate calcifications (n = 131, 74.8%) and plaque length ≥ 10 mm (n = 111, 63.4%) were not considered high-risk. In the group without ESUS, an irregular surface was observed in 218 (92.8%) and ulceration in 131 (55.7%); punctate calcifications, identified in 164 (69.8%), and plaque length ≥ 10 mm in 159 (67.6%), were not considered high-risk. None of the morphological characteristics of non-stenotic carotid plaque showed a significant association with ipsilateral ESUS.* **Conclusion:** *In Mexican patients with ipsilateral ESUS, high-risk morphological characteristics of non-stenotic carotid plaque on head and neck CTA included an irregular surface, ulceration, a lipid-rich necrotic core, and intraplaque hemorrhage. Comparable results were found in patients without ESUS but with other neurological diagnoses.*

Keywords: *Embolic stroke. Computed tomography angiography. Embolic stroke of undetermined source. Non-stenotic carotid plaque. High-risk carotid plaque.*

***Corresponding author:**
Vanessa Cano-Nigenda
E-mail: vcanonigenda@gmail.com

Received for publication: 21-11-2025
Accepted for publication: 06-02-2026
DOI: 10.24875/JMEXFRI.M26000128

Available online: 08-07-2026
J Mex Fed Radiol Imaging. 2026;5(2):116-125
www.JMeXFRI.com

INTRODUCTION

Ischemic stroke is a leading cause of morbidity and mortality worldwide, but in approximately 30% of cases, the etiology remains undetermined and is termed cryptogenic stroke[1], which is classified into three subgroups[2]: stroke with no identifiable cause after a complete diagnostic evaluation; stroke with multiple possible underlying causes; and stroke with an incomplete diagnostic evaluation. Within the subgroup with a complete diagnostic evaluation, the term embolic stroke of undetermined source (ESUS) defines a specific group of patients with non-lacunar cerebral infarction, non-stenotic carotid plaque (< 50%), and no major identifiable cardioembolic source. ESUS represents approximately 15%-20% of all ischemic strokes and is a clinically relevant entity due to its heterogeneous etiology and an annual recurrence risk of 4% to 5%[1].

Non-stenotic carotid plaque (< 50%) has traditionally been considered low risk for ischemic stroke[3,4]. However, recent evidence suggests that high-risk plaque features such as an irregular surface, ulceration, a lipid-rich necrotic core, or intraplaque hemorrhage may cause embolism[5]. Other features, such as punctate calcifications[6] and plaque length ≥ 10 mm[7] have been considered non-high risk. Various imaging modalities have been used to evaluate the morphological characteristics of non-stenotic carotid plaque, including color Doppler ultrasound[8], head and neck computed tomography angiography (CTA)[5], magnetic resonance imaging (MRI)[9], and positron emission tomography-computed tomography (PET-CT)[10].

In patients with ESUS, the prevalence of non-stenotic carotid plaque has been reported to range from 39.1%[11] to 42.1%[12], and it occurs more frequently on the ipsilateral than the contralateral side. High-risk characteristics of non-stenotic carotid plaque (< 50%) have been identified by head and neck CTA[5]. The prevalence of morphological characteristics of non-stenotic carotid plaque on head and neck CTA in patients with ipsilateral ESUS is heterogeneous worldwide; however, information on Latin American populations is scarce[11]. This study describes the morphological characteristics of non-stenotic carotid plaque on head and neck CTA in Mexican patients with ipsilateral ESUS and in those without ESUS but with other neurological diagnoses.

MATERIAL AND METHODS

This retrospective cross-sectional study was conducted from March 2024 to February 2025 in the Department of Neuroimaging at the Instituto Nacional de Neurologia y Neurocirugia Manuel Velasco Suarez, in Mexico City, Mexico. Consecutive adults (≥ 18 years) with acute neurological symptoms and non-stenotic carotid plaque identified on head and neck CTA were included. Patients with non-stenotic plaques were excluded if they had an ischemic stroke of determined etiology according to TOAST criteria[13], a carotid stenosis ≥ 50%, complete carotid occlusion, carotid dissection, or scans with incomplete acquisition or an inadequate arterial phase. Informed consent was waived due to the study's retrospective design and the use of data obtained during routine clinical care. The study was approved by the Institutional Research and Ethics Committees.

Study development and variables

Clinical and imaging records were analyzed, and the following variables were collected: age, sex, smoking history, transient ischemic attack (TIA), systemic arterial hypertension, type 2 diabetes, family history of stroke in a first-degree relative, and a previous ipsilateral ischemic stroke documented by computed tomography (CT) on admission.

The morphological characteristics of high-risk non-stenotic carotid plaque, including an irregular surface, ulceration, lipid-rich necrotic core, and intraplaque hemorrhage, were recorded. Features not considered high-risk for ischemic stroke, such as punctate calcifications and plaque length ≥ 10 mm, were also recorded.

Two groups were defined: patients with ipsilateral ESUS, including those with non-stenotic carotid plaque (< 50%) in whom other etiologies were excluded according to TOAST[13], and patients without ESUS but with other neurological diagnoses (aneurysm, intracranial hemorrhage, demyelinating disease, or epilepsy) who had no imaging evidence of ischemic stroke, and a non-stenotic carotid plaque as an incidental finding. In patients with ESUS, only the carotid artery on the same side as the ischemic event was evaluated. In patients without ESUS, but with other neurological diagnoses, a unilateral carotid artery with a non-stenotic plaque and greater atherosclerotic burden was assessed.

Definitions[14]

Irregular surface: plaque contour variability exceeding 1 mm in depth.

Ulceration: contrast extension ≥ 1 mm projecting beyond the luminal boundary into the plaque.

Lipid-rich necrotic core: a plaque component with attenuation less than 30 Hounsfield units (HU).

Intraplaque hemorrhage: subadventitial or intraplaque hyperdensity associated with adjacent fat stranding.

Punctate calcifications: hyperdense foci within the plaque > 130 HU.

Plaque length: the maximum longitudinal extent measured (mm) on multiplanar head and neck CTA reconstructions.

Image acquisition protocol

Head and neck CTA examinations were performed on a 128-slice CT scanner (Somatom Definition AS+, Siemens Healthcare, Forchheim, Germany). Automatic exposure control (CARE Dose 4D) was used with a reference tube current of 90 mAs. Tube voltage was selected based on scout acquisition (CARE kV). A total of 50 mL of non-ionic iodinated contrast medium (Iomeprol 300 mg/mL, Lomeron® 300; Bracco Imaging, Milan, Italy) was administered at 5 mL/s via a power injector (EmpowerCTA+, ACIST Medical Systems, Eden Prairie, MN, USA), followed by a 30-mL saline flush. Scanning was performed in the caudocranial direction with a pitch of 1.4 and a rotation time of 0.33 s at 120 kV. Images were reconstructed using the sinogram-affirmed iterative reconstruction (SAFIRE; Siemens Healthcare, Forchheim, Germany) algorithm with a strength level of 3. Bolus tracking was performed using a region of interest (ROI) positioned in the aortic arch; acquisition was automatically triggered when attenuation reached 70 HU.

Statistical analysis

Quantitative variables tested for normality with the Shapiro-Wilk test were reported as means ± standard deviation or as medians with interquartile ranges, as appropriate. Qualitative variables were reported as absolute and relative frequencies. Comparative analyses assessed differences in carotid plaque morphological characteristics between patients with and without ESUS using Student's *t*-test or the Mann-Whitney U test for continuous variables and the chi-square test or Fisher's exact test for categorical variables. A p value < 0.05 was considered statistically significant. Statistical analyses were performed using SPSS Statistics version 26.0 (IBM Corp., Armonk, NY, USA).

RESULTS

Four hundred ten patients with a non-stenotic carotid plaque (< 50%) were included; 175 (42.7%) in the ipsilateral ESUS group and 235 (57.3%) in the group without ESUS but with other neurological diagnoses (Table 1). Age was significantly higher in patients with ipsilateral ESUS (68.7 ± 13.0 vs 64.4 ± 13.0 years; p < 0.001). The groups were comparable by sex (n = 206, 50.3% vs n = 204, 49.7%) and smoking status (n = 80, 45.7% vs n = 104, 44.2%; p = 0.836).

A history of ipsilateral ischemic stroke was more common in patients with ipsilateral ESUS than in the non-ESUS group (n = 140, 80.0% vs n = 4, 1.7%; p < 0.001). Similarly, TIA (n = 56**,** 32.0% vs n = 38, 16.2%; p < 0.001), systemic arterial hypertension (n = 127, 72.6% vs n = 125, 53.2%; p < 0.001), and type 2 diabetes (n = 78, 44.6% vs n = 76, 32.3%; p < 0.05) were significantly associated with ipsilateral ESUS.

Morphological characteristics of non-stenotic carotid plaque

In patients with non-stenotic carotid plaque and ipsilateral ESUS, the most frequent high-risk characteristics were an irregular surface (n = 168, 96.0%), followed by plaque ulceration (n = 102, 58.3%) (Table 2). Among the morphological characteristics not considered high-risk, punctate calcifications were present in 131 (74.8%) patients, followed by plaque length ≥ 10 mm (n = 111, 63.4%). Two or more morphological characteristics of non-stenotic carotid plaque were present in most patients.

In the group without ESUS but with other neurological diagnoses and non-stenotic carotid plaque, the most frequent high-risk characteristic was an irregular surface (n = 218, 92.8%), followed by plaque ulceration (n = 131, 55.7%). Among morphological characteristics not considered high-risk, punctate calcifications were present in 164 (69.8%) patients, followed by plaque length ≥ 10 mm (n = 159, 67.6%). Two or more morphological characteristics of non-stenotic carotid plaque were observed in most patients.

Morphological characteristics of non-stenotic carotid plaques evaluated by head and neck CTA are shown in figure 1. A head and neck CTA scan of a non-stenotic carotid plaque with high-risk morphological characteristics associated with ipsilateral ESUS is shown in figure 2. Additionally, figures 3 and 4 show high-risk morphological characteristics and other features not considered high risk in non-stenotic carotid plaque in patients without ESUS but with other neurological diagnoses, such as intracranial aneurysm and epilepsy.

Table 1. Characteristics of patients with non-stenotic[a] carotid plaque with ipsilateral ESUS compared with patients without ESUS, but with other neurological diagnoses[b] assessed with head and neck CTA

Description	Total (n = 410)	Ipsilateral ESUS group (n = 175)	Other neurological diagnoses group (n = 235)	p
Age, years, mean ± SD	66.2 ± 12.6	68.7 ± 13.0	64.4 ± 13.0	< 0.001
Sex, n (%)				
Women	206 (50.3)	89 (50.8)	117 (49.8)	0.901
Men	204 (49.7)	86 (49.1)	118 (50.2)	0.901
Smoking, n (%)	184 (44.9)	80 (45.7)	104 (44.2)	0.836
Family history of stroke in first-degree relatives, n (%)	18 (4.4)	12 (6.8)	6 (2.5)	0.068
Previous ipsilateral ischemic stroke[c], n (%)	144 (35.1)	140 (80.0)	4 (1.7)	< 0.001
Presence of TIA[d], n (%)	94 (22.9)	56 (32.0)	38 (16.2)	< 0.001
Comorbidities				
Systemic arterial hypertension, n (%)	252 (61.5)	127 (72.6)	125 (53.2)	< 0.001
Type 2 diabetes, n (%)	154 (37.6)	78 (44.6)	76 (32.3)	< 0.05

[a]Stenosis less than 50% of the arterial lumen. [b]Patients with non-stenotic carotid plaque and no imaging evidence of ESUS, but with other neurological diagnoses such as aneurysm, intracranial hemorrhage, demyelinating disease, or epilepsy. [c]Non-recent ipsilateral ischemic stroke, documented by CT scan on admission. [d]Clinical history of TIA before the current event. CTA: computed tomography angiography; ESUS: embolic stroke of undetermined source; SD: standard deviation; TIA: transient ischemic attack.

Table 2. Morphological characteristics of non-stenotic carotid plaque[a] in patients with ipsilateral ESUS compared with patients without ESUS, but with other neurological diagnoses[b] assessed with head and neck CTA

Description	Total[c] (n = 410)	Ipsilateral ESUS group (n = 175)	Other neurological diagnoses group[c] (n = 235)
High-risk morphological characteristics of non-stenotic carotid plaque			
Irregular surface, n (%)	386 (94.1)	168 (96.0)	218 (92.8)
Ulceration, n (%)	233 (56.8)	102 (58.3)	131 (55.7)
Lipid-rich necrotic core, n (%)	54 (13.2)	20 (11.4)	34 (14.5)
Intraplaque hemorrhage, n (%)	2 (0.5)	1 (0.6)	1 (0.4)
Not considered high-risk morphological characteristics of non-stenotic carotid plaque			
Punctate calcifications, n (%)	295 (71.9)	131 (74.8)	164 (69.8)
Plaque length ≥ 10 mm, n (%)	270 (65.8)	111 (63.4)	159 (67.6)

[a]Stenosis < 50% of the carotid arterial lumen. [b]Patients with a non-stenotic carotid plaque and no imaging evidence of ESUS, but with other neurological diagnoses such as aneurysm, intracranial hemorrhage, demyelinating disease, or epilepsy. [c]Two or more morphological characteristics of non-stenotic carotid plaque were found in patients. CTA: computed tomography angiography; ESUS: embolic stroke of undetermined source.

DISCUSSION

In this study, head and neck CTA identified an irregular surface, ulceration, a lipid-rich necrotic core, and intraplaque hemorrhage as high-risk morphological characteristics of non-stenotic carotid plaque in Mexican patients with ipsilateral ESUS. Additionally, features not considered high-risk, such as punctate calcifications and plaque length ≥ 10 mm, were also commonly observed. Similar findings were observed in patients without ESUS but with other neurological diagnoses. This study is the first to describe the morphological characteristics of non-stenotic carotid plaque in Mexican patients with ipsilateral ESUS.

Non-stenotic carotid plaques can exhibit morphological features associated with instability, regardless of the degree of luminal stenosis. These features include an irregular surface, ulceration, a lipid-rich necrotic core, and intraplaque hemorrhage, which have been defined as high-risk markers of plaque vulnerability[11,15,16]. Demir et al.[17] in a retrospective cross-sectional study using head and neck CTA evaluated 81 Turkish patients

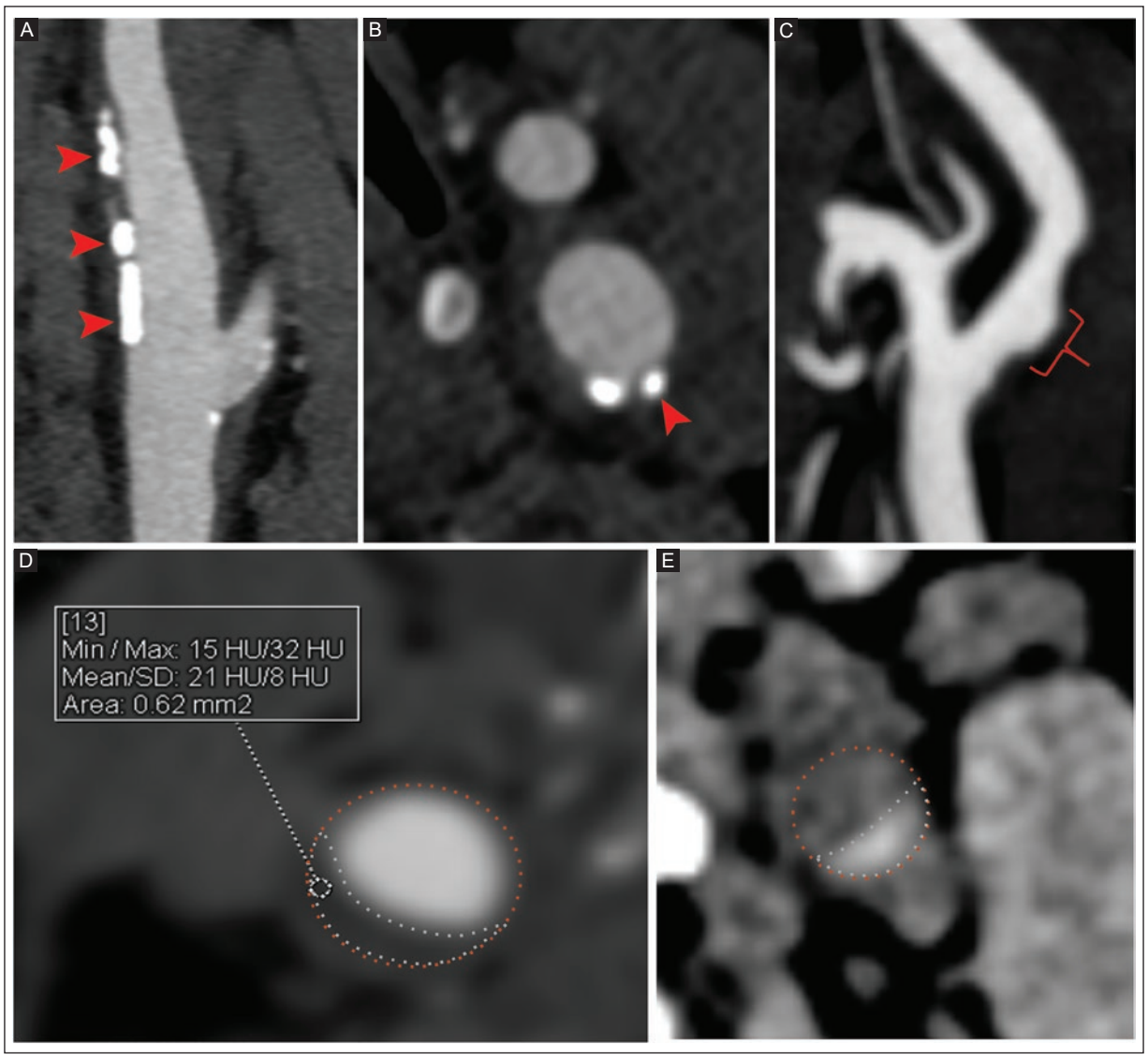

Figure 1. Morphological characteristics of non-stenotic carotid plaques by head and neck CTA. **A:** arterial phase oblique sagittal reconstruction MIP and vascular filter in the carotid bulb showing an irregular plaque surface (red arrowheads). **B:** arterial phase axial view of the carotid bulb showing subendothelial punctate calcifications (red arrowhead). **C:** arterial phase of the carotid bulb with oblique sagittal MIP reconstruction showing contrast extending > 1 mm beyond the luminal contour, indicating plaque ulceration (red curly bracket). **D:** arterial phase MIP of the carotid bulb, axial view. The orange dotted line marks the arterial contour, and the white dotted line marks the hypodense plaque contour, with attenuation of 21 ± 8 HU, suggesting a lipid-rich necrotic core. **E:** unenhanced-phase axial view of the carotid artery. The orange dotted line marks the arterial contour. The hyperdense intraplaque area, indicated by white dotted lines, suggests intraplaque hemorrhage.

CTA: computed tomography angiography; HU: Hounsfield units; MIP: maximum intensity projection.

with ESUS. Non-stenotic carotid plaques were more frequent in the ipsilateral carotid artery than on the contralateral side (44/81, 54.3% vs 24/81, 29.6%; p = 0.002). Plaque thickness ≥ 3 mm (28/81, 34.6% vs 11/81, 13.6%; p = 0.003), plaque ulceration (24/81, 29.6% vs 7/81, 8.6%; p = 0.001), plaque irregularity (34/81, 42.0% vs 10/81, 12.3%; p < 0.001), noncalcified plaque (21/81, 26.0% vs 5/81, 6.2%; p = 0.001), and plaque hypodensity (20/81, 24.7% vs 5/81, 6.2%; p = 0.002) were significantly more frequent in the carotid artery on the same side as the ischemic event. The authors concluded that non-stenotic carotid plaques, particularly those with high-risk characteristics, are more prevalent on the ipsilateral side and should be considered in the clinical evaluation and treatment of ESUS. In a meta-analysis that included 10 studies with a predominance of patients with ESUS (n = 797), the prevalence of non-stenotic carotid plaques was 55% (95% CI: 42-68)[11].

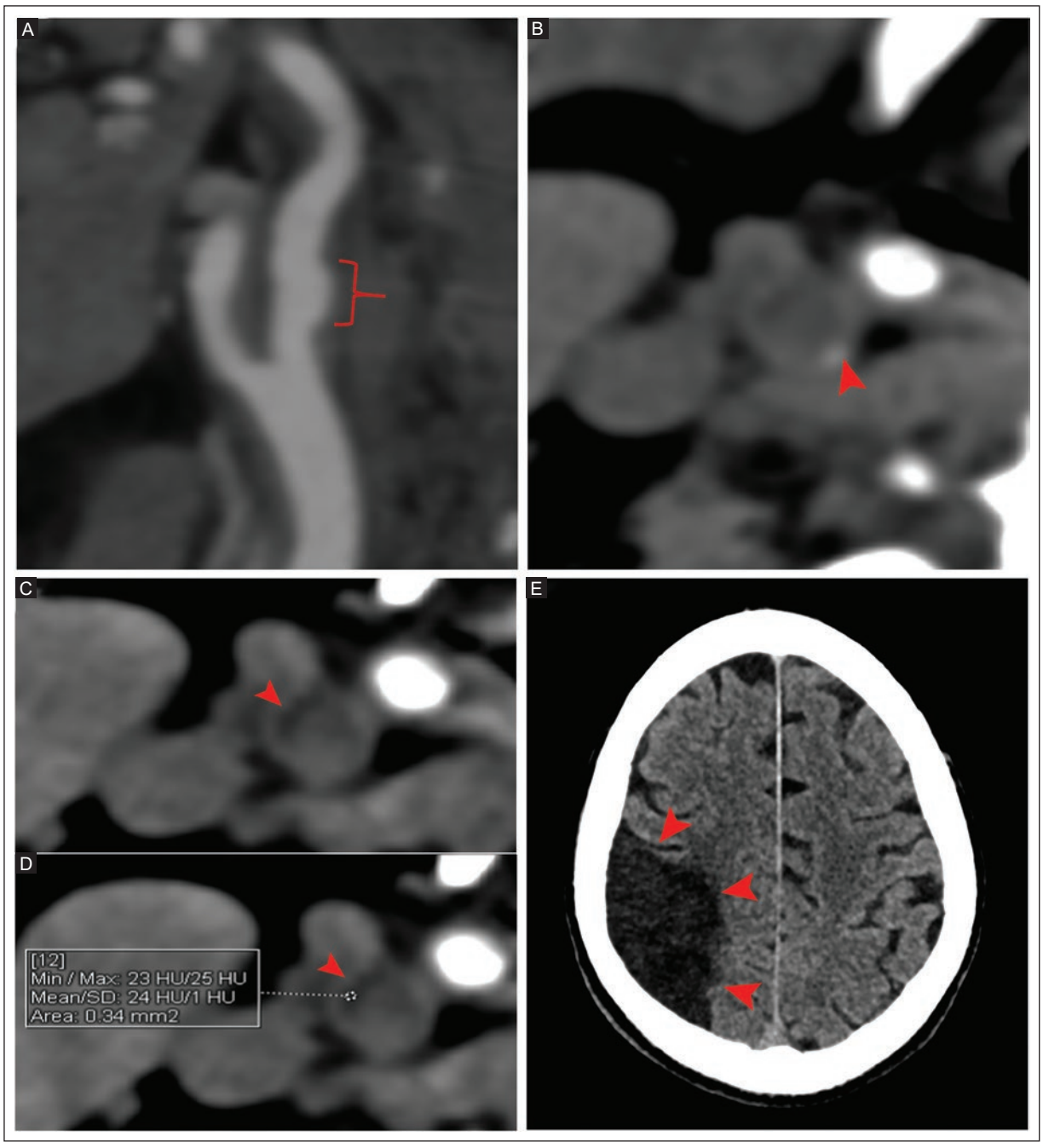

Figure 2. Head and neck CT of the right carotid artery shows a non-stenotic carotid plaque with high-risk morphological characteristics in a 67-year-old man presenting with sudden-onset left hemiparesis, right lip deviation, and dysarthria, without altered consciousness. The initial CT ruled out hemorrhage and demonstrated an ipsilateral cerebral infarction. **A:** MIP arterial phase in the oblique sagittal plane shows contrast extending > 1 mm beyond the luminal contour, indicating plaque ulceration in the right carotid bulb (red curly bracket). **B:** unenhanced-phase axial view showing an atherosclerotic plaque with punctate calcification (red arrowhead). **C-D:** unenhanced-phase views of the right carotid bulb show an intraplaque hypodense component (red arrowheads) and an ROI of 24 ± 1 HU consistent with a lipid-rich necrotic core. **E:** unenhanced-phase view showing a wedge-shaped hypodense area in the right cerebral hemisphere, consistent with an ipsilateral subacute cerebral infarction (red arrowheads). The diagnosis was ESUS ipsilateral to the non-stenotic carotid plaque.

CT: computed tomography; CTA: computed tomography angiography; ESUS: embolic stroke of undetermined source; HU: Hounsfield units; MIP: maximum intensity projection; ROI: region of interest.

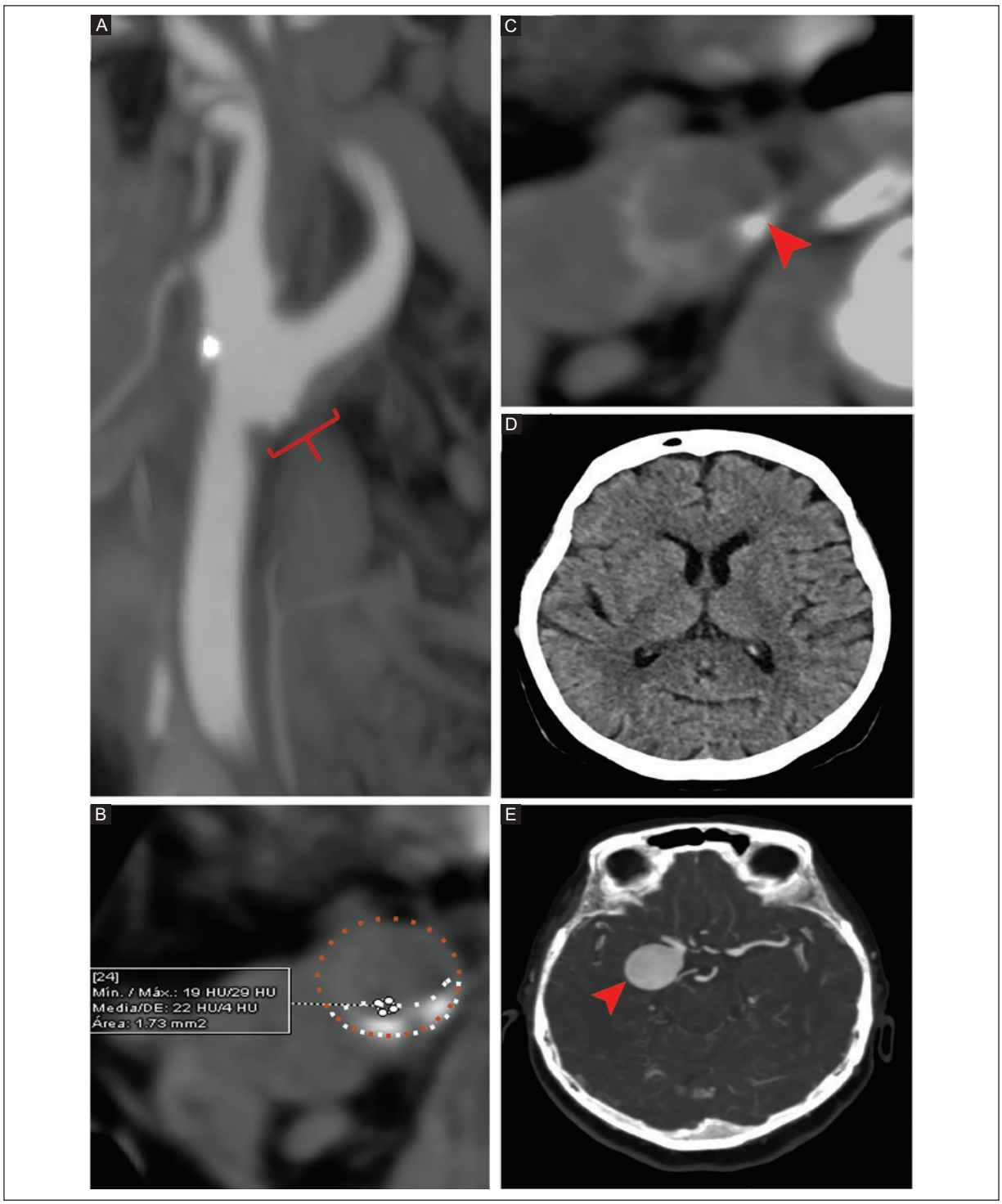

Figure 3. Head and neck CTA in a 56-year-old woman with a sudden onset of right hemicranial headache (NAS 10/10), right eyelid ptosis, and retroauricular and retro-orbital pain secondary to an intracranial aneurysm. Non-stenotic carotid plaque with high-risk morphological characteristics was an incidental finding. **A:** arterial-phase MIP in the oblique sagittal plane of the right carotid, demonstrating contrast extending > 1 mm beyond the luminal contour, indicating plaque ulceration in the carotid bulb associated with punctate calcifications (red curly bracket). **B:** unenhanced-phase axial view of the right carotid bulb showing a plaque outlined by white dotted lines, with the carotid lumen indicated by orange dotted lines. The plaque contains punctate calcifications and a hypodense component with an attenuation of 22 ± 4 HU (ROI), consistent with a lipid-rich necrotic core. **C:** unenhanced-phase view of the right carotid bulb showing punctate subendothelial calcification (red arrowhead). **D:** unenhanced-phase view at the level of the basal ganglia, with no evidence of cerebral infarction. **E:** arterial phase axial view shows a saccular arterial dilation in the posterior communicating segment of the right internal carotid artery (red arrowhead).

CTA: computed tomography angiography; HU: Hounsfield units; MIP: maximum intensity projection; NAS: numerical analog scale; ROI: region of interest.

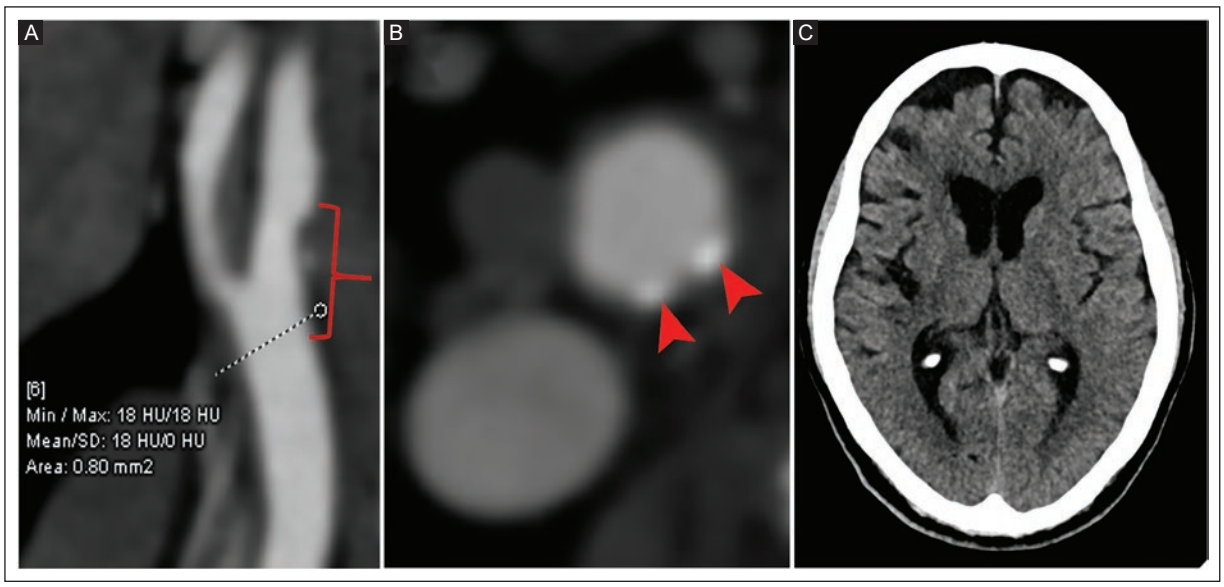

Figure 4. Head and neck CT of a 55-year-old woman with a history of epilepsy. The head CT showed no evidence of an acute ischemic event (not shown). A non-stenotic carotid plaque with high-risk morphologic characteristics was incidentally identified. **A:** oblique sagittal arterial-phase MIP shows an irregular plaque extending from the common carotid artery toward the carotid bulb and the right internal carotid artery (red curly bracket). A hypodense intraplaque area is identified with an ROI of 18 ± 0 HU, suggesting a lipid-rich necrotic core. **B:** arterial-phase axial view at the level of the right carotid bulb shows subendothelial punctate calcifications (red arrowheads). **C:** unenhanced-phase view shows decreased brain volume in the right hemisphere, with widened sulci related to atrophy.

CT: computed tomography; CTA: computed tomography angiography; ESUS: embolic stroke of undetermined source; HU: Hounsfield units; MIP: maximum intensity projection; ROI: region of interest.

The authors concluded that non-stenotic carotid plaques are highly prevalent in patients with ESUS and may represent an underrecognized embolic source in ischemic stroke. Ospel et al.[11] analyzed an international, multicenter cohort of 138 patients with ESUS who underwent head and neck CTA. Non-stenotic carotid plaques were more frequent in patients with ESUS than in those with non-ESUS (54/138, 39.1% vs 77/308, 25.0%; p = 0.002). Among patients with ESUS, non-stenotic carotid plaques were more frequent ipsilateral to the ischemic event than in the contralateral carotid artery (40/137, 29.2% vs 26/139, 18.7%; p = 0.041). In our study, the prevalence of high-risk and non-high-risk non-stenotic carotid plaques was elevated; however, the morphological characteristics did not show a significant association with ipsilateral ESUS compared to patients without ESUS but with other neurological diseases. This discrepancy could be due to methodological differences, particularly the lack of a contralateral carotid artery comparison and the selection of the comparison group without ESUS based on a higher atherosclerotic burden.

Non-stenotic carotid plaques with vulnerability features are associated with a higher risk of ischemic recurrence. In a meta-analysis of 2,350 patients, Rizvi et al.[18] reported that intraplaque hemorrhage was associated with an annualized rate of ischemic events of 11.9%, while lipid necrotic core and rupture or thinning of the fibrous cap showed rates of 5.4% and 5.7%, respectively[19]. Furthermore, intraplaque hemorrhage has been identified as an independent predictor of recurrence, with ipsilateral stroke rates of 9.0% per year in patients with less than 50% carotid stenosis (odds ratio of 11.0) compared to 0.7% in the absence of intraplaque hemorrhage[19]. In a meta-analysis by Singh et al.[20] that included 31 studies with 13,428 patients with non-stenotic carotid plaque, the incidence of associated ischemic events was evaluated using various imaging techniques-ultrasound, CTA, magnetic resonance angiography, or digital subtraction angiography. In patients with asymptomatic non-stenotic carotid plaque, the incidence of the first stroke or TIA event was 0.5 per 100 person-years; in contrast, in symptomatic non-stenotic plaques, the recurrence rate was 2.6 per 100 person-years, and in those with intraplaque hemorrhage 4.9 per 100 person-years. In our study, a high proportion of patients with a history of ipsilateral ischemic stroke related to the non-stenotic carotid

plaque was identified in 140 (80.0%) patients in the ipsilateral ESUS group compared to 4 (1.7%) in the group without ipsilateral ESUS ($p < 0.001$), indicating a high recurrence rate in ESUS group. Likewise, a higher frequency of prior TIA was found in patients with ipsilateral ESUS (n = 56, 32.0%) compared to the group without ESUS (n = 38, 16.2%) ($p < 0.001$). These findings are consistent with those reported in a meta-analysis by Singh et al.[20] which found that symptomatic non-stenotic carotid plaque with high-risk morphological features was associated with a higher risk of ESUS recurrence. In our study, a high frequency of history of stroke and TIA was observed in the ipsilateral ESUS group, suggesting a clinical pattern compatible with a higher risk of recurrence. Non-stenotic carotid plaque may be associated with an increased risk of recurrent ischemic events, particularly in patients with high-risk carotid plaque morphology, suggesting its potential as an embolic source.

Among the strengths of this study are the sample size, the systematic evaluation using head and neck CTA in all patients, and the characterization of morphological features of non-stenotic carotid plaque, which has traditionally been underestimated in the etiological evaluation of stroke. However, the study has limitations related to its retrospective design. Carotid plaque characterization was performed solely using head and neck CTA, without the inclusion of vascular wall MRI. Moreover, it was not possible to definitively establish a causal relationship between plaque characteristics and the ischemic event due to the possible coexistence of other causes not routinely evaluated, such as subclinical atrial fibrillation, atrial cardiomyopathy, small intracavitary thrombi, and hereditary or acquired thrombophilias. Finally, the clinical characteristics and their relationship to the morphological features of the non-stenotic carotid plaque are not described.

CONCLUSION

In our study, the most common high-risk morphological characteristics of non-stenotic carotid plaque on head and neck CTA in patients with ipsilateral ESUS were an irregular surface and ulceration. Prospective studies with larger sample sizes, including assessment of the contralateral carotid and complementary imaging techniques, are needed to enable more detailed characterization of the morphological features of non-stenotic carotid plaque in ESUS.

Acknowledgments

The authors thank Professor Ana M. Contreras-Navarro for her guidance in preparing and writing this scientific paper. This original research in the Radiology Specialty field was an awarded thesis at the Cuarta Convocatoria Nacional 2025-2026 "*Las Mejores Tesis para Publicar en el JMeXFRI*".

Funding

The authors declare that they have not received funding.

Conflicts of interest

The authors declare no conflicts of interest.

Ethical considerations

Protection of human subjects and animals. The authors declare that the procedures followed were in accordance with the ethical standards of the responsible committee on human experimentation and with the World Medical Association and the Declaration of Helsinki (1964). The procedures were authorized by the Institutional Ethics Committee.

Confidentiality, informed consent, and ethical approval. The authors have obtained approval from the Ethics Committee for the analysis of routinely collected and anonymized clinical data. Informed consent was not required for this observational study of information collected during routine clinical care.

Declaration on the use of artificial intelligence. The authors declare that no generative artificial intelligence was used in the writing or creation of the content of this manuscript.

REFERENCES

1. Ntaios G. Embolic stroke of undetermined source. J Am Coll Cardiol. 2020;75(3):333-340. doi:10.1016/j.jacc.2019.11.024.
2. Hart RG, Diener HC, Coutts SB, Easton JD, Granger CB, O'Donnell MJ, et al. Cryptogenic Stroke/ESUS international working group. Embolic strokes of undetermined source: the case for a new clinical construct. Lancet Neurol . 2014;13(4):429-438. doi:10.1016/S1474-4422(13)70310-7.
3. Guirguis-Blake JM, Webber EM, Coppola EL. Screening for asymptomatic carotid artery stenosis in the general population: updated evidence report and systematic review for the US Preventive Services Task Force. JAMA. 2021;325(5):487-499. doi: 10.1001/jama.2020.20364.
4. Abbott AL, Brunser AM, Giannoukas A, Harbaugh RE, Kleinig T, Lattanzi S, et al. Misconceptions regarding the adequacy of best medical intervention alone for asymptomatic carotid stenosis. J Vasc Surg. 2020;71(1): 257-269. doi: 10.1016/j.jvs.2019.04.490.
5. Ospel JM, Kappelhof M, Ganesh A, Kallmes DF, Brinjikji W, Goyal M. Symptomatic non-stenotic carotid disease: current challenges and opportunities for diagnosis and treatment. J Neurointerv Surg. 2024;16(4):418-424. doi: 10.1136/jnis-2022-020005.

6. Homssi M, Saha A, Delgado D, RoyChoudhury A, Thomas C, Lin M, et al. Extracranial carotid plaque calcification and cerebrovascular ischemia: a systematic review and meta-analysis. Stroke. 2023;54(10):2621-2628. doi:10.1161/STROKEAHA.123.042807.
7. Guo D, Lv S, Wu G, Li H, Wei B, Yang J. Features of non-stenotic carotid plaque on computed tomographic angiography in patients with embolic stroke of undetermined source. Front Cardiovasc Med. 2022; 9:971500. doi:10.3389/fcvm.2022.971500.
8. Grant EG, Benson CB, Moneta GL, Alexandrov AV, Baker JD, Bluth EI, et al. Carotid artery stenosis: gray-scale and Doppler US diagnosis–Society of Radiologists in Ultrasound consensus conference. Radiology. 2003;229(2):340-346. doi: 10.1148/radiol.2292030516.
9. Stary HC, Chandler AB, Dinsmore RE, Fuster V, Glagov S, Insull W Jr, et al. A definition of advanced types of atherosclerotic lesions and a histological classification of atherosclerosis: a report from the Committee on Vascular Lesions of the Council on Arteriosclerosis, American Heart Association. Circulation. 1995;92(5):1355-1374. doi:10.1161/01.CIR.92.5.1355.
10. Tarkin JM, Joshi FR, Rudd JHF. PET imaging of inflammation in atherosclerosis. Nat Rev Cardiol . 2014;11(8):443-457. doi: 10.1038/nrcardio. 2014.80.
11. Ospel JM, Marko M, Singh N, Goyal M, Almekhlafi MA. Prevalence of non-stenotic (< 50%) carotid plaques in acute ischemic stroke and transient ischemic attack: a systematic review and meta-analysis. J Stroke Cerebrovasc Dis. 2020;29(10):105117. doi:10.1016/j.jstrokecerebrovasdis.2020.105117.
12. Cheng SF, van Velzen TJ, Gregson J, Richards T, Jäger HR, Simister R, et al. The 2nd European Carotid Surgery Trial (ECST-2): rationale and protocol for a randomized clinical trial comparing immediate revascularization versus optimized medical therapy alone in patients with symptomatic and asymptomatic carotid stenosis at low to intermediate risk of stroke. Trials. 2022;23(1):606. doi:10.1186/s13063-022-06429-z.
13. Adams HP Jr, Bendixen BH, Kappelle LJ, Biller J, Love BB, Gordon DL, et al. Classification of subtype of acute ischemic stroke. Definitions for use in a multicenter clinical trial (TOAST). Trial of Org 10172 in Acute Stroke Treatment. Stroke. 1993;24(1):35-41. doi: 10.1161/01.STR.24.1.35.
14. Saba L, Cau R, Vergallo R, Kooi ME, Staub D, Faa G, et al. Carotid artery atherosclerosis: mechanisms of instability and clinical implications. Eur Heart J. 2025;46(10):904-921. doi: 10.1093/eurheartj/ehae933.
15. Kamtchum-Tatuene J, Noubiap JJ, Wilman AH, Saqqur M, Shuaib A, Jickling GC. Prevalence of high-risk plaques and risk of stroke in patients with asymptomatic carotid stenosis: a meta-analysis. JAMA Neurol. 2020;77(12):1524-1535. doi: 10.1001/jamaneurol.2020.2658.
16. Singh N, Ospel J, Mayank A, Marko M, Zaidat OO, Mueller-Kronast NH et al. STRATIS Investigators. Nonstenotic carotid plaques in ischemic stroke: analysis of the STRATIS registry. AJNR Am J Neuroradiol. 2021;42(9):1645-1652. doi: 10.3174/ajnr.A7218.
17. Demir M, Semiz-Oysu A, Ozsezen E, Yasar Y. Nonstenotic carotid artery plaques on computed tomography angiography in embolic stroke of undetermined source. Medicine (Baltimore). 2024;103(51):e40880. doi: 10.1097/MD.0000000000040880.
18. Rizvi A, Seyedsaadat SM, Alzuabi M, Murad MH, Huston J 3rd, Lehman VT, et al. Carotid plaque vulnerability on magnetic resonance imaging and risk of future ischemic events: a systematic review and meta-analysis. J Neurosurg Sci. 2020;64(5):480-486. doi: 10.23736/S0390-5616.20.04959-0.
19. Savastano L, Brinjikji W, Lutsep H, Chen H, Chaturvedi S. Symptomatic nonstenotic carotids: a topical review. Stroke. 2024;55(12):2921-2931. doi:10.1161/STROKEAHA.123.035675.
20. Singh N, Marko M, Ospel JM, Goyal M, Almekhlafi M. The risk of stroke and tia in nonstenotic carotid plaques: a systematic review and meta-analysis. AJNR Am J Neuroradiol. 2020;41(8):1453-1459. doi: 10.3174/ajnr.A6613.

JMeXFRI

Journal of the Mexican Federation of Radiology and Imaging

Check for updates

FULL RESEARCH ARTICLE

Agreement between volBrain and mdbrain AI software for thalamic and white matter lesion volumetry in multiple sclerosis

Rodrigo I. Brito-Delgado[1], *Eduardo Torres-Olivas*[1]* and *Arturo Hernandez-Medina*[1,2]

[1]Department of Magnetic Resonance, Hospital Angeles Lomas, Huixquilucan, State of Mexico; [2]Biomedical Engineering Area, Faculty of Engineering, Universidad Autonoma de Queretaro, Queretaro, Qro. Mexico

ABSTRACT

Introduction: *Artificial intelligence (AI)-based software platforms utilizing magnetic resonance imaging (MRI) have been developed to quantify brain structures and white matter lesions (WML) in patients with multiple sclerosis (MS). This study evaluated the agreement between volBrain and mdbrain software for thalamic and WML volumetry in patients with MS.* **Material and methods:** *This retrospective cross-sectional study included patients with MS. MRI examinations were performed on 1.5T or 3.0T scanners. Thalamic and WML volumes obtained with volBrain software were compared with those generated by mdbrain software. Statistical analysis included Student's paired t-test or the Wilcoxon signed-rank test, correlation analysis, and the Bland-Altman agreement assessment.* **Results:** *In 31 MS patients, the mean thalamic volume with volBrain was 14.48 ± 1.88 mL; the mean with mdbrain was 14.29 ± 1.94 mL. volBrain and mdbrain showed excellent thalamic volumetry agreement, with a bias of -0.194 mL and narrow limits of agreement (−1.199, 0.810) without proportional bias. WML volumetry exhibited significant disagreement between volBrain and mdbrain, with median volumes of 3.32 mL (IQR 5.08) and 4.48 mL (IQR 6.25), respectively. WML volumetry demonstrated minimal bias (0.062 mL) but wider limits of agreement (−5.588, 5.713) and significant proportional bias ($p < 0.001$).* **Conclusion:** *Agreement between volBrain and mdbrain for thalamic volumetry using MRI in patients with MS was excellent. However, proportional bias was observed in WML volumetry, particularly with high WML volume. VolBrain showed greater disagreement with mdbrain as lesion volume increased, suggesting that AI software may not be interchangeable for evaluating patients with MS.*

Keywords: *Multiple sclerosis. Thalamus. White matter lesion. mdbrain. volBrain. Artificial intelligence.*

INTRODUCTION

Artificial intelligence (AI) tools for automated brain volume and white matter lesion (WML) assessment have been integrated into clinical magnetic resonance imaging (MRI) workflows for patients with multiple sclerosis (MS)[1,2]. Thalamic atrophy is an early and sensitive marker of neurodegeneration, associated with physical disability and cognitive decline in MS[3-5], while WML volume reflects the accumulated inflammatory burden[6]. Several studies have demonstrated the utility of automated AI-based brain segmentation tools for estimating lesion volumes and burden in MS patients[1,7-9].

Commercial software platforms such as icobrain[10], Pixyl.Neuro.MS[11], Jazz[12], NeuroQuant[13], FIRST[14], and mdbrain[1], among others, provide automated detection and segmentation of WML. The machine-learning-based software mdbrain uses standard MRI sequences to measure brain volume, analyze gray and white matter volumes, and assess WML in MS patients[1]. Mdbrain provides radiologists with automatic lesion load quantification, and it is CE-certified clinical software[2]. In contrast,

***Corresponding author:**
Eduardo Torres-Olivas
E-mail: etorres_1509@hotmail.com

Received for publication: 11-12-2025
Accepted for publication: 18-02-2026
DOI: 10.24875/JMEXFRI.M26000127

Available online: 08-07-2026
J Mex Fed Radiol Imaging. 2026;5(2):126-133
www.JMeXFRI.com

Table 1. Brain MRI 1.5T and 3.0T segmentation and volumetry protocol with mdbrain AI software in patients with MS

Field strength	Sequence	TI (ms)	FOV (mm)	Matrix	TR (ms)	TE (ms)	Magnetic preparation (ms)	Flip angle (degree)	Slice thickness (mm)
1.5T	T1-MPRAGE 3D	No	250 × 250	256 × 256	2200	2.67	900	8	1.0
	SPACE 3D FLAIR	1600	260 × 260	220 × 256	5000	335	125	120-90	1.0
3.0T	T1-MPRAGE 3D	No	240 × 240	256 × 256	2300	2.32	900	8	0.9
	SPACE 3D FLAIR	2050	230 × 230	256 × 256	7000	395	125	120-90	0.9

FLAIR: fluid-attenuated inversion recovery; FOV: field of view; MPRAGE: magnetization-prepared rapid gradient echo; MRI: magnetic resonance imaging; MS: multiple sclerosis; SPACE: sampling perfection with application-optimized contrasts using different flip-angle evolutions; T: tesla; T1-weighted image; TE: time-echo; TI: inversion-recovery time; TR: time repetition.

the volBrain platform is an open-access, online tool with a user-friendly interface and fully automated processing pipelines[8,15]. The volBrain platform has demonstrated high performance, consistency, and accuracy in segmenting subcortical structures and assessing regional atrophy metrics[8,15,16].

The agreement between mdbrain, used in clinical assessments of patients with MS, and other software used in research, such as volBrain, has not been established[15]. It is unknown whether high WML volume affects agreement among AI systems in volumetric assessment of deep brain structures, such as the thalamus; therefore, this study evaluated agreement between volBrain and mdbrain AI in assessing thalamic and WML volumes in patients with MS.

MATERIAL AND METHODS

This cross-sectional, retrospective study was conducted from April 2025 to January 2026 in the Magnetic Resonance Department of Hospital Angeles Lomas in Huixquilucan, State of Mexico, Mexico. MS patients who underwent brain MRI scans were included. Low-quality MRI scans or those without an mdbrain report were excluded. Informed consent was not required because information was collected during routine clinical care. The institutional Research and Ethics in Research Committees approved the study.

Study development and variables

For this research, we used the database from a previous study of patients with MS[16]. We recorded age, sex, thalamus volume, and WML obtained with volBrain and mdbrain software.

Imaging and analysis protocol

A 1.5T MAGNETOM Aera or a 3.0T MAGNETOM Skyra Fit MRI scanner (Siemens Healthineers, Erlangen, Germany) was used. The workflow for volBrain software was described previously[16]. The protocol for segmentation and volumetry with mdbrain software in MS patients is shown in table 1. All images were acquired with a 32-channel head coil. Brain MRI was performed using our institution's MS protocol, including 3D T1-weighted magnetization-prepared rapid acquisition gradient-echo (T1-MPRAGE) and volumetric T2-weighted fluid-attenuated inversion recovery (T2-FLAIR) sequences with standard clinical acquisition parameters.

mdbrain AI software

The sequences for post-processing by mdbrain AI software v4.13.0 (Mediaire GmbH, Berlin, Germany) were obtained from the Picture Archiving and Communication System (PACS) Orchestrator (Philips, Eindhoven, Netherlands). Mdbrain software functions as a PACS-integrated module and provides two reports related to brain and WML volumetry. The first report segments three tissue classes and 21 brain regions, including thalamic volume, using T1-MPRAGE. The second report, WML characterization, is automatically segmented from a T2-FLAIR sequence using a deep convolutional neural network (U-Net), trained on 280 heterogeneous patient datasets from different scanner types and sequences[9].

Statistical analysis

The Shapiro-Wilk test was used to assess the distribution of quantitative variables. Thalamic volume and age were normally distributed and are expressed as means and standard deviations (SD). WML volumetry was a nonparametric variable expressed as a median and interquartile range (IQR). Comparisons between volBrain and mdbrain software were performed using Student's paired *t*-test and the Wilcoxon signed-rank test for normal and nonparametric variables, respectively.

Table 2. Age, sex, and volumetry values of patients with MS comparing volBrain and mdbrain AI software

Description	Parameter	
Age, years, mean ± SD (min-max)	45.4 ± 12.5 (20-70)	
Sex, n (%)		
Women	21 (67.7)	
Men	10 (32.3)	
Segmentation	volBrain software	mdbrain software
Thalamus volume (mL), mean ± SD (min-max)	14.48 ± 1.88 (10.54-19.58)	14.29 ± 1.94 (8.80-19.60)
WML volume (mL), median, IQR (min-max)	3.32, 5.08 (0.02-30.19)	4.48, 6.25 (0.29-19.40)

IQR: interquartile range; MS: multiple sclerosis; SD: standard deviation; WML: white matter lesion.

Pearson and Spearman correlations were also performed between thalamic and WML volumetry for both software. The Bland-Altman plot was used to assess the bias and limits of agreement between the software. To assess proportional bias, linear regression was performed on the differences of the measurements and the mean of the two software; a slope significantly different from zero was considered proportional bias. A $p < 0.05$ was considered statistically significant. The analysis was performed with RKWard v0.8.0[17].

RESULTS

Forty MS patients were eligible. Nine patients were excluded because the mdbrain report was not completed. Thirty-one patients with a mean age of 45.4 ± 12.5 years (range 20 to 70) were included. There were 21 (67.7%) women and 10 (32.3%) men (Table 2). The mean thalamus volume with volBrain was 14.48 ± 1.88 mL, with a minimum of 10.54 mL and a maximum of 19.58 mL. The mean thalamus volume with mdbrain was 14.29 ± 1.94 mL, with a minimum of 8.80 mL and a maximum of 19.60 mL. Regarding WML volume, the median with volBrain was 3.32 mL (IQR 5.08) with a minimum of 0.02 mL and a maximum of 30.19 mL. The median with mdbrain was 4.48 mL (IQR 6.25) with a minimum of 0.29 mL and a maximum of 19.40 mL. Measures of central tendency were comparable between the two software for the thalamus; however, the Wilcoxon signed-rank test showed a statistically significant difference ($p = 0.016$) for WML volume, indicating a shift in the distribution of measurements between the two software.

Correlation between volBrain and mdbrain for thalamic and WML volume

Scatterplots show the correlation between volBrain and mdbrain for thalamic and WML volume using MRI segmentation in patients with MS (Figure 1). The Pearson correlation for thalamic volume measured by the two software was $r = 0.96$ ($p < 0.001$). The Spearman correlation for WML volume measured by volBrain and mdbrain was $r = 0.97$ ($p < 0.001$). The correlation between the two software was nearly perfect, with close proportional growth between the measured values. The evaluation of each patient with both software programs showed an almost perfect correlation.

Comparison of thalamus and WML volumes with volBrain and mdbrain

Figure 2 shows a comparison of the correlation coefficient of thalamic volume, which was $r = -0.40$ ($p = 0.025$), and WML volume, which was $r = -0.39$ ($p = 0.027$), using volBrain and mdbrain, respectively. Both datasets have a negative slope, with a significant correlation between higher WML volume and lower thalamic volume. This is seen in the graph, where each dataset appears to have high dispersion, but statistical analysis reveals a trend. Some values are outliers; for example, in volBrain, three patients have WML volumes of 24.95 mL, 26.15 mL, and 30.19 mL, while the remaining values are below 20 mL. In mdbrain, one patient has a thalamic volume of 8.80 mL, and all other values are greater than 10 mL.

Agreement between volBrain and mdbrain for thalamic and WML volume estimation

Bland-Altman plots show the agreement between volBrain and mdbrain for thalamic and WML volume using MRI segmentation in patients with MS (Figure 3). The mean difference for thalamic volume was −0.194 mL (limits of agreement: −1.199, 0.810) with higher values for volBrain indicating a tendency for volBrain to segment larger volumes, but without a proportional bias (slope = 0.0347, $p = 0.491$). The agreement between the two software programs for thalamic segmentation and volumetry was adequate. The mean difference for WML volume segmentation was 0.062 mL (limits of agreement: −5.588, 5.713). Three outlier values were observed (mean measurements of 24.73 mL, 22.77 mL, and 22.12 mL; differences between software were −10.91 mL, −6.75 mL, and −5.65 mL, respectively).

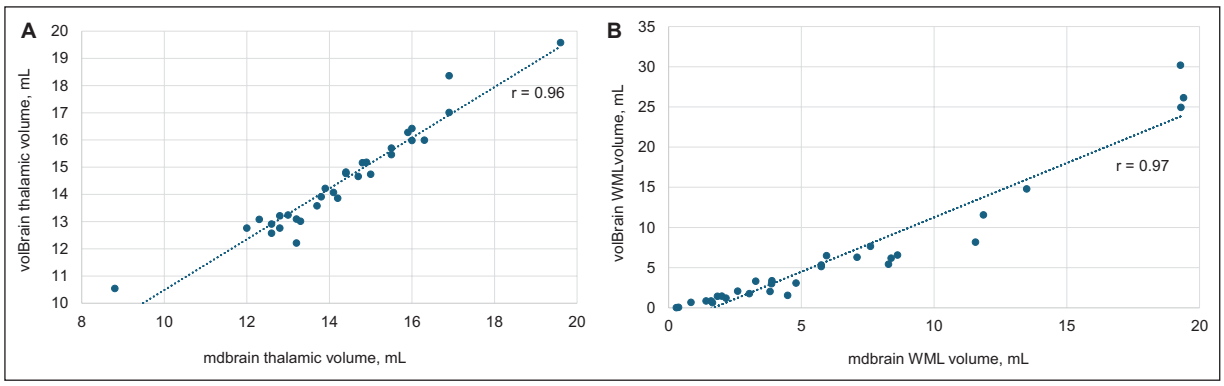

Figure 1. Scatterplots show the correlation between volBrain and mdbrain software for thalamic and WML volume using MRI segmentation in patients with MS. **A:** the Pearson correlation of thalamic volume measured by the two software was r = 0.96 ($p < 0.001$). **B:** the Spearman correlation of WML volume measured by volBrain and mdbrain was r = 0.97 ($p < 0.001$). Values show a similar trend with excellent correlation.

MRI: magnetic resonance imaging; MS: multiple sclerosis; WML: white matter lesion.

WML volumetry demonstrated minimal bias (0.062 mL) but wider limits of agreement (–5.588, 5.713) and significant proportional bias ($p < 0.001$), indicating disagreement between volBrain and mdbrain in WML segmentation and volumetry.

Figure 4 shows representative axial T1-MPRAGE images with overlaid automated brain MRI segmentation masks, comparing volBrain and mdbrain in a patient with MS. Both software delineated comparable thalamic regions, with similar extent and morphology in the axial slice shown. This visual finding aligns with the agreement demonstrated in the Bland-Altman analysis, where bias was minimal (–0.194 mL), and no proportional bias was observed. Differences in the extent and boundaries of other segmented brain regions reflect the distinct atlas-based and deep learning approaches used by each software. Figure 5 shows two representative patients with high and low WML volumes, illustrating the differences in automated WML segmentation between the two software packages. In the patient with low WML volume (Figures 5A-B), segmentation was similar between volBrain and mdbrain, with minor discrepancies in some small lesions detected by only one software. In the patient with high WML volume (Figures 5C-D), segmentation differed substantially between the software; volBrain delineated a greater extent of periventricular WML than mdbrain, although it did not segment a WML in the left frontal lobe. These visual differences are consistent with the proportional bias identified in the Bland-Altman analysis, which showed that the greater the WML volume, the greater the discrepancy between software, predominantly due to larger volumes segmented by volBrain.

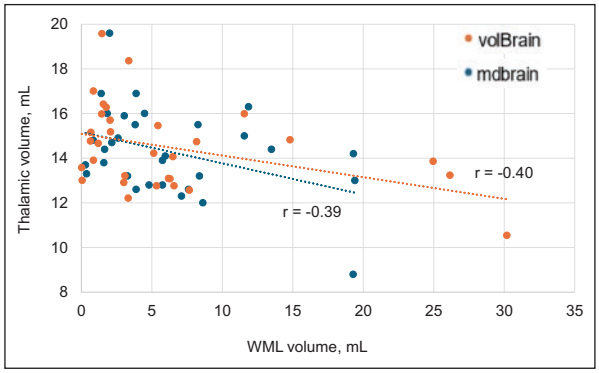

Figure 2. Scatterplot of MRI volumetry of the thalamus and WML comparing volBrain (orange marks) and mdbrain (blue marks) in patients with MS. The correlation coefficient for thalamic volume was r = –0.40 ($p = 0.025$) and for WML volume was r = –0.39 ($p = 0.027$) with volBrain and mdbrain, respectively. Three pairs of outlier values above 15 mL were observed in WML segmentation for both software (24.95 mL, 26.15 mL, and 30.19 mL vs. 19.3 mL, 19.4 mL and 19.28 mL for volBrain and mdbrain, respectively) indicating increased extreme values of WML volumetry using volBrain.

MRI: magnetic resonance imaging; MS: multiple sclerosis; WML: white matter lesion.

DISCUSSION

Our study found high agreement between volBrain and mdbrain AI software in thalamic volumetry in patients with MS. However, WML volume quantification showed a significant proportional bias toward higher WML volumes: as lesion volume increased, volBrain showed greater disagreement with mdbrain. Therefore, it is recommended not to change the software used for the clinical follow-up of MS patients, as within-subject measurement bias may occur when switching software.

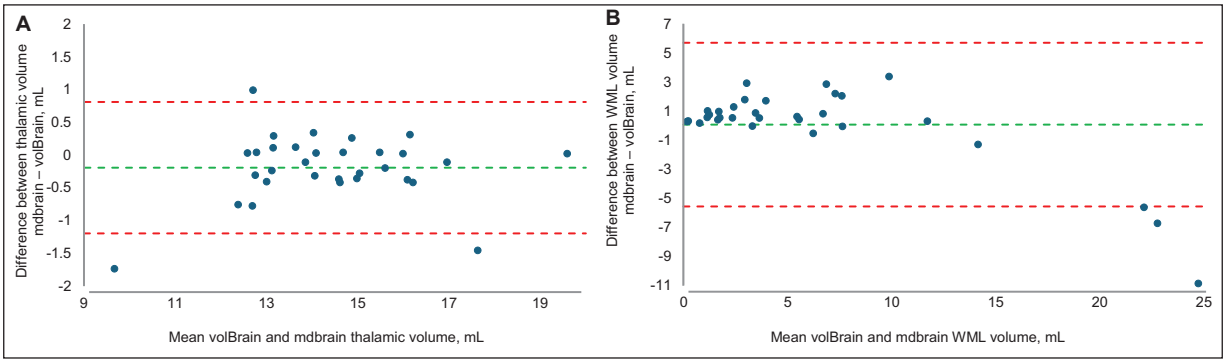

Figure 3. Bland-Altman plots showing agreement between volBrain and mdbrain for thalamic and WML volume using MRI segmentation in patients with MS. Bias is indicated by the dashed green line, and the limits of agreement (1.96 standard deviations) by the dashed red lines. **A:** the mean difference for thalamic volume was –0.194 mL (–1.199, 0.810). For the thalamus, agreement between volBrain and mdbrain was demonstrated, with three patients outside the limits of agreement, but without proportional bias. **B:** the mean difference for WML volume segmentation was 0.062 mL (–5.588, 5.713). Three outlier values were observed (mean measures of 24.73 mL, 22.77 mL, and 22.12 mL; postprocessing differences of –10.91 mL, –6.75 mL, and –5.65 mL, respectively) with higher values for volBrain. WML volumetry showed significant proportional bias (slope = –0.343, $p < 0.001$), indicating a difference between volBrain and mdbrain dependent on WML burden.

MRI: magnetic resonance imaging; MS: multiple sclerosis; WML: white matter lesion.

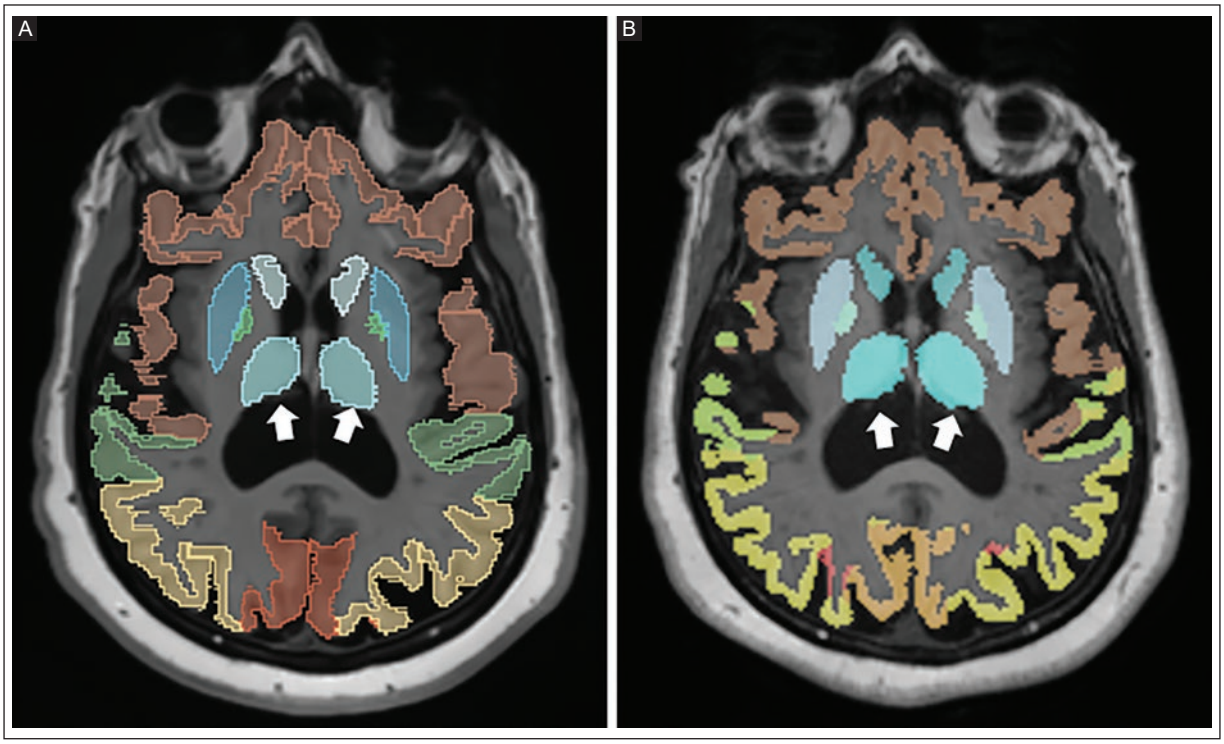

Figure 4. Representative axial T1-MPRAGE images with overlaid automated brain MRI segmentation masks, comparing **A:** volBrain and **B:** mdbrain, in a patient with MS. Both software delineate comparable thalamic regions (arrows). Differences in the extent and boundaries of other segmented brain regions reflect the distinct atlas-based and deep learning approaches used by each method.

MPRAGE: magnetization-prepared rapid acquisition gradient echo; MRI: magnetic resonance imaging; MS: multiple sclerosis.

Volumetry of deep structures such as the thalamus using AI is reproducible. Evidence of thalamic atrophy is associated with clinical progression of MS[3,18]. We found agreement in thalamic volume using two software programs: volBrain and mdbrain for segmentation and automatic volumetry. No significant differences were found between the measured values. Koussis et al.[13] evaluated brain volumes in 56 Greek patients (22 men

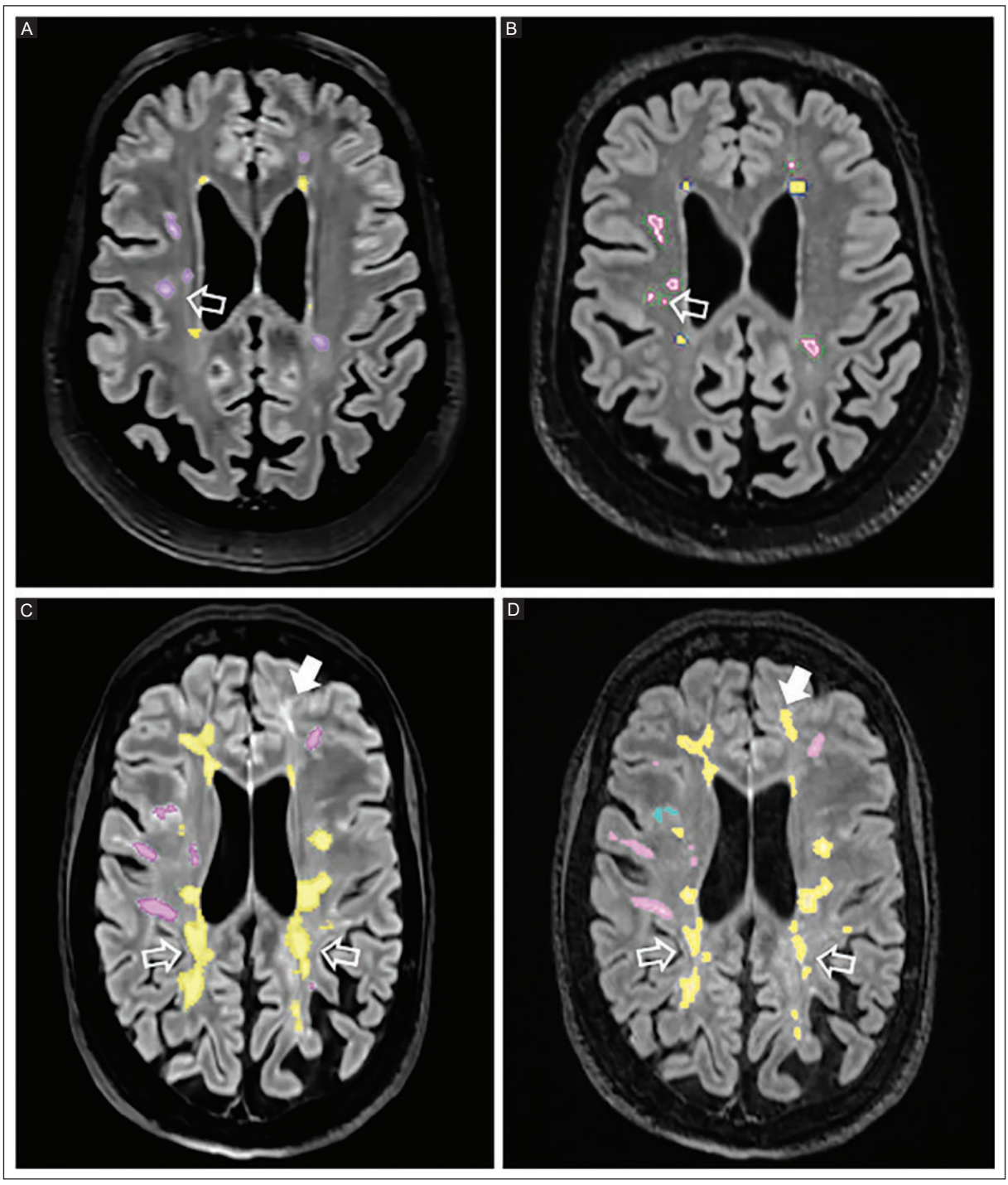

Figure 5. Axial MRI reformats from SPACE 3D FLAIR with overlaid automated WML masks, comparing volBrain and mdbrain in two patients with different WML volumes. **A:** volBrain and **B:** mdbrain postprocessing image from a 61-year-old woman with low WML volume. The overall MRI segmentation is similar between the two software, with only minor discrepancies; volBrain unifies one WML while mdbrain segments it as two separate lesions (void arrows). **C:** volBrain and **D:** mdbrain postprocessing image from a 50-year-old man with high WML volume. MRI segmentation differs substantially between the software, with volBrain delineating a larger periventricular WML extent than mdbrain (void arrows). Note that volBrain did not segment one WML in the left frontal lobe (solid arrow).

MRI: magnetic resonance imaging; MS: multiple sclerosis; SPACE 3D FLAIR: sampling perfection with application optimized contrasts using different flip angle evolution 3D fluid-attenuated inversion recovery; WML: white matter lesion.

and 34 women) aged 18 to 70 years. Of these, 27 (48.2%) had MS, 21 (37.5%) had dementia, and 8 (14.3%) were healthy. NeuroQuant and volBrain were compared using 3D T1-weighted sequences. Intracranial volume, putamen, thalamus, amygdala, cerebrum, cerebellum, white matter, and the hippocampus were assessed. Paired *t*-test analysis showed significant differences ($p < 0.001$) in all segments except the hippocampus. Good to excellent linear regression and intraclass correlation coefficient (ICC) were found in most measurements, indicating that NeuroQuant and volBrain can detect the relative size of each brain segment. The use of automated brain volumetry software is strongly recommended for research and clinical studies to evaluate and interpret a patient's condition. However, changing software or scanning parameters during a research project or patient monitoring should be avoided, as this may lead to severe errors and misleading results[13]. Tekin et al.[8] in a retrospective study, assessed 100 Turkish individuals, including 50 patients diagnosed with MS and 50 healthy controls. They used volBrain as an automated segmentation tool and reported significant differences in volume values between the groups ($p < 0.001$) for the putamen, thalamus, and globus pallidus with subcortical atrophy in MS patients[8]. Our study found agreement between the two software packages for thalamic volume in MS patients with no evidence of proportional bias. Thalamic volumetry was highly reproducible between volBrain and mdbrain.

Volumetric quantification of WML is important for evaluating inflammatory activity, progression, and therapeutic response in patients with MS[19]. The literature reports that changes in acquisition sequence parameters, artifacts during acquisition, scanner changes, and the use of different AI software in the same MS patient to evaluate clinical evolution can lead to errors in assessing the thalamus and WML[1,9,13,19]. Pareto et al.[20] used a database of 115 patients with clinically isolated syndrome (CIS); 39 were classified as MS due to their symptoms at a follow-up of up to 3 years, the rest remained as CIS. The sample was collected as part of an ongoing research protocol. The goal of the study was to assess agreement between NeuroQuant and FIRST in estimating overall and regional volume. Additionally, WML volume was estimated with NeuroQuant and the Lesion Segmentation Toolbox (LST). They found that brain volume agreement between NeuroQuant and FIRST depends on the structure of interest, with larger structures showing better agreement. Agreement was low (ICC < 0.40) for smaller structures such as the amygdala and globus pallidus, fair to good (ICC > 0.40) for the thalamus, putamen, hippocampus, and total intracranial volume, and fair for lesion volume (ICC = 0.61), with NeuroQuant estimates lower than LST. In our study comparing volBrain and mdbrain, significant differences in central tendency were observed in WML volume among patients with MS. Three values outside the limits of agreement resulted in a significant proportional bias (slope = −0.343, $p < 0.001$); volBrain estimated a larger WML volume when patients with high WML burden were analyzed. This suggests differences in the architecture or training of the neural networks. Therefore, the software programs may not be interchangeable for the clinical monitoring of patients with MS. Our results indicate that volBrain and mdbrain are not interchangeable for the clinical evaluation of patients with MS due to potential segmentation inaccuracies in cases with high WML burden; switching software may introduce artificial volume changes.

One strength of the study is the combined evaluation of deep structures such as the thalamus and WML, both of which are important for monitoring and prognosis in MS. A direct comparison between the two software programs, volBrain and mdbrain, for assessing thalamic and WML volumetry has not been reported previously. The study has limitations, including its small sample size and retrospective design. Therefore, it was not possible to define the variability of findings over time and their relationship with clinical manifestations. Additionally, two different MRI scanners (1.5T and 3.0T) were used. This factor was neither controlled nor evaluated to assess intra-scanner differences, which could introduce inter-scanner variability when comparing the two software programs[9].

CONCLUSION

Our study demonstrated high agreement between volBrain and mdbrain software in thalamic volumetry in MS patients. In contrast, WML volume quantification showed a significant proportional bias: as lesion volume increased, volBrain showed greater disagreement with mdbrain. Larger sample sizes and multicenter studies, including multisoftware studies, are recommended to validate the variability and clinical agreement between software, especially in MS patients with high WML volume.

Acknowledgments

The authors thank Professor Ana M. Contreras-Navarro for her guidance in preparing and writing this scientific paper. This original research in the Radiology

Specialty field was an awarded thesis at the *Cuarta Convocatoria Nacional 2025-2026 "Las Mejores Tesis para Publicar en el JMeXFRI".*

Funding

The authors declare that they have not received funding.

Conflicts of interest

The authors declare no conflicts of interest.

Ethical considerations

Protection of human subjects and animals. The authors declare that the procedures followed were in accordance with the ethical standards of the responsible committee on human experimentation and with the World Medical Association and the Declaration of Helsinki (1964) and subsequent amendments.

Confidentiality, informed consent, and ethical approval. The authors have obtained approval from the Ethics Committee for the analysis of routinely collected and anonymized clinical data; therefore, individual informed consent was not required.

Declaration on the use of artificial intelligence. The authors declare that no generative artificial intelligence was used in the writing or creation of the content of this manuscript.

REFERENCES

1. Rathmann E, Hemkemeier P, Raths S, Grothe M, Mankertz F, Hosten N, et al. Changes in MRI workflow of multiple sclerosis after introduction of an AI-software: a qualitative study. Healthcare (Basel). 2024;12(10):978. doi: 10.3390/healthcare12100978.
2. Peters S, Kellermann G, Watkinson J, Gärtner F, Huhndorf M, Stürner K, et al. AI supported detection of cerebral multiple sclerosis lesions decreases radiological reporting times. Eur J Radiol. 2024;178:111638. doi: 10.1016/j.ejrad.2024.111638.
3. Hänninen K, Viitala M, Paavilainen T, Karhu JO, Rinne J, Koikkalainen J, et al. Thalamic atrophy predicts 5-year disability progression in multiple sclerosis. Front Neurol. 2020;11:606. doi: 10.3389/fneur.2020.00606.
4. Eshaghi A, Prados F, Brownlee WJ, Altmann DR, Tur C, Cardoso MJ, et al. MAGNIMS study group. Deep gray matter volume loss drives disability worsening in multiple sclerosis. Ann Neurol. 2018;83(2):210-222. doi: 10.1002/ana.25145.
5. Houtchens MK, Benedict RH, Killiany R, Sharma J, Jaisani Z, Singh B, et al. Thalamic atrophy and cognition in multiple sclerosis. Neurology. 2007;69(12):1213-1223. doi: 10.1212/01.wnl.0000276992.17011.b5.
6. Vernooij MW, Jasperse B, Steketee R, Koek M, Vrooman H, Ikram MA, et al. Automatic normative quantification of brain tissue volume to support the diagnosis of dementia: a clinical evaluation of diagnostic accuracy. Neuroimage Clin. 2018;20:374-379. doi: 10.1016/j.nicl.2018.08.004.
7. Szekely-Kohn AC, Castellani M, Espino DM, Baronti L, Ahmed Z, Manifold WGK, et al. Machine learning for refining interpretation of magnetic resonance imaging scans in the management of multiple sclerosis: a narrative review. R Soc Open Sci. 2025;12(1):241052. doi:10.1098/rsos.241052.
8. Tekin A, Rende B, Efendi H, Bunul SD, Çakır Ö, Çolak T, et al. Volumetric and symmetric index analysis of subcortical structures in multiple sclerosis patients: a retrospective study using volbrain software. Cureus. 2024;16(3):e55799. doi: 10.7759/cureus.55799.
9. Peters S, Schmill L, Gless CA, Stürner K, Jansen O, Seehafer S. AI-based assessment of longitudinal multiple sclerosis MRI: strengths and weaknesses in clinical practice. Eur J Radiol. 2025;183:111941. doi: 10.1016/j.ejrad.2025.111941.
10. Nguyen AL, Sormani MP, Horakova D, Havrdova EH, Barnett MH, De Stefano N, et al. Utility of icobrain for brain volumetry in multiple sclerosis clinical practice. Mult Scler Relat Disord. 2024;92:106148. doi: 10.1016/j.msard.2024.106148.
11. Mastilović M, Muños-Ramírez V, Rauschecker AM, Boban J, Blanchere M, Cotton F, et al. Artificial intelligence in the detection of multiple sclerosis plaques: can it influence the treatment decision? J Neuroradiol. 2026;53(1):101406. doi: 10.1016/j.neurad.2025.101406.
12. Federau C, Hainc N, Edjlali M, Zhu G, Mastilovic M, Nierobisch N, et al. Evaluation of the quality and the productivity of neuroradiological reading of multiple sclerosis follow-up MRI scans using an intelligent automation software. Neuroradiology. 2024;66(3):361-369. doi:10.1007/s00234-024-03293-3.
13. Koussis P, Toulas P, Glotsos D, Lamprou E, Kehagias D, Lavdas E. Reliability of automated brain volumetric analysis: a test by comparing NeuroQuant and volBrain software. Brain Behav. 2023;13(12):e3320. doi:10.1002/brb3.3320.
14. Vrenken H, Jenkinson M, Horsfield MA, Battaglini M, van Schijndel RA, Rostrup E, et al. Recommendations to improve imaging and analysis of brain lesion load and atrophy in longitudinal studies of multiple sclerosis. J Neurol. 2013;260(10):2458-2471. doi: 10.1007/s00415-012-6762-5.
15. Manjón JV, Coupé P. volBrain: an online MRI brain volumetry system. Front Neuroinform. 2016;10:30. doi: 10.3389/fninf.2016.00030.
16. Torres-Olivas E, Brito-Delgado RI, Hernandez-Medina A, Ayala-Ochoa F. Thalamic atrophy correlates with white matter lesion metrics in Mexican patients with multiple sclerosis: an automated MRI volumetry analysis. J Mex Fed Radiol Imaging. 2025;4(3):163-172 doi: 10.24875/JMEXFRI.M25000109.
17. Friedrichsmeier T, RKWard Team. RKWard: graphical interface to the statistical language R [Internet]. Version 0.8.0. 2024. Available from: https://rkward.kde.org.
18. McKinley R, Wepfer R, Aschwanden F, Grunder L, Muri R, Rummel C, et al. Simultaneous lesion and brain segmentation in multiple sclerosis using deep neural networks. Sci Rep 2021;11(1):1087. doi:10.1038/s41598-020-79925-4.
19. de Oliveira M, Piacenti-Silva M, da Rocha FCG, Santos JM, Cardoso JDS, Lisboa-Filho PN. Lesion volume quantification using two convolutional neural networks in MRIs of multiple sclerosis patients. Diagnostics (Basel). 2022;12(2):230. doi:10.3390/diagnostics12020230.
20. Pareto D, Sastre-Garriga J, Alberich M, Auger C, Tintoré M, Montalban X et al. Brain regional volume estimations with NeuroQuant and FIRST: a study in patients with a clinically isolated syndrome. Neuroradiology. 2019;61(6):667-674. doi:10.1007/s00234-019-02191-3.

JMeXFRI

Journal of the Mexican Federation of Radiology and Imaging

Check for updates

BRIEF RESEARCH ARTICLE

Saline needle-tract sealing for preventing complications in CT-guided percutaneous lung biopsy: an exploratory study

R. Daniela Treviño-Carranza[1,2], Marcela Aldape-Perez[2], Miguel A. Carrillo-Martinez[1,2] and Anais D. Garcia-Aguilar[1,2]*

[1]Department of Interventional Radiology; [2]Department of Radiology and Imaging. Zambrano Hellion Hospital TecSalud, San Pedro Garza Garcia, Nuevo Leon, Mexico

ABSTRACT

Saline needle tract sealing is a technique used to reduce pleuropulmonary complications during computed tomography (CT)-guided percutaneous lung biopsy. This retrospective, comparative cohort study compared complication rates in patients who underwent CT-guided percutaneous lung biopsy using the standard coaxial technique, with and without saline needle tract sealing. Pneumothorax and pulmonary hemorrhage were recorded as biopsy complications in patients with and without saline needle tract sealing. Thirty-three patients underwent CT-guided percutaneous lung biopsy with the standard coaxial technique: 15 (45.5%) with saline sealing and 18 (54.5%) without sealing. The incidence of pneumothorax was 11.1% (2/18 patients) in the group without saline sealing and 0% in the group with saline sealing (p = 0.19). The incidence of pulmonary hemorrhage was 22.2% (4/18 patients) in the unsealed group and 0% in the needle tract saline-sealing group (p = 0.055). Saline needle tract sealing in patients undergoing CT-guided percutaneous lung biopsy with the standard coaxial technique may prevent pleuropulmonary complications, such as pneumothorax and pulmonary hemorrhage, compared with patients without saline sealing. In this exploratory study of Mexican patients, sealing the needle tract with saline solution during CT-guided lung biopsy was associated with no complications. It is a simple, safe, and low-cost technique that may improve the safety of lung biopsy.

Keywords: *Needle tract saline sealing. Percutaneous lung biopsy. Pneumothorax. Pulmonary hemorrhage.*

INTRODUCTION

Computed tomography (CT)-guided percutaneous lung biopsy is a widely used technique for histological diagnosis of lung lesions. The standard coaxial technique, which uses an introducer needle to allow multiple passes of a cutting needle through a single pleuropulmonary access, remains the most widely used approach[1,2]. Pneumothorax, pulmonary hemorrhage, and hemoptysis are complications of CT-guided percutaneous lung biopsy that have been associated with various technical and patient-related clinical factors[2]. The most common complication is pneumothorax, with an incidence of 20%-45%[1-3]. Various strategies have been proposed to reduce the incidence of pneumothorax, including the rapid turning maneuver and the use of sealing materials[3,4], which increase the cost and/or time of the lung biopsy procedure. These materials can also cause local inflammatory reactions, including granuloma formation and fibrotic changes in the lung parenchyma[5].

Saline sealing of the needle path at the puncture site has been proposed as a simple, inexpensive, and safe option to reduce the risk of pneumothorax after lung biopsy[4,6]. This technique involves temporarily replacing

***Corresponding author:**
R. Daniela Treviño-Carranza
E-mail: daniela.trevino95@gmail.com

Received for publication: 12-02-2026
Accepted for publication: 27-03-2026
DOI: 10.24875/JMEXFRI.M26000130

Available online: 08-07-2026
J Mex Fed Radiol Imaging. 2026;5(2):134-140
www.JMeXFRI.com

alveolar air with isotonic fluid during removal of the coaxial needle, thereby promoting collapse of the pleuroparenchymal tract and reducing air leakage[1,6,7]. Previous reports have shown significant reductions in the incidence of pneumothorax[1,6,8]. The benefits of saline needle tract sealing vary with the characteristics of the study population and anatomical risk factors[9,10]. This study compared complication rates of CT-guided percutaneous lung biopsy using the standard coaxial technique, with and without saline needle tract sealing.

MATERIAL AND METHODS

This comparative, retrospective, cohort study was conducted from March 2023 to December 2025 at Zambrano Hellion Hospital, San Jose Hospital, Swiss Hospital, Doctors Hospital, and Christus Muguerza Hospital in Monterrey, Nuevo Leon, Mexico. Patients with lung lesions who underwent CT-guided percutaneous lung biopsy using the standard coaxial technique were included. Patients with incomplete records or without post-procedure imaging were excluded. All patients provided informed consent.

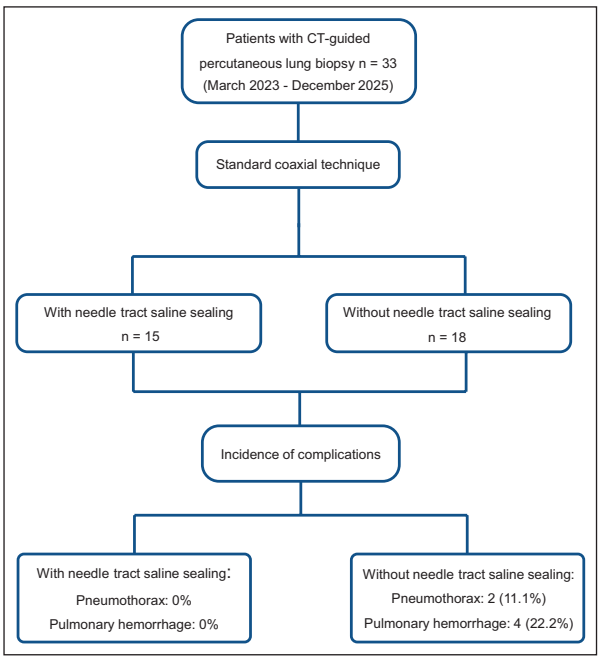

Figure 1. Flow diagram of patients who underwent CT-guided percutaneous lung biopsy using the standard coaxial technique. The incidence of pneumothorax and pulmonary hemorrhage was compared between patients with and without needle tract saline sealing.
CT: computed tomography.

Study development and variables

Age, sex, maximum size and location of the lung lesion, pleura-lesion distance, number of samples obtained, patient position during the procedure, and needle caliber were recorded. The presence of lung emphysema, defined radiologically as areas of low pulmonary attenuation without visible walls, with centrilobular, paraseptal, or panlobular predominance on baseline CT before the procedure, was also documented.

All patients underwent CT-guided percutaneous lung biopsy using the standard coaxial technique and were classified into two groups: with or without saline needle tract sealing. The interventional radiologist arbitrarily assigned patients to groups based on lesion depth, location, and size. The complications evaluated were pneumothorax after percutaneous lung biopsy, defined as air in the pleural space, and pulmonary hemorrhage, defined as alveolar opacities and perilesional or biopsy-path consolidation on immediate post-procedural chest CT.

CT-guided percutaneous lung biopsy technique

A 17-gauge (G) coaxial system and an 18-G cutting needle were used. Patients were positioned supine, prone, or lateral, depending on lesion location. The biopsy technique was performed as described by vanSonnenberg et al.[11]. In the needle tract saline-sealing group, after the biopsy, the puncture access was sealed with 1 to 3 mL of 0.9% NaCl solution during withdrawal of the coaxial needle. Patients were monitored for two hours after the lung biopsy to assess for complications. A post-procedural chest CT was performed in all patients. All procedures were performed by the same interventional radiologist (MCM), who has 32 years of experience in image-guided procedures.

Statistical analysis

Absolute and relative frequencies were calculated, and the chi-square and Mann-Whitney U tests were used to compare variables. A p value < 0.05 was considered statistically significant. Epi Info version 7.2.6.0 (Centers for Disease Control and Prevention, Atlanta, GA, USA) was used for analyses.

RESULTS

Thirty-six patients undergoing CT-guided percutaneous lung biopsy were evaluated. Three cases were excluded due to missing information on the procedure or CT scan. Thirty-three patients were included and

Table 1. Characteristics of patients undergoing CT-guided percutaneous lung biopsy with and without saline needle tract sealing

Description	Standard coaxial technique		p
	With saline needle tract sealing (n = 15)	Without saline needle tract sealing (n = 18)	
Sex, n (%)			0.85
Men	8 (46.7)	9 (50.0)	
Women	7 (53.3)	9 (50.0)	
Age, years, mean ± SD	66.6 ± 11.8	72.7 ± 12.8	0.17
Emphysema, n (%)	1 (6.7)	3 (16.7)	0.388
Lesion size, mm, mean ± SD	35.1 ± 10.6	45.4 ± 22.7	0.193
Location of pulmonary lesion, n (%)			0.476
Upper lobe	8 (53.3)	9 (50.0)	
Middle lobe	1 (6.7)	0	
Lower lobe	6 (40.0)	9 (50.0)	
Pleura-to-lesion distance, mm, mean ± SD	21.1 ± 12.3	9.9 ± 10.8	0.007
Lesion depth, n (%)			0.044
Adherent	0	9 (50.0)	
Superficial	9 (60.0)	7 (38.9)	
Non-superficial	6 (40.0)	2 (11.1)	
Patient position, n (%)			0.624
Supine	6 (40.0)	9 (50.0)	
Prone	8 (53.3)	7 (38.9)	
Lateral	1 (6.7)	2 (11.1)	
Number of lung biopsy samples, mean ± SD	3 ± 1	3 ± 1	0.446

CT: computed tomography; SD: standard deviation.

Table 2. Comparison of complications during CT-guided percutaneous lung biopsy with and without saline needle tract sealing

Complication	Standard coaxial technique		p
	With saline needle tract sealing (n = 15)	Without saline needle tract sealing (n = 18)	
Pneumothorax, n (%)	0	2 (11.1)	0.19
Pulmonary hemorrhage, n (%)	0	4 (22.2)	0.055

CT: computed tomography.

divided into two groups: 15 (45.5%) with saline needle tract sealing and 18 patients (54.5%) without needle tract sealing (Figure 1). All procedures were performed with an 18-G needle.

Characteristics of patients undergoing CT-guided percutaneous lung biopsy with and without saline needle tract sealing

Sex, age, emphysema, size and location of the lung lesion, patient position, and number of lung biopsies did not differ significantly between the groups with and without saline needle tract sealing (Table 1). The pleura-lesion distance was significantly greater in the needle tract saline-sealing group (21.1 ± 12.3 mm) than in the group without saline needle tract sealing (9.9 ± 10.8 mm) (p = 0.007). Lesion depth was superficial in 9 patients (60.0%) and non-superficial in 6 (40.0%) in the needle tract saline-sealing group, whereas in the group without saline needle tract sealing, 9 patients (50.0%) had adherent lesions, 7 (38.9%) had superficial lesions, and 2 (11.1%) had non-superficial lesions (p = 0.044). The mean number of samples obtained per procedure was similar between the two groups (3 ± 1 vs. 3 ± 1, respectively; p = 0.446).

Comparison of the incidence of CT-guided percutaneous lung biopsy complications with and without saline needle tract sealing

The incidence of pneumothorax was 11.1% (2/18 procedures) in the group without needle tract saline sealing. Pleural drainage was not required in the pneumothorax cases.

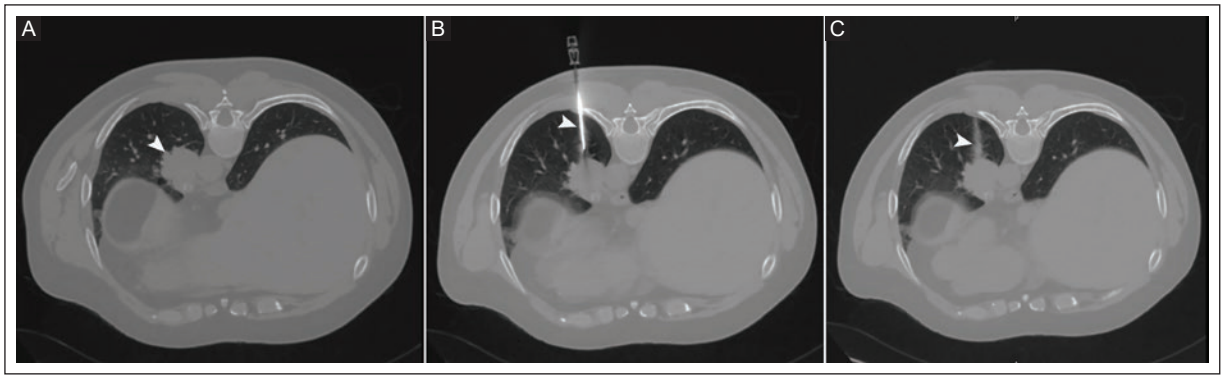

Figure 2. Axial chest CT of a 45-year-old man with a left lung mass who underwent a CT-guided percutaneous lung biopsy using the standard coaxial technique and saline needle tract sealing. **A:** a left lower lobe pulmonary mass (arrowhead). **B:** the position of the 18G coaxial needle within the left lower-lobe mass (arrowhead). **C:** a linear tract of saline solution is observed after withdrawing the coaxial needle (arrowhead). There is no evidence of post-procedural pneumothorax or pulmonary hemorrhage on immediate post-biopsy chest CT.

CT: computed tomography; G: gauge.

Figure 3. Axial chest CT of a 67-year-old man with a right lung mass who underwent a CT-guided percutaneous lung biopsy using the standard coaxial technique without saline needle tract sealing. **A:** right upper lobe pulmonary mass (arrowhead). **B:** position of the 18G coaxial needle within the right upper lobe lesion (arrowhead). **C:** right pulmonary mass with a visible post-biopsy tract after withdrawing the coaxial needle. A small pneumothorax (arrowhead) was identified on immediate post-biopsy chest CT.

CT: computed tomography; G: gauge.

There were no cases of pneumothorax in the saline needle tract sealing group (Table 2). Pulmonary hemorrhage occurred in 22.2% (4/18) of procedures without needle tract saline sealing, whereas no complications occurred with saline sealing (p = 0.055).

Figure 2 shows a chest CT axial view of a 45-year-old man with a left lung mass who underwent CT-guided percutaneous lung biopsy using the standard coaxial technique with needle tract saline sealing. No evidence of post-procedural complications such as pneumothorax or pulmonary hemorrhage on post-biopsy chest CT is seen. Figure 3 shows an axial view of a 67-year-old man with a right lung mass who underwent CT-guided percutaneous lung biopsy using the standard coaxial technique without needle tract saline sealing. A small residual pneumothorax was identified on post-biopsy chest CT. Figure 4A-C shows a chest CT view of a 64-year-old man with a left upper lobe pulmonary mass who underwent CT-guided percutaneous lung biopsy using the standard coaxial technique without needle tract

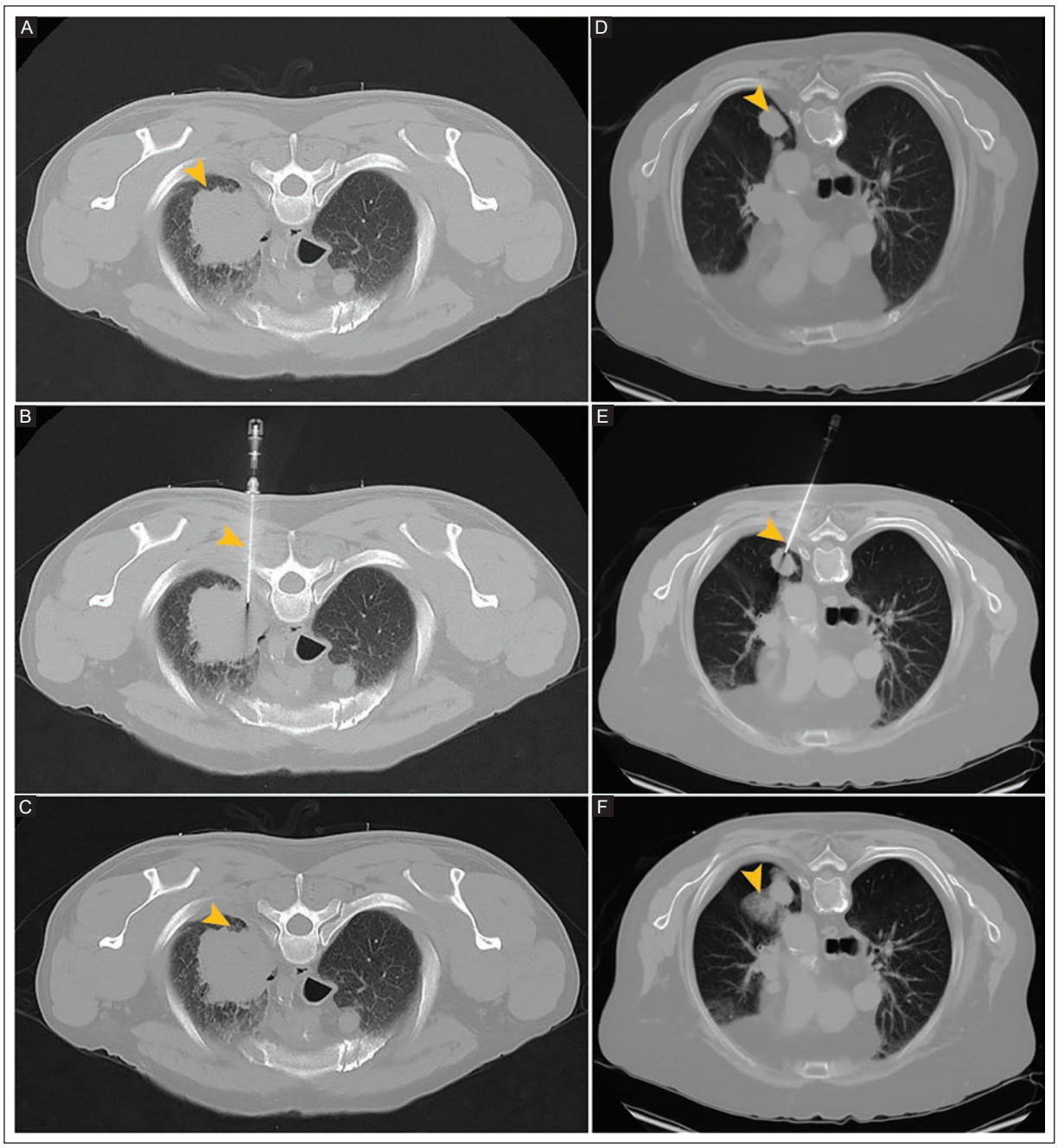

Figure 4. Chest CT scan of a 64-year-old man with a left upper-lobe mass who underwent a CT-guided percutaneous lung biopsy using the standard coaxial technique without saline needle tract sealing. **A:** left upper lobe pulmonary mass (arrowhead). **B:** position of the 18G coaxial needle within the pulmonary lesion (arrowhead). **C:** post-biopsy CT image with no complications (arrowhead). Chest CT view of a 74-year-old man with a left lower-lobe pulmonary nodule who underwent a CT-guided percutaneous lung biopsy using the standard coaxial technique without saline needle tract sealing. **D:** left lower lobe nodule (arrowhead). **E:** position of the 18G coaxial needle before tissue sampling (arrowhead). **F:** perilesional ground-glass opacities compatible with pulmonary hemorrhage are seen on post-biopsy chest CT (arrowhead).

CT: computed tomography; G: gauge.

saline sealing. There is no evidence of complications on post-biopsy chest CT. Figure 4D-F shows a 74-year-old man with a left lower lobe pulmonary nodule who underwent CT-guided percutaneous lung biopsy using the standard coaxial technique without needle tract saline sealing. Perilesional ground-glass opacities compatible with pulmonary hemorrhage are seen on post-biopsy chest CT.

DISCUSSION

No complications occurred in patients who underwent CT-guided percutaneous lung biopsy with saline needle tract sealing. In contrast, patients without needle tract saline sealing presented pneumothorax and pulmonary hemorrhage. In this exploratory study in Mexican patients, sealing the needle tract with saline solution during CT-guided lung biopsy was associated with no complications and is a simple, safe, and low-cost strategy that can improve the safety of lung biopsy.

Needle tract saline sealing obliterates the pleuroparenchymal tract by transiently replacing alveolar air with isotonic saline, thereby inducing collapse and limiting air leakage[1,6,7,9]. Billich et al.[6] conducted a prospective study that evaluated 140 German patients undergoing CT-guided percutaneous lung biopsy using the coaxial technique. Patients were alternately assigned to a tract saline sealing group (n = 70) – instillation of 2-4 mL of 0.9% saline solution during removal of the guide needle, or to a control group (n = 70) without sealing. A significant reduction in pneumothorax from 34% to 8% was reported ($p < 0.001$). Babu et al.[8] retrospectively compared 100 CT-guided transthoracic percutaneous lung biopsies using the coaxial technique with injection of 1-3 mL of saline during sheath removal with 100 unsealed biopsies. The incidence of pneumothorax was 32% in the sealed group and 46% in the group without saline injection along the needle tract ($p = 0.042$). Li et al.[1], in a randomized study, evaluated 322 Chinese patients undergoing CT-guided lung biopsy using the coaxial technique, with 161 patients in a tract saline-sealing group and 161 in a non-sealing group. They found a significant reduction in the incidence of pneumothorax from 26.1% to 6.2% ($p < 0.001$) in the saline-sealing group. In contrast, Okamoto et al.[10], in a single-center Japanese retrospective study analyzing 298 CT-guided lung biopsies, compared a tract saline sealing group (n = 138), in which 1-5 mL of normal saline was instilled during inserter needle removal, with a control group without sealing (n = 160). They did not find a significant reduction in the incidence of pneumothorax or chest tube placement. They suggested that in patients with a high prevalence of small lesions, isolated saline sealing may be insufficient to decrease the risk of post-biopsy pneumothorax. The incidence of pneumothorax in our study was 11.1% in the group without saline needle tract sealing, whereas none was observed in the group with saline needle tract sealing. These findings confirm the protective effect of saline needle tract sealing, which maintained its preventive effect even when applied to deeper lesions, a factor recognized as an independent predictor of pneumothorax[1,2,9].

Pulmonary hemorrhage, although generally self-limiting, is a clinically relevant complication in patients who have undergone CT-guided percutaneous lung biopsy. From a pathophysiological perspective, saline sealing acts as an inert liquid sealant that promotes alveolar collapse and may also limit blood extravasation into the lung parenchyma[5,6]. Zhang et al.[9] in a single-center retrospective study in China, evaluated 227 patients who underwent CT-guided percutaneous lung biopsy using the standard coaxial technique. These researchers compared a saline tract sealing group (n = 95) with a group without saline tract sealing (n = 132). Three to five mL of normal saline was applied during the gradual withdrawal of the coaxial needle in the saline tract-sealing group. They found no statistically significant difference between the two groups in the frequency of pulmonary hemorrhage (42.1% and 38.6%, respectively, $p = 0.599$). The authors concluded that saline tract sealing does not increase the risk of hemorrhagic complications. Billich et al.[6] reported three cases of pulmonary hemorrhage in a saline-sealed group (n = 70) compared to two cases in a non-sealed group (n = 70), with no significant difference between the groups ($p = 0.65$). There was no evidence of a clinically relevant increase in bleeding risk associated with saline instillation. In our study, pulmonary hemorrhage occurred only in the group without saline needle tract sealing. Our results suggest that the benefit of saline sealing is not limited to reducing pneumothorax but may also provide a protective effect, improving the overall safety of CT-guided percutaneous lung biopsy.

The strength of the present study is its comparative analysis of procedures with and without saline needle tract sealing in a real clinical setting, which lends practical relevance to the findings. However, this study has several limitations, including a small sample size, which limits statistical power, and the non-random assignment of patients to groups, which may introduce selection bias. The presence of hemoptysis was not evaluated. These limitations restrict the generalizability of the findings.

CONCLUSION

In this exploratory study, patients who underwent CT-guided percutaneous lung biopsy using the standard coaxial technique with needle tract saline sealing had no complications, while those without saline sealing developed pneumothorax and pulmonary hemorrhage.

Needle tract saline sealing may prevent complications in patients undergoing CT-guided percutaneous lung biopsy. Prospective studies with larger sample sizes are needed to confirm these results and establish its role as a standard for preventing complications.

Acknowledgments

The authors thank Professor Ana M. Contreras-Navarro for her guidance in preparing and writing this scientific paper.

Funding

The authors declare that they have not received funding.

Conflicts of interest

The authors declare no conflicts of interest.

Ethical considerations

Protection of human subjects and animals. The authors declare that the procedures followed were in accordance with the ethical standards of the responsible committee on human experimentation and with the World Medical Association and the Declaration of Helsinki (1964).

Confidentiality, informed consent, and ethical approval. The authors have followed their institution's confidentiality protocols, obtained informed consent from all patients. SAGER guidelines have been followed as applicable to the nature of the study.

Declaration on the use of artificial intelligence. The authors declare that no generative artificial intelligence was used in the writing or creation of the content of this manuscript.

REFERENCES

1. Li Y, Du Y, Luo TY, Yang HF, Yu JH, Xu XX, et al. Usefulness of normal saline for sealing the needle track after CT-guided lung biopsy. Clin Radiol. 2015;70(11):1192-1197. doi:10.1016/j.crad.2015.06.081.
2. Heerink WJ, de Bock GH, de Jonge GJ, Groen HJ, Vliegenthart R, Oudkerk M. Complication rates of CT-guided transthoracic lung biopsy: meta-analysis. Eur Radiol. 2017; 27(1):138-148. doi:10.1007/S00330-016-4357-8.
3. Khorochkov E, Garvin GJ, Potoczny S, Kozak RI. Injection of saline into the biopsy tract and rapid patient rollover decreases pneumothorax size following computed tomography-guided transthoracic needle biopsy. Can Assoc Radiol J. 2018;69(4):489-492. doi:10.1016/j.carj.2018.08.002.
4. Chan MV, Huo YR, Lui I, Ridley L. Tract sealing with normal saline after percutaneous transthoracic lung biopsies – promising but better evidence required. J Med Imaging Radiat Oncol. 2020; 64(6):800-802. doi: 10.1111/1754-9485.13090.
5. Satomura H, Higashihara H, Kimura Y, Nakamura M, Tanaka K, Ono Y, et al. Normal saline injection and rapid rollover: preventive effect on incidence of pneumothorax after CT-guided lung biopsy: a retrospective cohort study. BMC Pulm Med. 2024;24:505. doi:10.1186/s12890-024-03315-z.
6. Billich C, Muche R, Brenner G, Schmidt SA, Krüger S, Brambs HJ, et al. CT-guided lung biopsy: incidence of pneumothorax after instillation of NaCl into the biopsy tract. Eur Radiol. 2008;18(6):1146-1152. doi: 10.1007/S00330-008-0872-6.
7. Roman A, Brozba A, Necula A, Muntean DD, Kubelac P, Fekete Z, et al. Usefulness of saline sealing in preventing pneumothorax after CT-guided biopsies of the lung. Diagnostics. 2023;13(23):3546. doi: 10.3390/diagnostics13233546.
8. Babu SB, Srinivasan S, Chung R, Chawla A, Tan HK, Lohan R. Tract sealing with normal saline after percutaneous transthoracic lung biopsies. J Med Imaging Radiat Oncol. 2020; 64(2):211-214. doi:10.1111/1754-9485.13002.
9. Zhang X, An J, Wu J, Jing X, Lu H, Tian Y. Effect of saline sealing after CT-guided lung biopsy on pneumothorax and hemoptysis. J Comput Assist Tomogr. 2025;49(4):640-645. doi:10.1097/RCT.0000000000001725.
10. Okamoto S, Matsui Y, Tomita K, Munetomo K, Umakoshi N, Mitsuhashi T, et al. Is saline sealing of needle tract effective to prevent pneumothorax after computed tomography-guided lung biopsy? Interv Radiol. 2025; 10:e2025-0068. doi:10.22575/interventionalradiology.2025-0068.
11. vanSonnenberg E, Lin AS, Deutsch AL, Mattrey RF. Percutaneous biopsy of difficult mediastinal, hilar, and pulmonary lesions by computed tomographic guidance and a modified coaxial technique. Radiology. 1983; 148(1):300-302. doi:10.1148/radiology.148.1.6856853.

JMeXFRI

Journal of the Mexican Federation of Radiology and Imaging

Check for updates

CASE REPORT

Multimodality imaging of right-sided May-Thurner syndrome for accurate diagnosis and effective endovascular therapy: three case reports

Paola P. Alva-Espinoza[1], Miguel A. Hinostroza-Sanchez[2,3], Marcelo Valdes-Hernandez[4], Karla I. Soto-Valdez[1] and Francisco E. Puente-Gallegos[2]*

[1]Department of Radiology and Imaging; [2]Department of Interventional Radiology. Zambrano Hellion Hospital, TecSalud, San Pedro Garza Garcia; [3]Department of Radiology and Imaging, Hospital Christus Muguerza Alta Especialidad; [4]Hospital Regional Monterrey, Instituto de Seguridad y Servicios Sociales de los Trabajadores del Estado. Monterrey. Nuevo Leon, Mexico

ABSTRACT

Right-sided May-Thurner syndrome (MTS) is a rare variant involving iliac vein compression and can lead to delayed diagnosis. We present three male patients with chronic venous insufficiency of the right lower extremity who underwent Doppler ultrasound (US), digital subtraction venography (DSV), and intravascular ultrasound (IVUS). Doppler US identified hemodynamic abnormalities suggestive of venous obstruction. DSV demonstrated focal stenosis, intraluminal defects, and collateral circulation. IVUS confirmed significant luminal narrowing and precisely characterized the stenosis. All patients underwent thrombectomy, balloon angioplasty, and placement of an uncovered self-expanding stent, achieving adequate stent expansion and restoration of venous flow. These cases highlight the value of multimodal imaging for accurate diagnosis and effective endovascular management of right-sided MTS, particularly when iliac vein compression is atypical. Right-sided MTS is an unusual entity that is often overlooked in clinical practice. It is important to document the success of multimodal imaging, as diagnoses are often delayed due to its rarity. Therefore, combining Doppler US, DSV, and IVUS compensates for the limitations of each imaging modality. Endovascular therapy is the standard of care for restoring venous flow in right-sided MTS. It is safe, minimally invasive, and provides immediate restoration of vessel patency. This is the first report of three men with right-sided MTS, published for educational purposes.

Keywords: *May-Thurner syndrome. Iliac vein compression. Doppler. Intravascular ultrasound. Digital subtraction venography. Endovascular procedures.*

INTRODUCTION

Right-sided May-Thurner syndrome (MTS) is a rare condition characterized by anatomical variants, including compression of the right common iliac vein (CIV) that becomes trapped between the right internal and external iliac arteries[1], situs inversus associated with dextrocardia[2], a left-sided inferior vena cava, and a high aortic bifurcation[3,4]. This condition is more prevalent in women (2:1). Most patients are asymptomatic or present with mild symptoms[5,6]. Significant differences in clinical presentation are observed by gender[7]. While men more frequently report leg pain and swelling, women tend to present at a younger age and are more likely to develop pulmonary embolism[7].

The initial diagnostic approach uses Doppler ultrasound (US) to identify indirect findings of hemodynamic alterations, such as loss of phasicity, increased velocity, and turbulent flow. Digital subtraction venography (DSV) with intravascular ultrasound (IVUS) is the gold

***Corresponding author:**
Paola P. Alva-Espinoza
E-mail: prisalva1@gmail.com

Received for publication: 06-01-2026
Accepted for publication: 18-03-2026
DOI: 10.24875/JMEXFRI.M26000129

Available online: 08-07-2026
J Mex Fed Radiol Imaging. 2026;5(2):141-146
www.JMeXFRI.com

standard for diagnosing MTS[5]. In the interventional setting, DSV allows dynamic assessment of venous flow and stenotic areas[8]. In this context, IVUS is a key tool, providing a more accurate assessment of the venous lumen, quantifying the luminal area, and characterizing intraluminal abnormalities that may not be evident on DSV[9].

Treatment of symptomatic MTS is predominantly endovascular, especially when thrombosis is present[1,10,11]. Among therapeutic methods, balloon angioplasty combined with placement of an uncovered self-expanding stent is the most commonly used to correct underlying stenosis[12,13]. This report describes multimodal imaging findings, including Doppler US, DSV, and IVUS, in three men with right-sided MTS who underwent endovascular management.

CASE CLINICAL DESCRIPTION

Case 1

A 56-year-old man presented with progressive edema of the right lower limb over 7 months, associated with pain, heaviness, and fatigue, all worsened by prolonged standing. *Imaging findings:* Doppler US (VINNO, E35, Barcelona, Catalonia, Spain) showed decreased peak systolic velocity (PSV) in the prestenotic segment of the right common iliac vein (CIV) and distal flow turbulence due to compression by the right common iliac artery (CIA) (Figure 1). The diagnosis was right-sided MTS. IVUS (Philips, Volcano, Amsterdam, Netherlands) confirmed a focal area of significant stenosis with a reduced luminal area. DSV (Philips, DSV Azurion 7 m20 Flex Arm, Amsterdam, Netherlands) demonstrated a stenotic segment with a filling defect consistent with thrombus and collateral circulation. Endovascular treatment included thrombectomy, balloon angioplasty, and placement of uncovered self-expanding stents (Zilver Vena Venous Self-Expanding Stent, Cook Medical, Bloomington, IN, USA). Follow-up DSV showed adequate stent expansion, restoration of luminal caliber, and improved flow.

Case 2

A 74-year-old man presented with chronic edema of the right lower limb, accompanied by pain, heaviness, and fatigue, all worsened by prolonged standing. *Imaging findings:* Doppler US (SonoScape, S9, Guangzhou, Guangdong, China) showed compression of the right CIV by the right CIA (Figure 2). The diagnosis was right-sided MTS. IVUS (Philips, Volcano) showed significant stenosis of the right CIV, with reduced luminal area and minimum diameter. After placement of uncovered self-expanding stents (Zilver Vena Venous Self-Expanding Stent), intraoperative IVUS demonstrated adequate expansion and restoration of vessel caliber. DSV (Philips, Volcano) confirmed the pre-treatment stenosis site, correct stent placement, and restoration of venous flow.

Case 3

A 63-year-old man with a history of right iliofemoral deep vein thrombosis and an inferior vena cava filter presented with pain in his right lower extremity over approximately 6 months. The pain progressively worsened, with heaviness, distal edema, and visible varicose veins. Symptoms were exacerbated by prolonged standing and partially improved with rest and limb elevation. *Imaging findings:* Doppler US (VINNO, E35) showed iliac venous compression (Figure 3). The diagnosis was right-sided MTS**.** DSV (Philips, Volcano) showed focal stenosis of the right CIV due to the right CIA, with absence of opacification in its upper third and collateral circulation, findings compatible with venous compression and recanalized chronic thrombosis. After thrombectomy and balloon angioplasty, multiple uncovered self-expanding stents (Zilver Vena Venous Self-Expanding Stent) were placed in the affected segment. DSV showed restoration of venous flow in the upper third, with no evidence of residual stenosis.

DISCUSSION

Multimodal imaging evaluation of right-sided MTS caused by extrinsic iliac venous compression in three men, using Doppler US, DSV, and IVUS, enabled accurate diagnosis and efficient endovascular therapy, including angioplasty and placement of uncovered self-expanding stents to restore deep venous flow. This is the first report of three men with right-sided MTS, published for educational purposes.

The diagnosis of MTS is traditionally based on demonstrating mechanical iliac venous stenosis in patients with chronic venous stenosis or thrombosis, and clinical suspicion is almost exclusively in the left limb[11]. The combination of DSV with IVUS is considered the gold standard for visualizing iliac vein compression and establishing the diagnosis of MTS[3]. In our three reported cases, the diagnostic protocol began with Doppler US, which detected hemodynamic alterations characterized

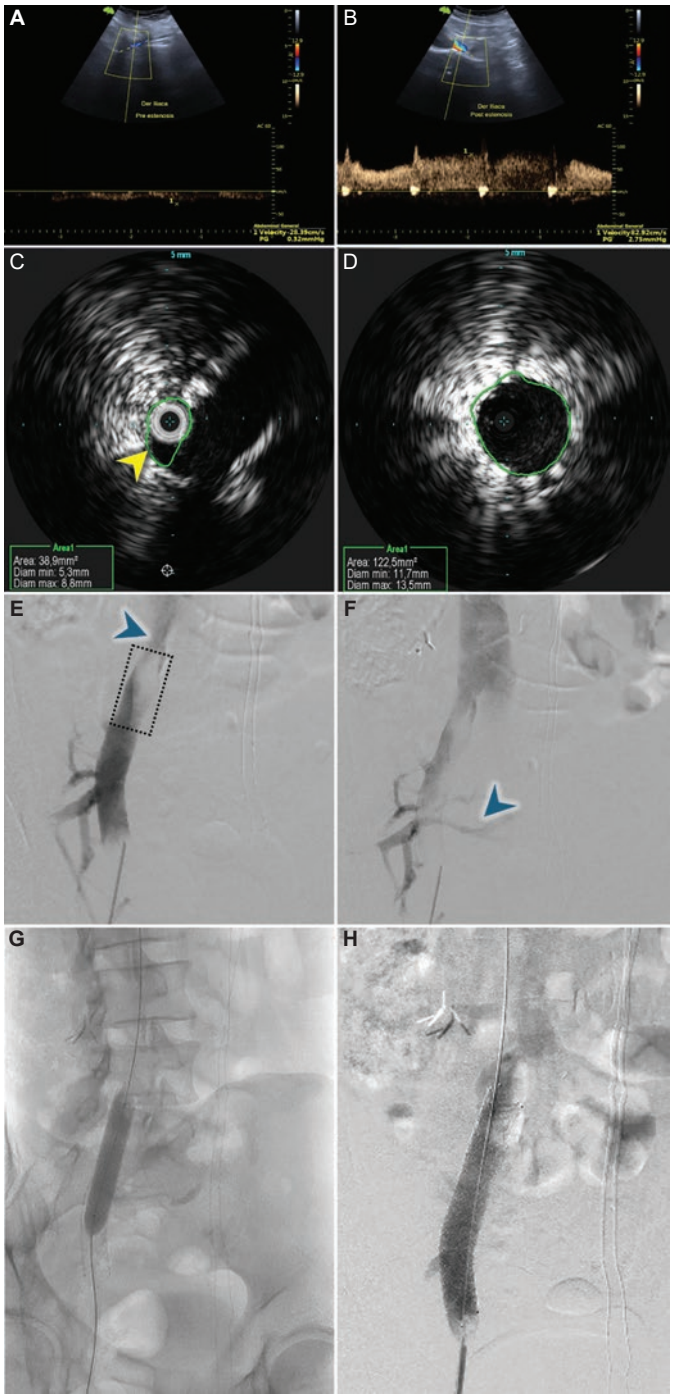

Figure 1. A 56-year-old male with progressive edema of the right lower limb over 7 months, accompanied by pain, heaviness, and fatigue during standing. **A:** color Doppler and spectral US of the right common iliac vein show a pre-stenotic segment with decreased PSV (28.39 cm/s), suggestive of proximal stenosis. **B:** color Doppler and spectral US of the upper third of the right common iliac vein show turbulent flow with increased PSV (82.92 cm/s) due to acceleration. These findings are consistent with right May-Thurner syndrome. **C:** IVUS demonstrates stenosis of the right common iliac vein (yellow arrowhead), with a luminal area of 38.9 mm² (reference value 150 mm²), confirming the stenosis. **D:** IVUS after balloon angioplasty and placement of an uncovered self-expanding stent in the stenotic segment shows adequate expansion and restoration of caliber, with a luminal area of 122.5 mm². **E:** DSV shows a stenotic segment (blue arrowhead) and a filling defect in the upper third of the right common iliac vein, compatible with thrombus (dotted square). **F:** DSV shows collateral venous vessels (blue arrowhead) secondary to the thrombus. **G:** DSV during endovascular therapy, post-thrombectomy, shows balloon angioplasty and placement of an uncovered self-expanding stent in the stenotic segment. **H:** DSV after placement of an uncovered self-expanding stent in the right common iliac vein shows restoration of luminal caliber and adequate opacification after intravenous administration of iodinated contrast media.

DSV: digital subtraction venography; IVUS: intravascular ultrasound; PSV: peak systolic velocity; US: ultrasound.

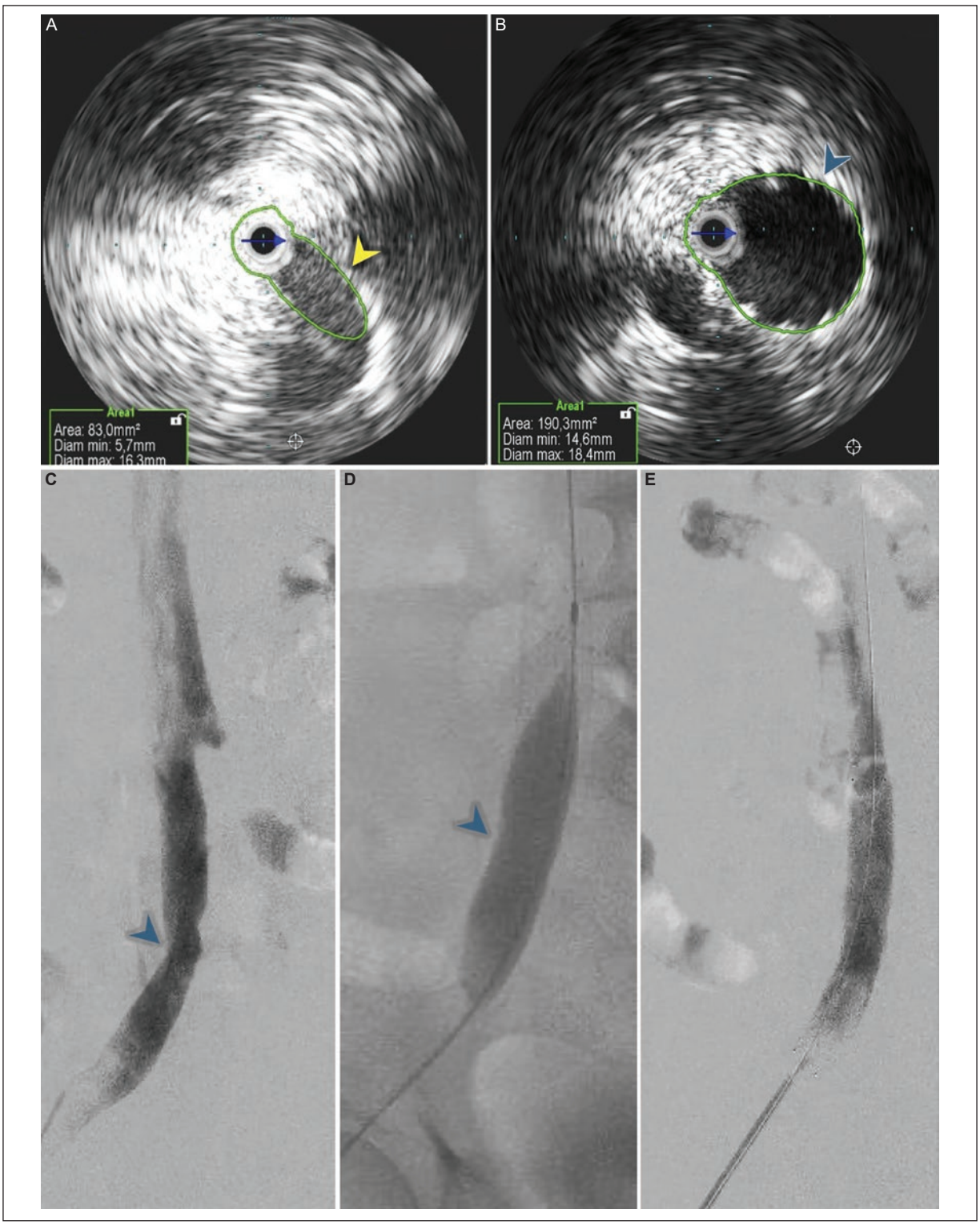

Figure 2. A 74-year-old male with right lower-limb edema, associated with heaviness and pain that worsen with prolonged standing. **A:** intraoperative IVUS shows significant stenosis of the right common iliac vein (yellow arrowhead), with an area of 83 mm² and a minimum diameter of 5.7 mm. The diagnosis is right May-Thurner syndrome. **B:** intraoperative IVUS after placement of an uncovered self-expanding stent in the right common iliac vein shows adequate expansion and restoration of caliber (blue arrowhead), with an area of 190 mm² and a minimum diameter of 14.6 mm. **C:** intraoperative DSV shows a site of stenosis in the right common iliac vein before plasty (blue arrowhead). **D:** balloon plasty and uncovered self-expanding stents, with indentation at the stenosis site still visible on the lateral wall of the vessel (blue arrowhead). **E:** intraoperative DSV confirms correct positioning of the uncovered self-expanding stents and restoration of venous flow.

DSV: digital subtraction venography; IVUS: intravascular ultrasound.

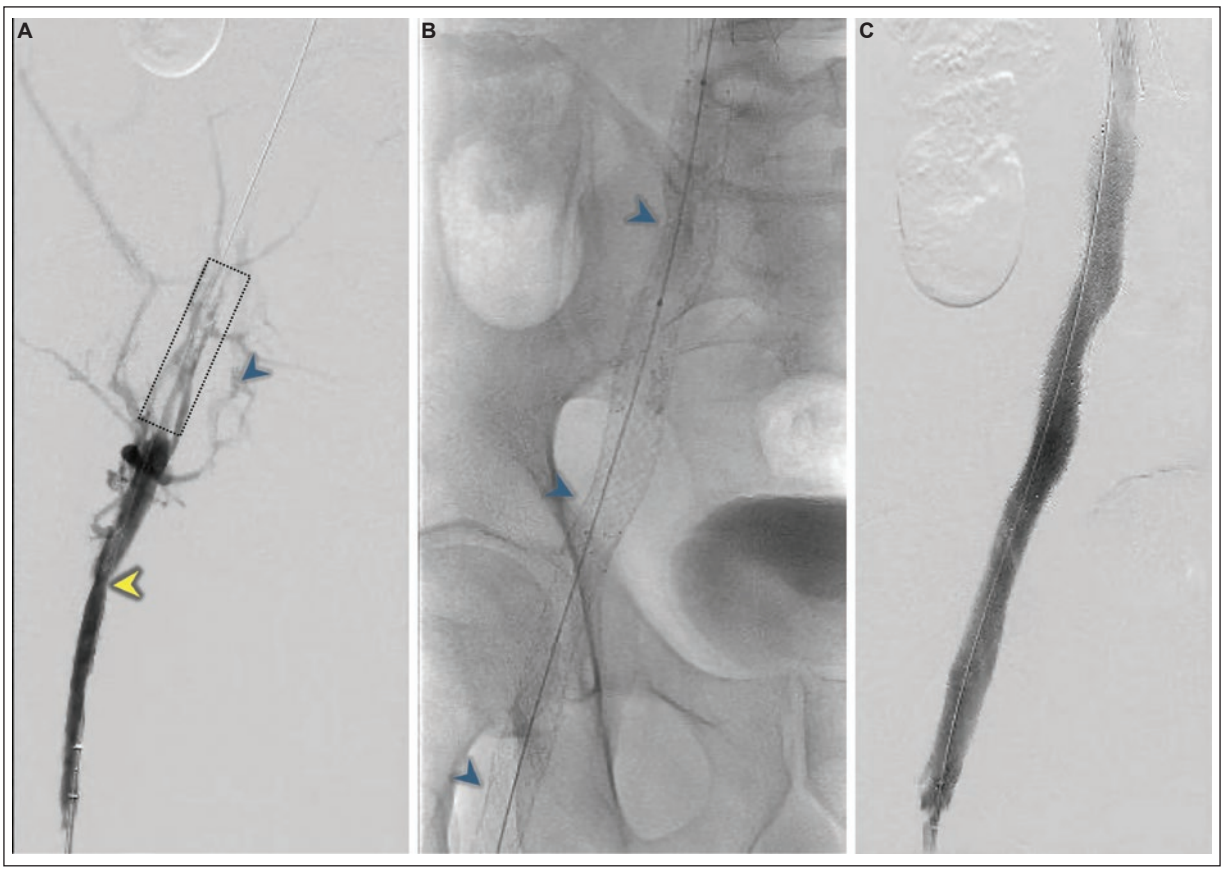

Figure 3. A 63-year-old male with right lower-limb pain for 6 months, associated with varicose veins and worsening symptoms with standing. He is diagnosed with right May-Thurner syndrome. **A:** DSV with focal stenosis (yellow arrowhead) of the right common iliac vein and absence of opacification in its upper third, associated with multiple collateral venous vessels (blue arrowhead and dotted square), consistent with venous compression and chronic thrombosis with recanalization. **B:** post-thrombectomy fluoroscopic image shows placement of three uncovered self-expanding stents (blue arrowheads) in the right common iliac vein after balloon angioplasty. The stenosis was corrected. **C:** DSV shows restored venous flow through the segment with uncovered self-expanding stents and no residual stenosis.

DSV: digital subtraction venography.

by a marked decrease in PSV in the pre-stenotic segment and turbulent flow with a compensatory increase in PSV distal to the site of obstruction due to thrombosis or venous stenosis. All three patients showed imaging findings of extrinsic compression of the right CIV by the right CIA, with a clinical presentation of obstructive venous symptoms. DSV complemented the diagnosis in cases one and three by revealing filling defects consistent with thrombosis and the development of multiple collateral vessels secondary to chronic obstruction. The incorporation of IVUS enabled precise identification of intraluminal structures such as spurs and fibrosis and accurate characterization of the degree of stenosis[10,11]. In our cases, IVUS overcame DSV's tendency to underestimate the severity of the obstruction[1]. Multimodal evaluation with Doppler US as an initial method to identify hemodynamic alterations, combined with DSV and IVUS, allows characterization of stenosis and represents the most accurate diagnostic strategy in right-sided MTS[1,3,11].

The principles of left-sided MTS management also apply to rare right-sided MTS variants, yielding significant clinical improvement with mechanical thrombectomy and stent placement[1]. In our three reported cases, endovascular techniques, including balloon angioplasty and placement of uncovered self-expanding stents, effectively restored vein integrity and normalized deep blood flow. The intervention immediately resolved the mechanical stenosis, as confirmed by follow-up IVUS, which demonstrated adequate expansion and restoration of vessel caliber. Similarly, Chen et al.[10] demonstrated that endovascular treatment of non-thrombotic iliac venous compression yields excellent patency with uncovered self-expanding stents, which allow more

precise positioning without migration. After deploying the uncovered self-expanding stent, post-dilation with larger balloons ensures proper stent attachment to the vessel wall, providing stability against extrinsic compression and chronic arterial pulsation[10,11]. This endovascular approach represents a critical advancement over open surgery, as it allows direct visualization of the degree of obstruction and repair of intraluminal stenosis without the morbidity associated with open surgery. Placement of uncovered self-expanding stents is essential when persistent stenosis remains after angioplasty, ensuring vessel stability against extrinsic compression and chronic arterial pulsation[11]. These techniques enable conclusive diagnosis and treatment in a single procedure, minimizing hospital stay[10,14].

CONCLUSION

Multimodal evaluation with Doppler US, DSV, and IVUS enabled accurate diagnosis and efficient endovascular management of right-sided MTS, resulting in complete restoration of deep venous flow in all three patients. Key imaging findings included decreased PSV and distal turbulence on Doppler US, significant focal stenoses with reduced luminal area on IVUS, and visualization of chronic thrombi and collateral circulation on DSV. Therefore, right-sided MTS should be considered in the differential diagnosis of unilateral edema or thrombosis of the right lower extremity. Multimodal assessment of extrinsic iliac venous compression should be prioritized.

Acknowledgments

The authors thank interventional radiologists Dr. M.A. Carrillo-Martínez and Dr. S.E. Kettenhofen-Jimenez, as well as vascular surgeon Dr. O. Villegas-Cabello, for their collaboration and contributions to the endovascular treatment of these cases. The authors also thank Professor Ana M. Contreras-Navarro for her guidance in preparing and writing this scientific paper.

Funding

The authors declare that they have not received funding.

Conflicts of interest

The authors declare no conflicts of interest.

Ethical considerations

Protection of human subjects and animals. The authors declare that the procedures followed were in accordance with the ethical standards of the responsible committee on human experimentation and with the World Medical Association and the Declaration of Helsinki (1964).

Confidentiality, informed consent, and ethical approval. Individual informed consent was not required for this observational study of information collected during routine clinical care.

Declaration on the use of artificial intelligence. The authors declare that no generative artificial intelligence was used in the writing or creation of the content of this manuscript.

REFERENCES

1. Tai E, Jaberi A, Oreopoulos GD, Forbes TL, Tan KT, Mafeld S. Diagnosis and management of right external iliac vein "sandwich": a rare cause of iliofemoral deep venous thrombosis. J Vasc Surg Cases Innov Tech. 2019;5(3):314-318. doi:10.1016/j.jvscit.2019.02.006.
2. Vijayalakshmi IB, Natraj Setty HS, Narasimhan C. Unusual cases of right-sided and left-sided May-Thurner syndrome. Cardiol Young. 2015; 25(4):797-799. doi:10.1017/S1047951114001115.
3. Nasif A, Ahmed AM, Al- Embideen S, Nazzal M, Osman M, Ahmed A. Unusual presentation of right-sided May-Thurner syndrome. J Vasc Surg Cases Innov Tech. 2021;7(4):768-771. doi: 10.1016/j.jvscit.2021.10.005.
4. Harbin MM, Lutsey PL. May-Thurner syndrome: history of understanding and need for defining population prevalence. J Thromb Haemost. 2020; 18(3):534-542. doi: 10.11/jth.14707.
5. Dwivedi A, Singh SN, Sharma A, Sharma R, Mishra T. A systematic review of radiological diagnosis and management of May-Thurner syndrome. J Pharm Bioallied Sci. 2024;16(Suppl 2): S1012-S1016. doi: 10.4103/jpbs.jpbs_1135_23.
6. Mousa AY, AbuRahma AF. May-Thurner syndrome: Update and review. Ann Vasc Surg. 2013; 27(7):984-995. doi:10.1016/j.avsg.2013.05.001.
7. Kaltenmeier CT, Erben Y, Indes J, Lee A, Dardik A, Sarac T, et al. Systematic review of May-Thurner syndrome with emphasis on gender differences. J Vasc Surg Venous Lymphat Disord. 2018;6(3):399-407. doi: 10.1016/j.jvsv.2017.11.006.
8. Brinegar KN, Sheth RA, Khademhosseini A, Bautista J, Oklu R. Iliac vein compression syndrome: clinical, imaging and pathologic findings. World J Radiol. 2015;7(11):375-381. doi:10.4329/wjr.v7.i11.375.
9. Woods MA, Knavel Koepsel EM, Swietlik JF, Shin DS, Chick JFB, Weaver JJ, et al. Intravascular US: applications in interventional radiology. Radiographics. 2022;42(6):1742-1757. doi:10.1148/rg.220015.
10. Chen ZL, Zhang XC, Sun Y, Xu M. Diagnosis and treatment of nonthrombotic right iliac vein compression syndrome. Ann Vasc Surg. 2019;61: 363-370. doi:10.1016/j.avsg.2019.05.033.
11. Burke RM, Rayan SS, Kasirajan K, Chaikof EL, Milner R. Unusual case of right-sided May-Thurner syndrome and review of its management. Vascular. 2006;14(1):47-50. doi:10.2310/6670.2006.00012.
12. Lan YQ, Chen YM, Lan KS, Feng N, Xi ZF. Demographic characteristics, clinical manifestations, and treatment outcomes of May-Thurner syndrome: a five-year retrospective analysis using computed tomography venography in a Chinese population. Curr Med Res Opinion. 2024;40(11): 2013-2019. doi: 10.1080/03007995.2024.2418428.
13. Poyyamoli S, Mehta P, Cherian M, Anand RR, Patil SB, Kalva S, et al. May-Thurner syndrome. Cardiovasc Diagn Ther. 2021;11(5):1104-1111. doi: 10.21037/cdt.2020.03.07.
14. Fretz V, Binkert CA. Compression of the inferior vena cava by the right iliac artery: a rare variant of May-Thurner syndrome. Cardiovasc Intervent Radiol. 2010;33(5):1060-1063. doi:10.1007/s00270-009-9671-y.

JMeXFRI

Journal of the Mexican Federation of Radiology and Imaging

IMAGES IN RADIOLOGY

Contrast-enhanced CT findings of primary pancreatic lymphoma with bilateral renal involvement

Christian D. Gaytan-Alonso[1]* *and Roberto T. Jimenez-Lopez*[2]

[1]*Department of Radiology and Imaging, Hospital Regional de Alta Especialidad del Bajio, IMSS-Bienestar;* [2]*Department of Radiology and Imaging, Hospital de Especialidades Pediatrico de Leon. Secretaria de Salud. Leon, Guanajuato, Mexico*

A 13-year-old girl presented with a one-month history of jaundice, abdominal pain, and weight loss. Contrast-enhanced computed tomography (CECT) showed a hypoenhancing pancreatic head mass encasing the portal vein and superior mesenteric artery without vascular occlusion (Figure 1A). At a higher axial level, intrahepatic biliary ductal dilatation and hepatosplenomegaly, consistent with distal biliary obstruction, were observed (Figure 1B). Coronal reformatted images showed multiple bilateral, rounded, hypoenhancing renal parenchymal masses, compatible with lymphomatous renal involvement (Figure 2A). The pancreatic head mass was associated with intrahepatic and extrahepatic biliary ductal dilatation (Figure 2B). No significant retroperitoneal or peripancreatic lymphadenopathy was identified. Ultrasound- guided biopsy of a renal lesion revealed B-cell lymphoblastic lymphoma. The diagnosis was primary pancreatic lymphoma (PPL) with bilateral renal involvement.

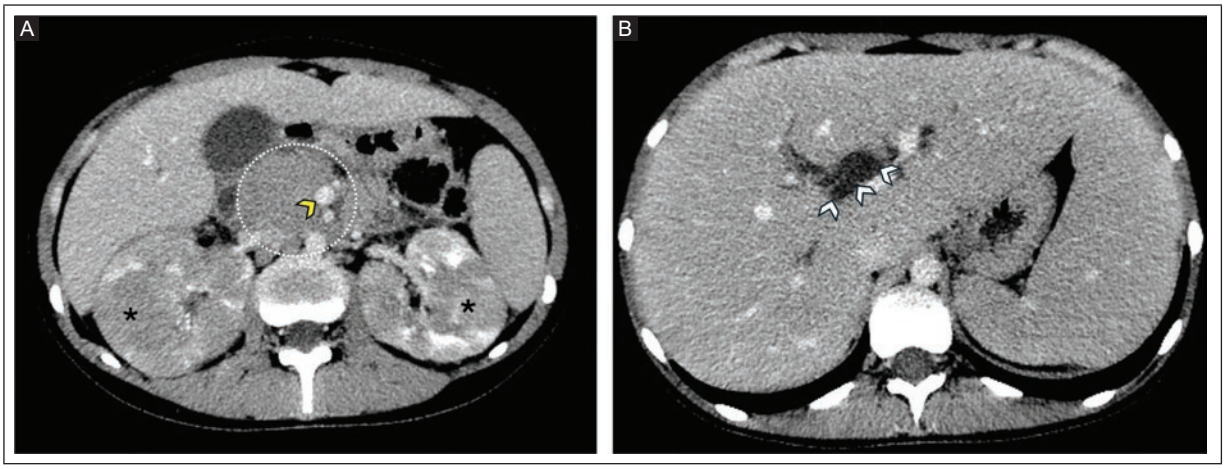

Figure 1. A 13-year-old girl was evaluated for a one-month history of jaundice, abdominal pain, and weight loss. **A:** axial CECT image shows a hypoenhancing mass in the pancreatic head (dashed circle) with encasement of the portal vein (yellow arrowhead) and the superior mesenteric artery. Multiple bilateral hypoenhancing renal parenchymal masses are also present (asterisks). **B:** CECT image at a more cranial level shows hepatosplenomegaly and marked intrahepatic biliary duct dilatation (white arrowheads). An ultrasound-guided biopsy of a renal lesion revealed B-cell lymphoblastic lymphoma. The diagnosis was PPL with bilateral renal involvement.

CECT: contrast-enhanced computed tomography; PPL: primary pancreatic lymphoma.

***Corresponding author:**
Christian D. Gaytan-Alonso
E-mail: cd.gaytanalonso@ugto.mx

Received for publication: 11-09-2025
Accepted for publication: 27-04-2026
DOI: 10.24875/JMEXFRI.25000026

Available online: 08-07-2026
J Mex Fed Radiol Imaging. 2026;5(2):147-149
www.JMeXFRI.com

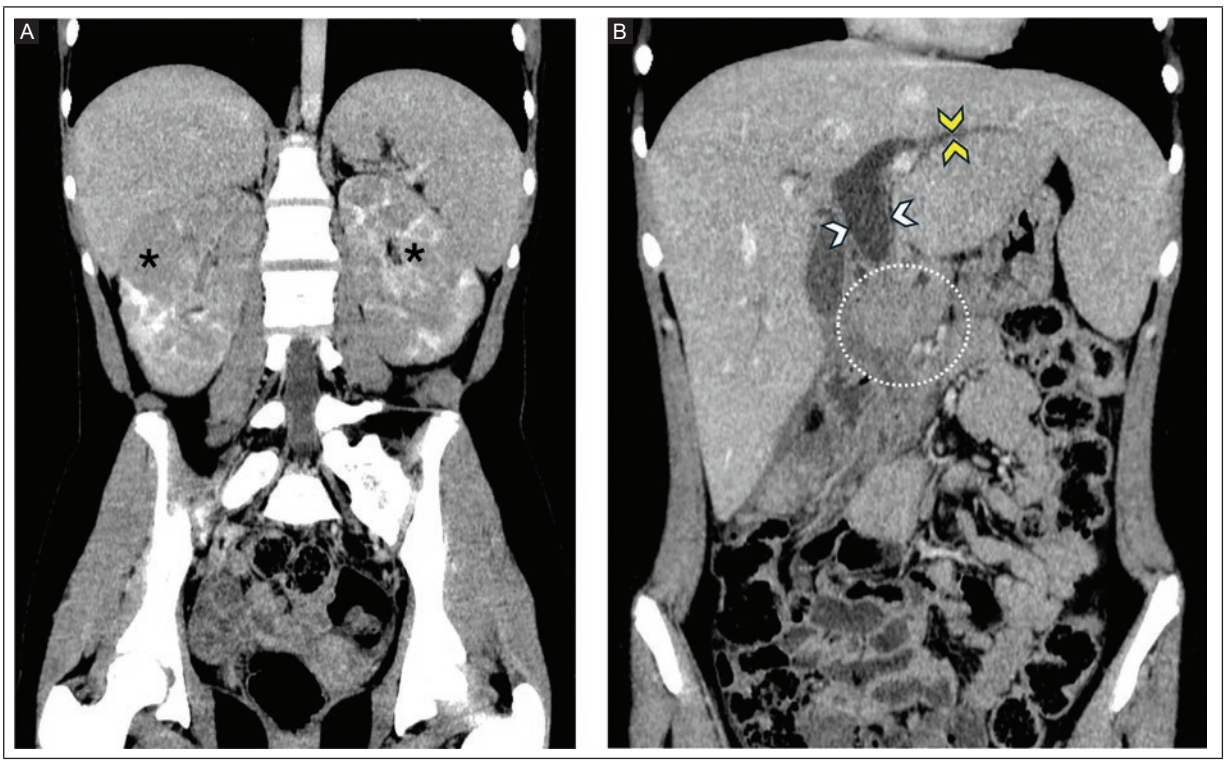

Figure 2. A 13-year-old girl was evaluated for a one-month history of jaundice, abdominal pain, and weight loss. **A:** coronal CECT reconstruction shows bilateral renal involvement with multiple rounded, hypoenhancing parenchymal masses (asterisks), consistent with lymphomatous infiltration. **B:** coronal CECT reconstruction shows a hypoenhancing mass in the pancreatic head (dashed circle), with intrahepatic (yellow arrowheads) and extrahepatic (white arrowheads) biliary duct dilatation, consistent with distal biliary obstruction. Hepatosplenomegaly is present. The diagnosis was PPL with bilateral renal involvement.

CECT: contrast-enhanced computed tomography; PPL: primary pancreatic lymphoma.

PPL is a rare neoplasm, particularly in the pediatric population[1]. It poses a diagnostic challenge because of its clinical and imaging similarities to other pancreatic lesions, primarily pancreatic adenocarcinoma[2]. An accurate diagnosis is crucial because treatments differ significantly: PPL responds well to chemotherapy, whereas adenocarcinoma requires surgical resection[3]. CECT findings, such as a bulky mass that encases vessels without occlusion and the absence of significant pancreatic ductal dilatation, help differentiate PPL from adenocarcinoma[3,4]. Although PPL itself is uncommon, its presentation can be even more atypical, as demonstrated by rare cases of simultaneous bilateral renal involvement, which further underscores its diagnostic complexity[5].

Acknowledgment

We thank Professor Ana M. Contreras-Navarro for her guidance in preparing and writing this scientific paper.

Funding

The authors declare that they have not received funding.

Conflicts of interest

The authors declare no conflicts of interest.

Ethical considerations

Protection of human subjects and animals. The authors declare that no experiments on humans or animals were performed for this research.

Confidentiality, informed consent, and ethical approval. The authors have followed their institution's confidentiality protocols for sharing patient data. Informed consent was not required to analyze and publish routinely acquired clinical and imaging data.

Declaration on the use of artificial intelligence. The authors declare that no generative artificial intelligence was used in the writing or creation of the content of this manuscript.

REFERENCES

1. Shapira G, Fisher Y, Ilivitzki A. Bifocal primary pancreatic Burkitt's lymphoma in a 4-year-old child. J Clin Ultrasound. 2017;45(3):171-174. doi:10.1002/jcu.22372.
2. Anand D, Lall C, Bhosale P, Ganeshan D, Qayyum A. Current update on primary pancreatic lymphoma. Abdom Radiol. 2016;41(2):347-355. doi:10.1007/s00261-015-0620-8.
3. Facchinelli D, Sina S, Boninsegna E, Borin A, Tisi MC, Piazza F, et al. Primary pancreatic lymphoma: clinical presentation, diagnosis, treatment, and outcome. Eur J Haematol. 2020;105(4):468-475. doi:10.1111/ejh.13468.
4. Low G, Panu A, Millo N, Leen E. Multimodality imaging of neoplastic and non-neoplastic solid lesions of the pancreas. Radiographics. 2011;31(4):993-1015. doi:10.1148/rg.314105731.
5. Javaugue V, Debiais-Delpech C, Nouvier M, Gand E, Chauvet S, Ecotiere L, et al. Clinicopathological spectrum of renal parenchymal involvement in B-cell lymphoproliferative disorders. Kidney Int. 2019;96(1):94-103. doi:10.1016/j.kint.2019.01.027.

PHILIPS

Ultrasound

Affiniti

Designed for your everyday

Stepping up to today's Philips Affiniti Ultrasound System means stepping up to the next level of performance to help with a confident diagnosis using streamlined workflow.

Upgrade to the latest Affiniti capabilities

Intuitive use

Experience a user interface and workflow that helps increase your productivity.

- Enhances user workflow with **system-guided protocols** that can be easily customized to suit your needs
- **Tablet-like 30.48 cm (12 in) touchscreen** with workflow-related controls for ease of use
- **Next Gen AutoSCAN reduces button pushes by up to 54%** with pixel-by-pixel real-time optimization and reduces the need for user adjustment while also enhancing transducer plunkability.*
- At just 83.5 kg (184 lb), the system is **16% lighter** than its predecessor system**
- **Shared transducer family** across Affiniti and Compact 5000*** series systems helps maximize your investment
- **Wireless networking** aids workflow

* When comparing VM10 performance to VM7.
** HD15.
*** R.S. #1437E2024 SSA.

Battery backup with sleep mode allows the system to **sleep in 2 seconds and return to full functionality in 20 seconds**

Consumes nearly 40% less power compared to our legacy predecessor system*

Intelligent imaging

Flow Viewer

Defines vasculature with a 3D-like appearance using both the velocity and power of the Doppler signal to accurately represent vascular flow topography

MicroFlow Imaging (MFI)

Provides remarkable sensitivity and detail in assessing blood flow

Find out more at
www.philips.com.mx/healthcare/solutions/ultrasound

Lunit

AI that supports every read

From chest X-ray to mammography—built for clinical practice

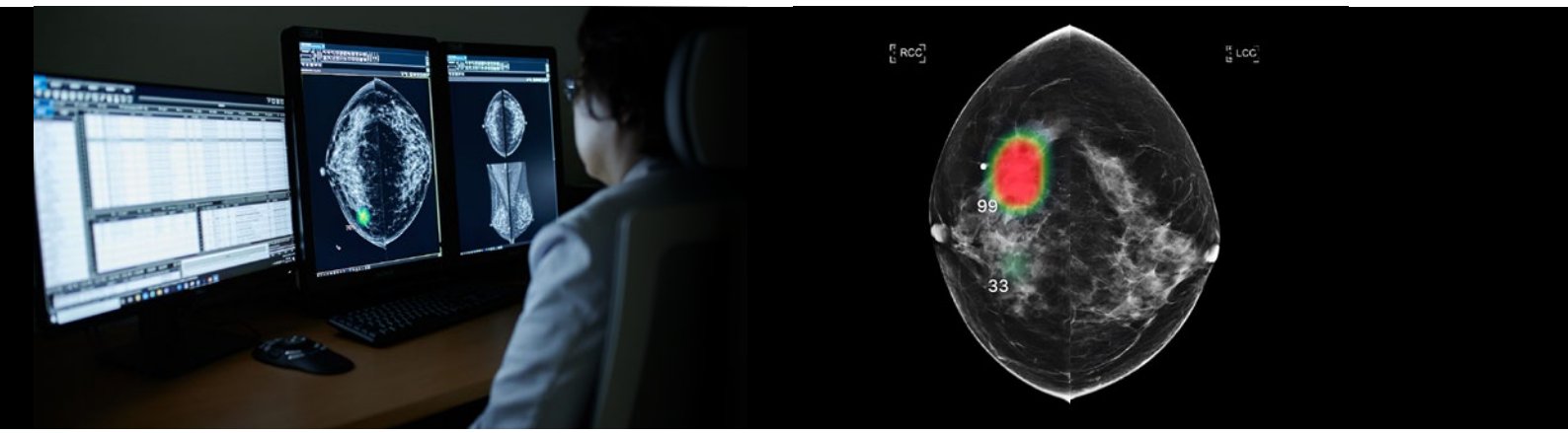

Lunit delivers clinically validated AI that supports radiologists across chest X-ray and breast imaging in daily practice—enhancing cancer detection, improving workflow efficiency, and enabling confident decision-making.

Built for real-world radiology. Proven in everyday practice.

Chest radiology

See Lunit INSIGHT CXR
Detect critical abnormalities

Breast imaging

Discover Lunit INSIGHT MMG & DBT
Detect cancer in 2D and 3D mammography

lunit.io

MRH Series
Horizontal Radiographic Systems

CMR

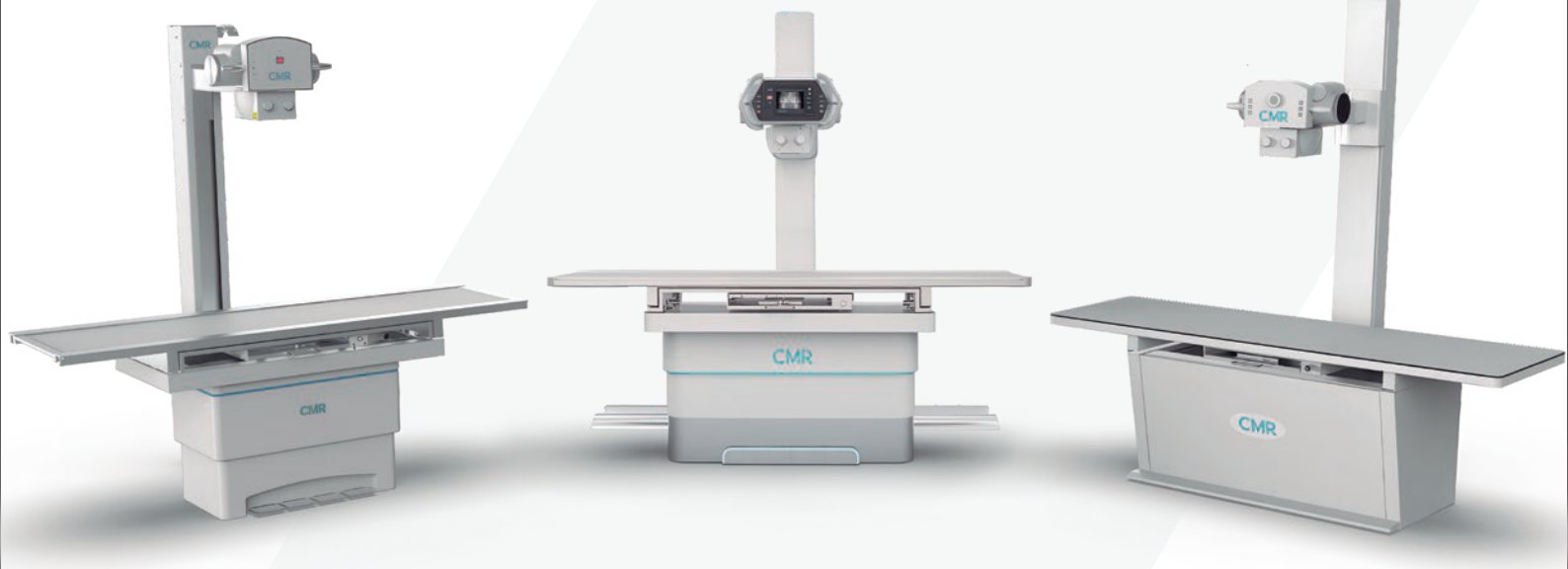

Innovative radiology
solutions for advanced care

cmr-rx.com
contacto@cmr3.com.mx
+52 55 9063 2047

FUTURA MEDICA
DIAGNÓSTICOS EN RADIOLOGÍA & LABORATORIO
MR

RADIOLOGY RESEARCH:
REVEALING TRUTH,
INSPIRING PROGRESS.

WWW.FUTURAMEDICADEMORELIA.COM

EI
Diagnóstico Especializado en Imágen

Dr. Gerardo S Navarro Gomez
Radiologist

Dr. Eduardo Sarda Inman
Radiologist

Dra. Beatriz Gonzalez Ulloa
Radiologist

Clinical Laboratory	General Ultrasound
Digital Radiology	Color Doppler Ultrasound
Digital Mammography	4D Structural Obstetric Ultrasound
Tomosynthesis	Musculoskeletal Ultrasound
Contrast-Enhanced Mammography	Peripheral Doppler Ultrasound
Computed Tomography (CT)	gnetic Resonance Imaging (MRI)

Guadalajara, Jalico. Mexico